Technische Universität München

Physik Department E20

Molecular Nanoscience and Chemical Physics of Interfaces

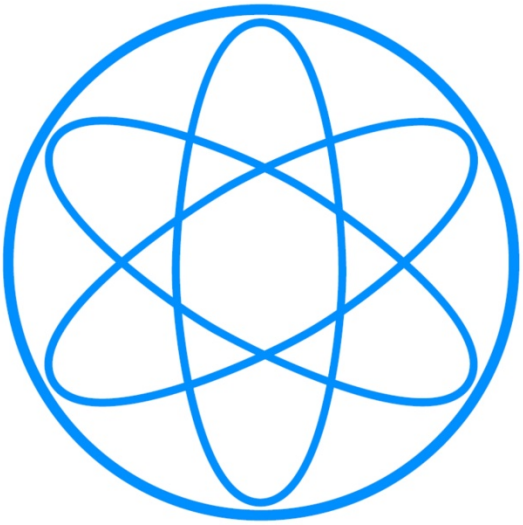

Two-dimensional lanthanide-directed metal-organic networks at surfaces

Dissertation

von

José Ignacio Urgel Tendero

TECHNISCHE UNIVERSITÄT MÜNCHEN

Lehrstuhl **E20** -

Molekulare Nanowissenschaften & Chemische Physik von Grenzflächen

Two-dimensional lanthanide-directed metal-organic networks at surfaces

José Ignacio Urgel Tendero

Vollständiger Abdruck der von der Fakultät für Physik der Technischen Universität München zur Erlangung des akademischen Grades eines Doktors der Naturwissenschaften (Dr. rer. nat.) genehmigten Dissertation.

Vorsitzender: Univ.-Prof. Dr. B. Garbrecht

Prüfer: 1. Univ.-Prof. Dr. J. V. Barth

2. Priv. Doz. Dr. M. Lackinger

3. Prof. R. Otero Ph. D., Universidad Autónoma de Madrid

Die Dissertation wurde am 17.12.2015 bei der Technischen Universität München eingereicht und durch die Fakultät für Physik am 08.03.2016 angenommen.

To my parents and brother

Abstract

The design and inspection of surface-confined metal-organic nanoarchitectures is a recent and relevant research field providing prospects in functional materials. During the last decade supramolecular protocols on surfaces have afforded the fabrication of distinct metallosupramolecular structures embedding mostly transition metals, nevertheless lanthanide elements remained elusive.

In this thesis, we have investigated lanthanide-directed metal-organic networks amenable to scanning tunneling microscopy, by exploiting the coordination between appropriate molecular linkers and lanthanide elements. To this aim, cerium (Ce), gadolinium (Gd) and europium (Eu) are selected as the f-block elements, whereas molecular species equipped with terminal carbonitrile or carboxylate functional groups are utilized as linkers. Due to the distinct coordinative characteristics of the lanthanide nodes we demonstrate an exceptional degree of flexibility of the coordination sphere and a high coordination number, which induces the expression of five-fold planar coordination motifs and allows for the fabrication of complex tessellations, including semi-regular Archimedean tilings and random-tiling quasicrystals. Furthermore, we illustrate the feasibility of designing on surfaces metallosupramolecular networks embedding simultaneously d- and f-block elements. Finally, we show the thermal stability of lanthanide-carboxylate architectures, thus paving the way for future applications that require robustness.

Our investigations will steer the development of advanced metal-organic protocols on surfaces exploiting lanthanide elements, whose study will reveal the behavior of f-block elements upon coordination on surfaces, with potential in the development of approaches in sensing, catalysis, luminescence and magnetism.

Contents

List of Figures

List of abbreviations

CSP. Cerium sublimation pump

CT. Cold trap

ddQC. Dodecagonal quasicrystal

DFT. Density functional theory

DOS. Density of states

DP. Diaphragm pump

DSP. Digital signal processor

Fcc. Face-centered cubic

FFT. Fast fourier transform

HKUST. Hong kong university of science and technology

HOMO. High occupied molecular orbital

IGP. Ion getter pump

IMDEA. Instituto madrileño de estudios avanzados

LDOS. Local density of states

LM. Lateral manipulation

LT-STM. Low-temperature scanning tunneling microscope

LUMO. Low unoccupied molecular orbital

MD. Molecular dynamics

MOCN. Metal-organic coordination network

MOF. Metal-organic framework

NIR. Near infrared

OMBE. Organic molecular beam epitaxy

PTCDA. Perylenetetracarboxylic dianhydride

QC. Quasicrystal

RT. Room temperature

SMM. Single molecular magnet

SPM. Scanning probe microscopy

STM. Scanning tunneling microscopy

STS. Scannind tunneling spectroscopy

TDA. 4,1′,4′,1′′-terphenyl-1,4′′-dicarboxylic acid

TEM. Transmission electron microscopy

TMP. Turbo molecular pump

TPCN. tetra-biphenylcarbonitrileporphyrin

TSP. Titanium sublimation pump

TUM. Technische universität München

UAM. Universidad autónoma de Madrid

UHV. Ultra high vacuum

UV. Ultraviolet

VM. Vertical manipulation

VT-STM. Variable-temperature scanning tunneling microscope

XMCD. X-ray magnetic circular dichroism

XPS. X-ray photoelectron spectroscopy

Acknowledgment

Many people have accompanied and supported me during this period of my life and I would to thank all of them.

First of all, I would like to thank Prof. Dr. Johannes V. Barth for his support and counseling and for giving me the opportunity to carry out my PhD thesis at this great group. Many thanks to Dr. Willi Auwärter for mentoring me. I am very grateful to him for the scientific discussions, support in the lab, availability in his office and easygoing discussions at the Mensa. I cannot be thankful enough to Dr. David Écija for introducing me into the LT-STM lab, being my mentor, scientific guide and above all a close friend during the last three years. Without the three of them this work would not have been possible.

I would like to thank all the LT-STM/AFM lab members, whose composition has change quite a bit in the last years but it has always maintained a friendly and constructive atmosphere. Felix Bishoff, Alissa Wiengarten, Tobias Kaposi, Sushoban Joshi and Dr. Knud Seufert for helping me every time I ask for assistance in the lab. I am especially grateful to Saranyan Vijayaraghavan for helping me at the beginning of my PhD being always with a smile on his face. I am also grateful to the "new" members of the LT-STM/AFM labs, Martin Schwarz for relaxed and fruitful discussions and Yuanquin He, Jacob Ducke and Domenik Zimmermann for their support. Another special thanks to Dr. Manuela Garnica for her significant help with the maintenance and implementation of the e-beam evaporator and for easygoing discussions. I am also grateful to Dr. Anthoula Papageorgiou, Sybille Fischer and Dr. Joachim Reichert for their help in the VT-STM during my first months at the E20.

Moreover, I am very thankful to the "Mensa team", Dr. Carlos-Andres Palma for interesting scientific and non-scientific discussions, Dr. Anthoula Papageorgiou, Dr. Yiqi Zhang, Dr. Willi Auwärter, Dr. David Écija, Dr. Florian Klappenberger, Dr. David A. Duncan and Nenad Kepčija for the great atmosphere during the lunch time.

I am thankful to our secretary Viktoria Blaschek for conveniently handling all the paper work (that was not little) and making my stay more comfortable. Thanks a lot to Max Glanz and Karl Eberle who were always ready to help me with their expertise for any

technical problem. Additionally, I would like to thank the people in my office, Runyuan Han, Tobias Kaposi, Florian Blobner, Peter Deimel and Andreas Kim for the good working environment in the last years. I thank all the other E20 members, not individually mentioned, for the excellent working environment in the last three years.

Furthermore it is a pleasure to acknowledge all the people who made me feel part of their group during my fruitful collaborations. I am particularly thankful to Borja A. Cirera for the awesome atmosphere in the work place and outside of it as well as to the rest of the group in IMDEA Nanoscience, Jonathan Rodríguez, Juan J. Navarro, Alberto Martín, Jesús Matarrubia, Carlos Guerrero and Victor Fernández. I would also like to thank Prof. Dr. Nian Lin for giving me the opportunity to join his group at HKUST which was a great experience from both professional and life points of view. Thanks to Guoquing Lyu and Tao Lin for helping me with the not easy task of finding an apartment in Hong Kong, Ran Zhang, Qiushi Zhang and Guowen Kuang for great time and conversations in the lab and canteen.

In addition, I would like to thank all my friends who have supported me during my last years in Munich.

Finally, my deepest thanks go to my great family, my parents, Carmen and Ignacio who always support me in everything I need and my brother Gonzalo for standing by me in every moment. Muchas muchas gracias!

1. Introduction

1.1 Nanotechnology background

Size matters…Human beings have been fascinated throughout centuries in things that escape from their perception, like invisible constituents of matter. During the last decades we have been learning to develop new materials, devices and manufacturing strategies that allow us to improve the way of communication, data handling, transportation and diagnosis or diseases treatment.

It was in the year 1959 when Richard Feynman (awarded with the Nobel Prize in 1965) delivered a speech "*I would like to describe a field, in which little has been done, but in which an enormous amount can be done in principle. This field is not quite the same as the others in that it will not tell us much of fundamental physics (in the sense of, "What are the strange particles?") but it is more like solid-state physics in the sense that it might tell us much of great interest about the strange phenomena that occur in complex situations"* in the famous lecture called ***There's Plenty of Room at the Bottom***[1]**.** It was the first time that someone spoke about the possibility of matter manipulation at the atomic scale and it opened a new window of opportunities in the scientific research that is changing the way we see the world.

NANOTECHNOLOGY (expression coined by Norio Taniguchi in 1974) is precisely the result of all this process of learning that lets us create, observe and manipulate systems that go from ≈ 100 nm to ≈ 1 Å in size, which is much smaller than anything one can see with the naked eye (Figure 1.1). It operates at the first organization level of atoms and molecules where the functions and properties of every system are determined and guarantees the ability to build accurate machines and components of molecular size. But how do we create materials on very small length scales? One traditional approach are the so-called **"top-down"** techniques, which consist in using tools (like photolithography or electronic bombardment) to whittle away undesired material to leave the final product. As an alternative, there is an increasing industrial interest in **"bottom-up"** techniques where the objective is to construct the desired nanostructure by the self-assembly of specific functional blocks[2]. The bottom-up approach is based in the use of

intermolecular interactions to control the process of molecular organization and by self-assembly, producing a desired pattern. Hereby, we can distinguish the supramolecular chemistry paradigm, which involves non covalent interactions such as van der Waals, hydrogen bonds, dipole-dipole or metal-organic links; and the covalent strategy that implies covalent bonds, more robust, lack of self-correction, and thus, limited to produce large regular assemblies.

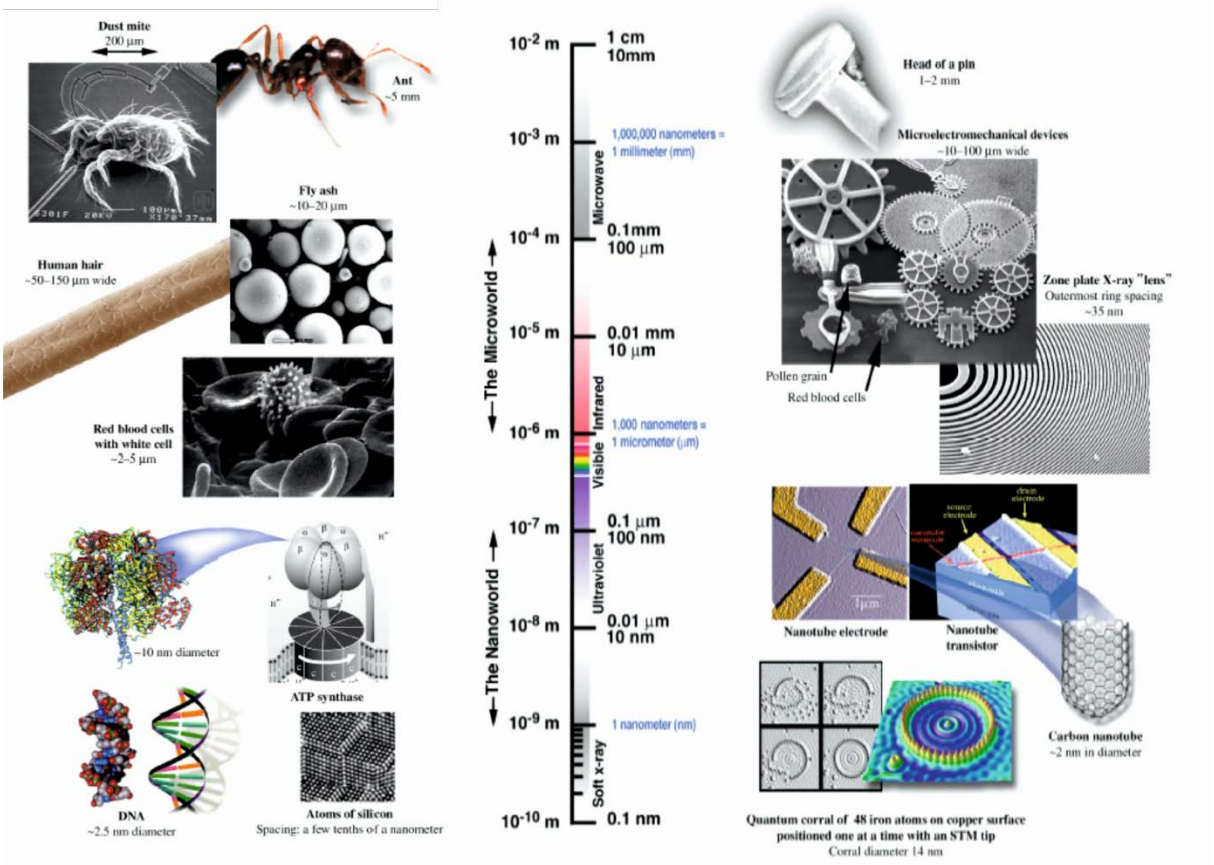

Figure 1 . 1 | Reaching at the nanoscale

Currently, nanotechnology is described as a revolutionary discipline in terms of its possible impact on industrial applications, understanding the complexity of working with nanoscale materials (Figure 1.2)[3]. Past industrial revolutions, driven by steam engines, internal combustion, electrical and computer power, have immensely affected our style of life and economy and have changed the course of society for all time. Now we can have a more evident picture of how to create nanoscale materials with novel properties never conceived before. Therefore, nanotechnology might represents more potential power than all previous technologies combined[4,5].

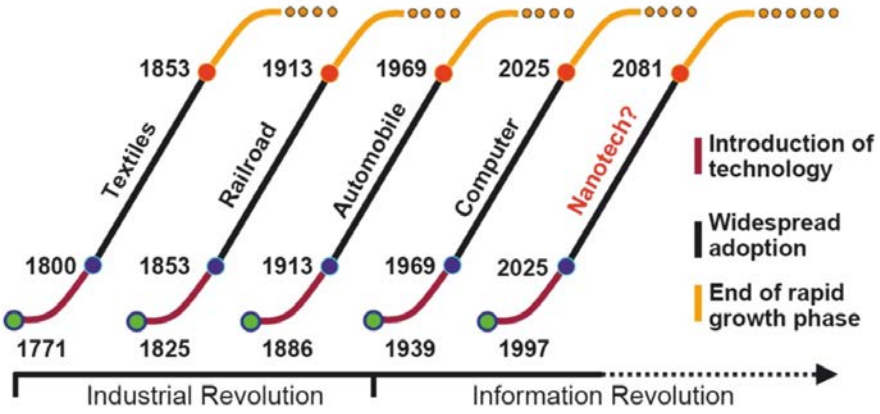

Figure 1 . 2 | Technological revolutions.

In order to characterize and understand properly these materials, it is necessary, if possible, to image them. In the early 1980's two IBM scientists, Binnig & Rohrer (awarded with the Nobel Prize in 1986), developed a new technique, based on a quantum mechanical phenomenon known as "tunnel effect", for studying surface structures, the **Scanning Tunneling Microscopy** (STM). This invention, which only works on a conductive or semi-conductive surface, was quickly followed by the development of a whole family of related techniques which, together with STM, may be classified in the general category of Scanning Probe Microscopy (SPM).

Nowadays STM is considered as an important instrument to inspect surfaces. It allows the direct visualization of metallic or semiconductors samples with exceptional resolution, manipulation of adsorbates, and the measurement of the electronic density of states of the surfaces. As a result, it is a key technique for nanoscopic studies in fundamental and material science.

In 1983, initial STM experiments shown a Si(111)-7×7 surface resolved with atomic resolution[6]. The complex herringbone reconstruction of Au(111) could also be elucidated[7]. Molecules were visualized steering the field of molecular architectonics on surfaces[8] _ENREF_8_ENREF_8 and recently, Dirac materials were explored, which lead to the surprising finding of Majorana fermions[9].

Alternatively, STM became more than a pure imaging tool of surfaces, and manipulation of matter at the nanoscale became feasible. Eigler et al. reported in 1990 the positioning of single Xe atoms on a Ni crystal surface with atomic precision[10]. Some years later Cro-

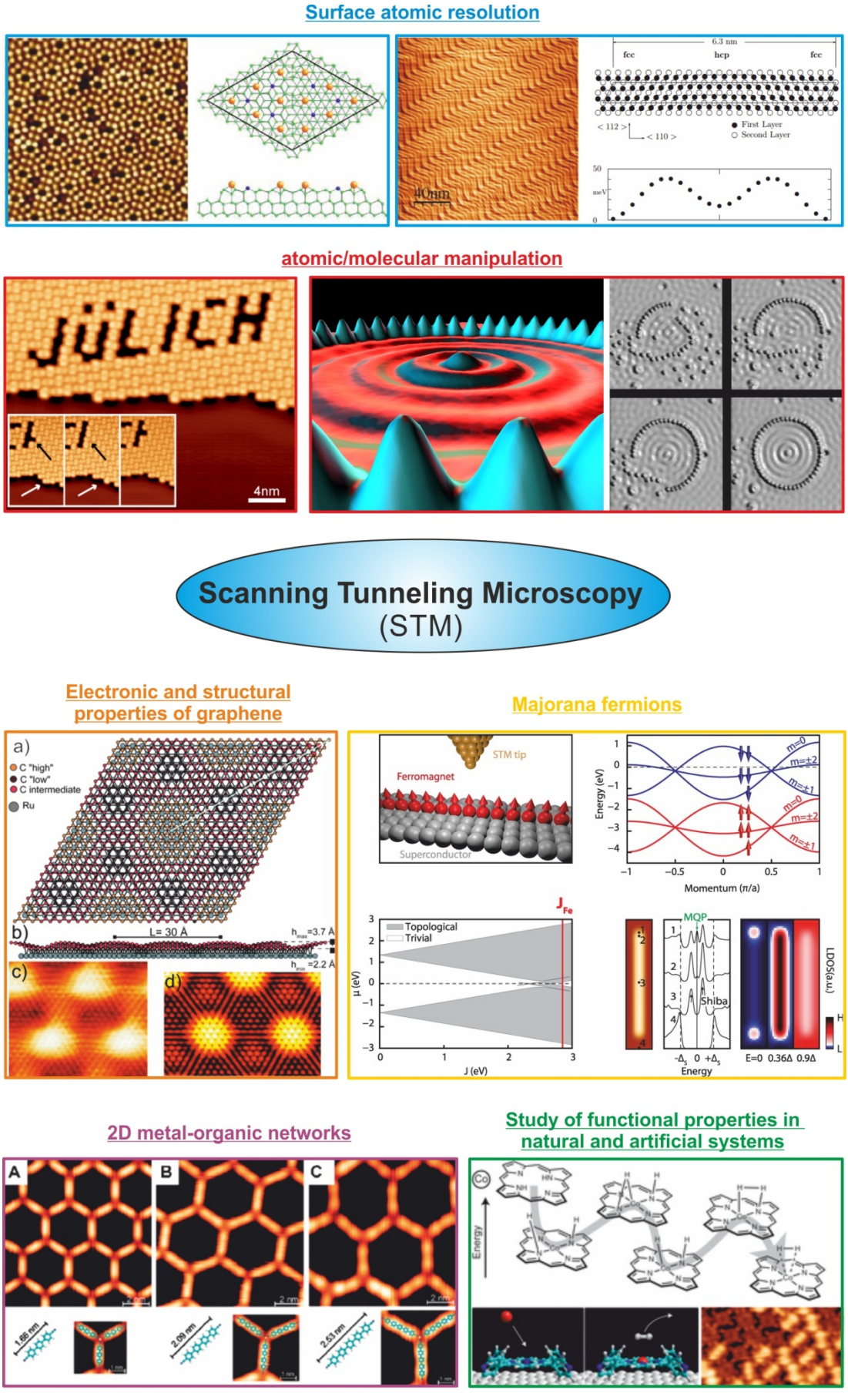

Figure 1 . 3 | Some crucial STM studies

Blue contour, surface atomic resolution of Si(111)–7×7 (left) and Au(111) 22×√ 3 "herringbone" reconstructed surface (right). **Red contour,** molecular manipulation realized by removing individual PTCDA molecules from a PTCDA/Ag(111) monolayer[11] (left) and "quantum coral" from 48 Fe atoms adsorbed on the surface of Cu(111)[12] (right). **Orange contour,** chemical origin of a graphene moiré overlayer on Ru (0001)[13]. **Yellow contour,** topological superconductivity and Majorana fermions in ferromagnetic atomic chains on a superconductor[9]. **Purple contour,** metal-organic honeycomb lattices assembled form ditopic molecular bricks and Co atoms on Ag(111)[14]. **Green contour,** metalation mechanism of porphyrinoid species[15].

mmie et al. created a quantum corral by using Fe atoms on a Cu(111) surface[12]. Recently, IBM researchers have created the world´s smallest movie called "a boy and his atom" by manipulating CO molecules on a copper surface[16].

Parallel to the development of STM, supramolecular chemistry on surfaces emerged as a powerful technique to develop nanoarchitectures with potential impact in a wide variety of fundamental and application fields of research. In particular, the development of surface-confined metallosupramolecular networks of well-defined topology has been recently achieved combining organic molecules and metallic atoms on surfaces. Hereby, the organic linkers are directly deposited on the substrate support, whereas metal atoms can be directly deposited or supplied by the surface. The resulting metal-organic coordination architectures are determined by the properties of the ligands (e.g., donor atoms and their spatial arrangement, steric crowding), the electronic characteristics of the metal atoms (e.g., energy level alignment of orbitals) and the substrate[17,18]. The final assembly is the result of a very delicate balance between molecule-molecule, molecule-metal atom and adsorbates-substrate interactions.

1.2 Intrinsic properties and applications of lanthanide elements

- ***Physico-chemical properties***

Lanthanides (Ln) are strictly defined as the 14 elements following lanthanum (La). They are part of the family of rare earths, which also includes scandium (Sc) and yttrium (Y) due to their chemical similarities and show a gradual variation of their physico-chemical properties, the most relevant of which are:

i) Electronic configuration. Lanthanides present 4f electrons in the valence band, strongly shielded by the occupied $5s^2$ and $5p^6$ orbitals. They exhibit the extended Xe core electronic configuration [Xe] $4f^n$ $5d^0$ $6s^2$ (n = 1-14), with some exceptions: lanthanum (La) and cerium (Ce), where the 4f orbitals have not contracted sufficiently to bring the energy of the 4f electrons below that of the 5d electrons; gadolinium (Gd), where the effect of the half-filled 4f subshell dominates; and lutetium (Lu), the 4f subshell having already been filled at ytterbium (Yb) (see Table 1). In their most stable ionic configuration (Ln^{3+}), electrons are removed first from the 6s and 5d orbitals having [Xe] $4f^n$ arrangements. In addition, the weak overlap of d orbitals with the orbitals of the ligands and the lanthanide contraction contributes to the prevalence of the ionic character in the lanthanide metal-organic complexes. Due to this fact, several of their chemical characteristics are in contrast with the d-block elements where the external d orbitals are sequentially occupied. Some characteristic data of Ln elements are described in Table 1:

	Symbol	Atomic number (Z)	Ground state configuration	Trivalent ionic radius (Å)	
				(CN6)	(CN8)
Lanthanum	La	57	$[Xe]5d^16s^2$	1.032	1.160
Cerium	Ce	58	$[Xe]4f^15d^16s^2$	1.01	1.143
Praseodymium	Pr	59	$[Xe]4f^36s^2$	0.99	1.126
Neodymium	Nd	60	$[Xe]4f^46s^2$	0.983	1.109
Samarium	Sm	62	$[Xe]4f^66s^2$	0.958	1.079
Europium	Eu	63	$[Xe]4f^76s^2$	0.947	1.066
Gadolinium	Gd	64	$[Xe]4f^75d^16s^2$	0.938	1.053
Terbium	Tb	65	$[Xe]4f^96s^2$	0.923	1.040
Dysprosium	Dy	66	$[Xe]4f^{10}6s^2$	0.912	1.027
Holmium	Ho	67	$[Xe]4f^{11}6s^2$	0.901	1.015
Erbium	Er	68	$[Xe]4f^{12}6s^2$	0.890	1.004
Thulium	Tm	69	$[Xe]4f^{13}6s^2$	0.880	0.994
Ytterbium	Yb	70	$[Xe]4f^{14}6s^2$	0.868	0.985
Lutetium	Lu	71	$[Xe]4f^{14}5d^16s^2$	0.861	0.977
Scandium	Sc	21	$[Ar]3d^14s^2$	0.745	0.870
Yttrium	Y	39	$[Kr]4d^15s^2$	0.900	1.019
	Eu^{2+}	—	—	1.17	1.25
	Ce^{4+}	—	—	0.87	0.97

Table 1 | Several characteristics of lanthanide elements

Adapted from reference[19].

In this thesis, three lanthanide elements are used to design lanthanide-directed metallosupramolecular architectures on surfaces, with the following electronic

configurations: cerium (Ce, ground state: [Xe] $4f^1$ $5d^1$ $6s^2$), europium (Eu, ground state: [Xe] $4f^7$ $6s^2$) and gadolinium (Gd, ground state: [Xe] $4f^7$ $5d^1$ $6s^2$).

ii) Oxidation states. The most stable oxidation state for lanthanides is +3 (Ln^{+3}). Generally, the two outer 6s electrons and one taken from the 4f sub-shell are removed from the ground state in order to obtain the +3 oxidation configuration. Nevertheless there are some exceptions where, apart from the 6s electrons, one electron is taken from the 5d sub-shell to maintain the higher stability of empty, half- and fully-filled 4f sub-shell. This is the case of Ce^{+4}, Gd^{+3} and Lu^{+3}. +2 (Ln^{+2}) and +4 (Ln^{+4}) oxidation states are only formed by elements that can maintain the 4f sub-shell empty, half-filled or fully-filled. On the one hand, Eu^{+2} and Yb^{+2} are the most stable di-positive configurations having half-filled and fully-filled the 4f sub-shell, respectively. On the other hand, Ce^{+4} is the most stable tetra-positive cation preserving an empty 4f sub-shell.

iii) Atomic and ionic radius. Both decrease lineally with the increment of the atomic number (lanthanide contraction). Particularly relevant is the relatively large ionic radius (exceeding the ionic radius of s- and d-block metals), which together with the shielding of the f valence electrons, allows high coordination numbers, affording new structural patterns not encountered for the main group of transition metals. Moreover lanthanide metal-organic interactions are determined primary by electrostatic aspects having a substantial effect in the formation, coordination number and reactivity of these complexes.

iv) Magnetic properties. Lanthanides have the largest atomic magnetic moments of all elements. Their local 4f moments are primarily responsible for their magnetism whereby a multitude of magnetic structures due to the 4f-4f coupling mechanism exist, producing long-range magnetic order. In the metallic state, the inter-atomic overlap of the 4f states is small and does not allow direct exchange interaction. Due to a direct intra-atomic exchange between the 4f electrons and the conduction electrons, the conduction electrons mediate a magnetic coupling between the 4f electrons on different lattice sites. Moreover, lanthanides present a strong spin-orbit coupling being especially used as single molecular magnets (SMMs) due to the large spin and unquenched orbital angular momentum interesting for spintronics and future applications like quantum computing, high-density information storage or magnetic refrigeration.

v) Luminescence. Lanthanide ions hold a special place in photonics because of their unique photophysical properties. Their optical characteristics arise due to the distinct features of the electronic [Xe] $4f^n$ configurations creating a rich variety of electronic levels. Lanthanide luminescence spectra are characterized by sharp peaks, whose spectral positions are only slightly sensitive to the ligand employed in the coordination. In particular, the formally forbidden inner-shell 4f-4f transitions are sharp and easily discernable with long lifetimes of the excited states which allows the use of time-resolved detection[20,21] _ENREF_17.

- ***Applications***

Lanthanide elements have an ever-growing variety of applications in modern technology. They have been extensively used due to their catalytic, magnetic and luminescence properties resulting in the development of numerous important applications in particular in the field of bio-imaging as fluorescent probe for fluoro-immunoassays as well as contrast agents for medical magnetic resonance imaging[22,23], biotechnology[24], telecommunications[25], corrosion inhibitors[26], therapeutic applications[27,28], doped nanocrystals[29] and new industrial applications[30].

They possess unique physico-chemical properties owing to a large atomic magnetic moment, strong spin-orbital coupling, high coordination number, and abundant coordination modes of the Ln ions[31]. Thus, several interesting applications arise from their specific properties:

i) Gas storage. The highly porous nature combined with the ability to tune the pore size and their thermal stability make them auspicious candidates for gas storage[32]. Specifically, the incorporation of lanthanide metal ions with carboxylate linkers improves the thermal stability due to the affinity to polarize the O atom causing strong metal-oxygen bonds.

ii) Catalysis. Lanthanide metal ions can possess Lewis acidic sites that are easily functionalized with Lewis bases and other groups within the pores. Furthermore, unlike many other metals, lanthanide metal ions can have wide variation and tunability in their coordination number and modes, producing novel catalytic centers[33,34].

iii) Chemical sensors. The interesting optical properties of lanthanides, which arise from the special features of the electronic [Xe] $4f^n$ configurations, have led to their use in a variety of chemical sensing applications including luminescent probes and sensors. Specially, lanthanide ions have numerous energy levels arising from the f–f transitions, which may make the luminescent spectra usually spanning from ultraviolet (UV) to visible and near infrared (NIR) region[35]. They exhibit unique photoluminescent features, such as sharp absorption and luminescence bands (pure emission lines arising from characteristic 4f electron transitions) and long luminescence lifetimes (ms).

iv) Materials with interesting magnetic properties. The large magnetic anisotropy arising from the strong spin–orbit coupling combined with their optical characteristics makes lanthanide ions very attractive components for functional molecular materials, e.g., magnetic, optical, and magneto-optical materials[36]. Recently, the combination of lanthanides and transition metals has also been employed to construct 3D lanthanide-transition metal MOFs in an attempt to increase the magnetic exchange coupling. To this purpose, the ability of cyano linkers to interact with various metal ions has been explored being considered a promising class of potentially porous magnetic materials[31,37-39].

1.3 Thesis outline

In this thesis we focus on the construction of lanthanide-directed metal-organic coordination networks (Ln-MOCNs) designed on well-defined noble metal surfaces. Many systems including alkali or d-block metals as coordinative nodes in metal-organic assemblies have been inspected in the last years giving rise to well-known 2D nano-structures. However, lanthanide metal-organic coordination nanoarchitectures remained unexplored.

A short summary of the systems studied by LT-STM and VT-STM in this thesis is as follows:

- In chapter three we explore the coordination between carbonitrile functional groups (*p*-NC-$Ph_{3,4}$-CN-*p*) and Ce/Gd f-block elements[40,41] as well as the lateral manipulation of Gd(*p*-NC-Ph_4-CN-*p*)$_5$ supramolecules[42] _ENREF_41.

In particular, we inspect three systems: Ce + *p*-NC-Ph_3-CN-*p*; Ce + *p*-NC-Ph_4-CN-*p* and Gd + *p*-NC-Ph_4-CN-*p*. All these studies have been done using pristine Ag(111) as the substrate. For the surface-confined network constituted by Ce/Gd atoms and *p*-NC-$Ph_{3,4}$-CN-*p* molecular species, three different phases (α, β and γ), reached by adjusting the stoichiometry of the constituents are found.

- Phase α shows a stoichiometry of 1 : 5 (Ce/Gd : *p*-NC-$Ph_{3,4}$-CN-*p*) where the spontaneous expression of supramolecules based on a five-fold planar coordination node is illustrated.

- Phase β shows a stoichiometry of 1 : 4 (Ce/Gd : *p*-NC-$Ph_{3,4}$-CN-*p*) where each lanthanide atom is connected via molecular coordination with two adjacent Ce/Gd atoms, turning out in the formation of dodecameric motifs based on equilateral triangles.
- Phase γ shows a stoichiometry of 2 : 5 (Ce/Gd : *p*-NC-$Ph_{3,4}$-CN-*p*), in which each molecule is doubly coordinated to Ce/Gd atoms, giving rise to complex metal-organic pattern of triangle and square motifs that tessellate the plane according to the semi-regular Archimedean snub square tessellation (3.3.4.3.4). This tessellation was described by Johannes Kepler in the XVI century and it is the first visualization of a 2D supramolecular assembly exhibiting this nanoarchitecture on a surface. In addition, minority semi-regular elongated triangle tilings are also observed.

We have also investigated the lateral manipulation and in-situ design of Gd-supramolecules for the phase α of the Gd + *p*-NC-Ph_4-CN-*p* system. Herein, mononuclear self-assembled pentamers are laterally displaced to a desired position onto the Ag(111) surface. Additionally, the coordination sphere of the pentameric nodes can be intentionally modified giving rise to different metallosupramolecular arrangements.

- In chapter four, we introduce Eu as the lanthanide element, taking into account its electronic structure differences with respect Ce and Gd. We also paid

attention to the importance of the adlayer/substrate interactions introducing Ag(111) and Au(111) as substrate supports.

On the Ag(111) surface, Eu atoms and *p*-NC-Ph_4-CN-*p* linkers form two different phases depending on the Eu : molecular ratio. For a specific stoichiometric ratio 1 : 2 (Eu : *p*-NC-Ph_4-CN-*p*) a well-ordered four-fold square network, never observed with Ce/Gd atoms, arises. For increasing Eu : *p*-NC-Ph_4-CN-*p* stoichiometric ratios (2 : 5), domains of a fully reticulated metal-organic network stabilized by five-fold Eu-carbonitrile bonds emerge. Particularly interesting is the formation of an extended metallosupramolecular coordination network based on the combination 3.3.4.3.4 and 3.3.3.4.4 five-fold coordination motifs. Thus, the expression of four-fold and five-fold coordination networks depending on the stoichiometric ratio Eu : molecular linker is observed and reflects the adaptability of the Eu coordination sphere, determining a characteristic distinction between Eu and Ce/Gd chemical behavior on surfaces.

On the Au(111) surface, Eu atoms and *p*-NC-Ph_4-CN-*p* linkers form manifold coordination networks depending on the stoichiometric ratio Eu : molecular linker. For a specific stoichiometric ratio 2 : 5.1, the expression of a random-tiling quasicrystal is distinguished. Herein, the adequate adlayer/substrate interaction and the low demanding steric restrictions given by the Au surface favored the expression of a random-tiling dodecagonal quasicrystalline structure (ddQC).

- In chapter five, we have taken advantage of orthogonal coordination interactions _ENREF_42, designing a surface-confined d-f heterobimetallic supramolecular nanoarchitecture[43] _ENREF_42. This network, realized by a three-step self-assembly protocol, comprises the formation of four-fold Gd-carbonitrile coordination arrays and in-situ Co metalated porphyrin derivates on Ag(111).

- In chapter six, we introduce carboxylate moieties as linking functional groups creating Gd-carboxylate assemblies on Cu(111) and Ag(111) surfaces.

  On the Cu(111) surface, well-ordered four-fold Gd-carboxylate coordination structures are visualized. More in detail, a coordination number of 8 for the Gd-

O interaction is achieved, exhibiting thermal robustness and having predominantly ionic character[44].

On Ag(111), irregular Gd-carboxylate coordination networks based on a four-fold metal-organic interaction are observed. The formation of extended well-ordered coordination structures is not achieved due to: i) the competition between carboxylic (TDA) and carboxylate (TDA^{2-}) species at room temperature deposition which interferes in the creation of Gd-carboxylate coordination networks. ii) the desorption of TDA species after annealing the sample at higher temperatures.

2. Experimental techniques

This chapter gives a brief overview of the main techniques used in this thesis. Thus, basic principles of the low-temperature scanning tunneling microscope (LT-STM) as well as variable-temperature scanning tunneling microscope (VT-STM) are explained and the corresponding theoretical foundations are concisely introduced. In addition, a short overview of the experimental set-up is presented.

2.1 Scanning tunneling microscopy (STM)

With the invention of the STM in the early 1980´s real space analysis of well-defined conductive (or at least semi-conductive) surfaces became possible. Scanning tunneling microscopy is a technique that exploits the tunnel effect phenomena. It is based on the displacement of a metallic sharp tip onto a conductive surface and the measurement of the current that flows between both electrodes[45,46] (Figure 2.3). This current "*I*" arises from electrons that tunnel between tip and surface due to an applied bias "V_{bias}" and depends exponentially on the vacuum gap width between tip and surface, which are separated a distance of a few angstroms resulting in an overlap of their electronic wave functions.

In the following, the theory of STM, the different modes of operation and the experimental set-up are outlined.

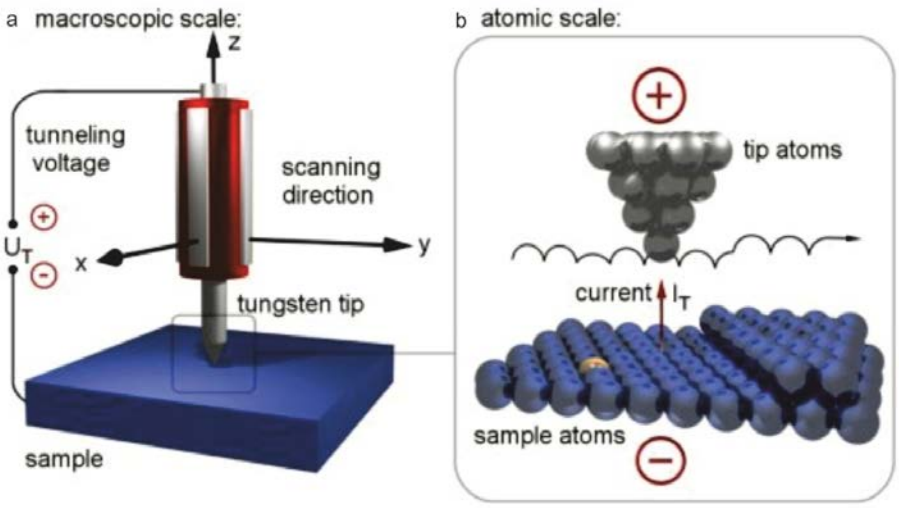

Figure 2 . 1 | Principle of scanning tunneling microscopy

Figure adapted from reference[47].

2.1.1 The tunnel effect. A theoretical approach

Quantum mechanics explains the behavior of matter at the nanoscale. One of its foundational concepts is the "wave-particle duality", which postulates that all particles exhibit both wave and particle properties. A counterintuitive consequence of this concept is the tunnel effect[48-50] (Figure 2.2):

1. From a *classical point of view* if a particle tries to cross a potential barrier larger than its kinetic energy, there is a zero probability that it may traverse the forbidden region and reappear on the other side of the barrier.
2. However, in *quantum mechanics*, this probability is non-zero. Due to the wave nature of the electron, it has a certain probability to pass an energy barrier, even if the energy of the electron is lower than the barrier.

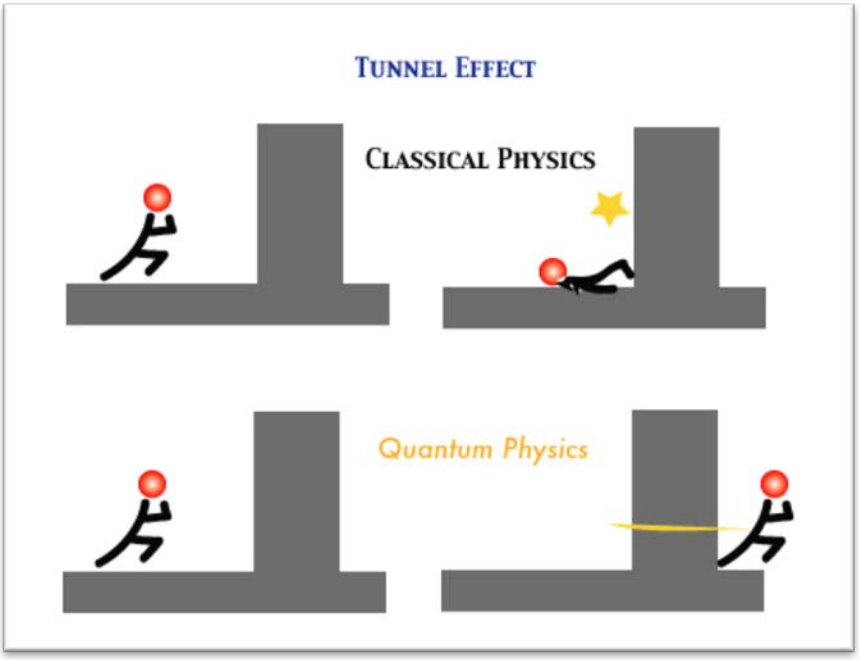

Figure 2 . 2 | Sketch of the tunnel effect from both points of view, classical and quantum physics

Adapted from reference[51].

Electrons are described by wave functions obeying the Schrödinger equation in quantum mechanics:

$$-\frac{\hbar^2}{2m}\frac{d^2}{dx^2}\psi(x)+U(x)\psi(x)=E\psi(x) \tag{2.1}$$

Where m is the mass of an electron, E is the energy, U is the potential barrier and $\hbar$ is the reduced Planck constant. Then, the wave function presented in equation 2.1 presents two possible solutions for both $E > U$ and $E < U$:

$$\psi(x)=\psi(0)e^{-i\frac{\sqrt{2m(E-U)}}{\hbar}x}=\psi(0)e^{\pm ikx} \quad \text{For } E > U \tag{2.2}$$

$$\psi(x)=\psi(0)e^{-\frac{\sqrt{2m(U-E)}}{\hbar}x}=\psi(0)e^{-kx} \quad \text{For } E < U \tag{2.3}$$

Figure 2.2 shows graphically the phenomena in the one dimensional (1D) case. The wave is transmitted with a certain probability through the potential barrier. So if the barrier has a thickness (s) less than the penetration length, there will be a non-vanishing probability for detecting the electron on the other side of the barrier:

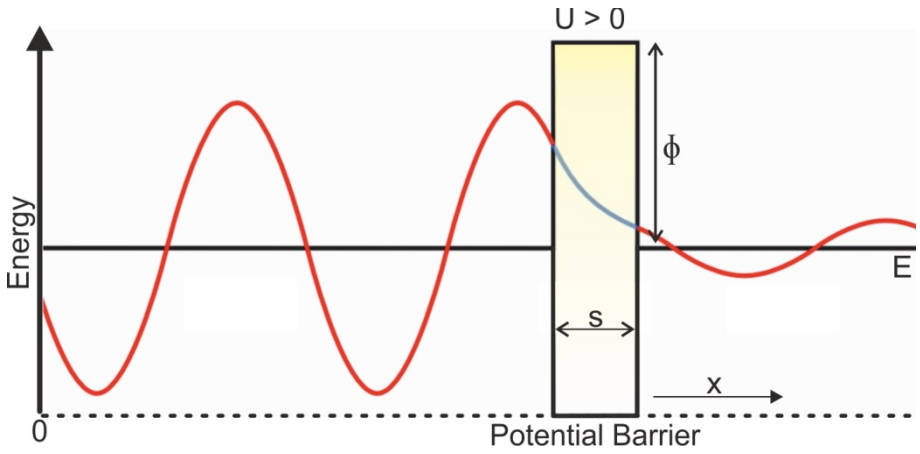

Figure 2 . 3 | Depiction of a particle-wave tunneling through a potential barrier

According to classical mechanics the potential is considered to be impenetrable. Schrödinger's equation gives a solution to the wave function suggesting that the particle could tunnel through the barrier. The wave function exponentially decreases inside the barrier.

For the case of a metal-vacuum-metal junction, the application of a sample bias "V_b" derives in an electron energy eV, that should be much smaller than the work function

"ϕ". Specifically, for the scanning tunneling microscopy, the tunnel effect can be explained as the tunneling of electrons that comes from the tip/sample into the sample/tip through a vacuum barrier. Thus, the probability "Γ" of an electron to tunnel into the tip at a given energy between the Fermi level E_f and $E_f - eV$ is:

$$\Gamma \propto |\psi(x)|^2 = |\psi(0)|^2 e^{-2\frac{\sqrt{2m\Phi}}{\hbar}x} \tag{2.4}$$

If we take into account the all the states in the sample surface between E_f and $E_f - eV$:

$$I_t \propto \sum_{E_f - eV}^{E_f} |\psi(x)|^2 \propto V_b \rho_s(0, E_f) e^{-2\frac{\sqrt{2m\Phi}}{\hbar}x} \tag{2.5}$$

Where I_t is the tunneling current, ρ_s is the local density of states (LDOS) of the sample at the Fermi level (E_f), V_b is the sample bias and x is the tip-sample distance.

Tersoff and Hamann[52], derived from Bardeen´s theory[53], gave an expression for the tunneling current between the two electrodes (tip and surface sample in the case of STM):

$$I_t = \frac{2\pi e}{\hbar} \int_{E_f}^{E_f + eV} \rho_s(E - eV) \rho_t(E) |M_{st}|^2 \, dE \tag{2.6}$$

Also, the above equation shows that the electronic structure of the tip and the sample play a role in the STM[54]. Herein, the density of states of the tip and sample are given by ρ_t and ρ_s, and M_{st} is the transmission matrix between the states of the tip and the surface. The matrix element can be evaluated to obtain the tunneling current under the following assumptions: i) the tip is assumed to be spherical at the apex with radius R, ii) the tip and surface work functions are equal, iii) the angular dependence of wave function of the tip is neglected, i.e. the tip wave function is assumed to be an s-wave function only and iv) the surface wave functions are undistorted.

In order to determine I_t from equation 2.6, Tersoff and Hamann calculated the tunneling matrix element (based in Bardeen´s theory):

$$M_{st} = \frac{\hbar^2}{2m} \int_S (\Psi_s^* \nabla \Psi_t - \Psi_t^* \nabla \Psi_s) dS \tag{2.7}$$

Wave functions are defined as "ψ_t" for tip and "ψ_s" for the sample. The integral is evaluated on a surface S which should be in the vacuum gap between tip and sample surface.

Thus, the Ansatz of Tersoff-Hamann[55] is applied in order to resolve the matrix element M_{st}, including the assumptions given in the previous page. For small bias voltages (V_b) the tunneling current is then proportional to the LDOS of the sample. The tunneling current then reads as:

$$I \propto V_{bias} e^{-2kR} \rho_t(E_f) \rho_s(E_f, r_0) \tag{2.8}$$

Where r_0 is the position of the center of the spherical tip with respect to the surface and $k = \frac{\sqrt{2m\Phi}}{h}$ is the minimum inverse decay length for the wave functions in the vacuum gap with a local barrier height Φ.

An energy diagram of a tunnel transport process in one dimension (1D) is shown in Figure 2.4. Electrons are confined by potential wells with depths equal to the respective work functions Φ_t and Φ_s, respect to the Fermi level. The bias voltage is usually applied to the sample and depending on the distance between tip and sample different scenarios can take place:

- When tip and sample are connected at thermodynamic equilibrium, in close proximity, their Fermi levels are equal (2.4(a)). This situation represents a STM setup with zero bias voltage.
- When a bias voltage V_b is applied to the sample while the tip is at ground, its energy levels are shifted down (for a positive bias (Figure 2.4(b)) or up (for a negative bias (Figure 2.4(c)). In this situation electrons can tunnel through the potential barrier if it is sufficiently narrow and cause a tunneling current.

Therefore, the tunneling current therefore depends on the applied bias voltage V_{bias}, the tip size R, the tip DOS $\rho_t(E_f)$, the sample DOS ρ_s (r_0; E_f) and the tip-sample distance *d*, and it should be seen as a convolution of topographic and electronic information.

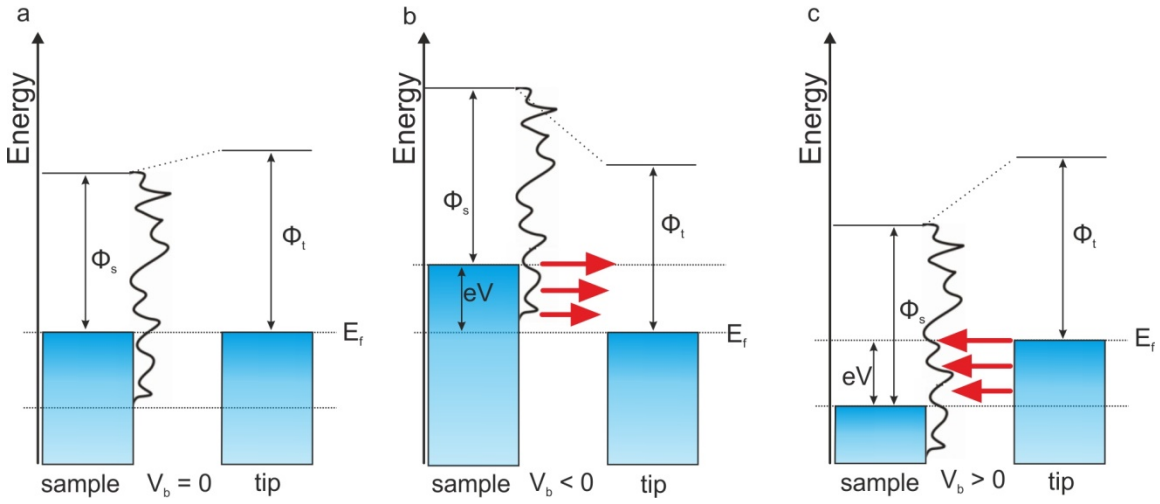

Figure 2 . 4 | Energy diagram describing the electron tunneling through the vacuum junction

a, No sample bias is applied. **b,** Negative bias is applied to the sample. **c,** Positive sample bias is applied to the sample. Initially the Fermi levels (E_f) of the tip and sample are aligned, nevertheless when a negative bias of energy eV is applied to the sample, the Fermi level of the sample shifts by that magnitude eV. The electrons from the occupied states of the sample (in the energy window E_f - eV) tunnel through the vacuum into the unoccupied states of the tip. The electrons are marked as red arrows and the electron close to the E_f experiences the smallest barrier. In the case of positive sample bias, the inverse happens: electrons from the occupied states of the tip tunnel into the unoccupied states of the sample. Adapted from Reference[56].

2.2 Working principles of STM

The basic principles of STM measurements are described in this section.

2.2.1 Operation modes

When the tunneling current is measured, there are two different operational modes that one can use (Figure 2.5):

i) In the constant *Height mode* the tip scans the sample, maintaining the vertical position of the tip constant, while simultaneously recording the current. During each measurement the tip covers a grid xy obtaining I_z values that constitute the surface image. The main advantage of this mode of operation is that it can be used at high scanning frequencies. The disadvantage is that it is only appropriate for atomically flat surfaces as otherwise a tip crash would be inevitable.

ii) In the *Topographic mode (constant current)* a feedback control is used. The tunneling current is set to a value (I_0), then the tip scans the sample measuring in each point the corresponding tunneling current (I). If the current I is different from I_0, the electronic control will send a voltage V_z to the piezoelectrics to bring the tip closer to the surface or to go away from it. During each measurement the tip covers a grid xy obtaining V_z values that constitute the topographic image.

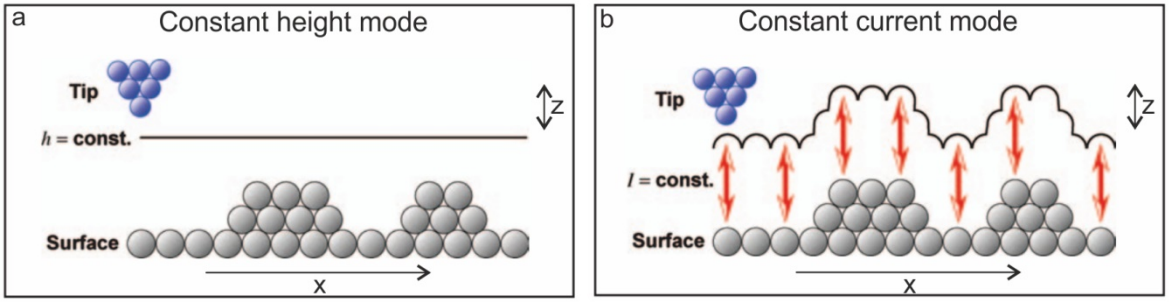

Figure 2 . 5 | Sketch of the two scanning modes in scanning tunneling microscopy

a, Constant-height mode. **b,** Constant-current mode. In **(a)** the measured signal is the tunneling current. In **(b)** the tunneling current is kept constant and the measured signal is the V_z applied to the tip to keep the current constant. Image adapted from reference[57].

2.2.2 Lateral manipulation

A STM manipulation procedure to relocate single atoms/molecules across a surface is known as "lateral manipulation" (LM, Figure 2.6). A typical LM procedure involves three steps: 1) vertically approaching the tip towards the targeted atom to increase the tip-atom interaction, 2) scanning the tip parallel to the surface where the atom moves under the influence of the tip, and 3) retracting the tip back to the normal image-height thereby the atom is left at the final location on the surface.

The nature of atom movements and the type of tip-atom interactions during a LM process can be determined from the STM feedback or tunneling current. Three basic LM modes, "pushing", "pulling" and "sliding", are distinguished. In the "pulling" mode, the atom follows the tip due to an attractive tip-atom interaction[58] _ENREF_9. In the "pushing" mode, a repulsive tip-atom interaction drives the atom to move in front of the

tip. In the "sliding" mode, the atom is virtually bound or trapped under the tip and it moves smoothly across the surface together with the tip.

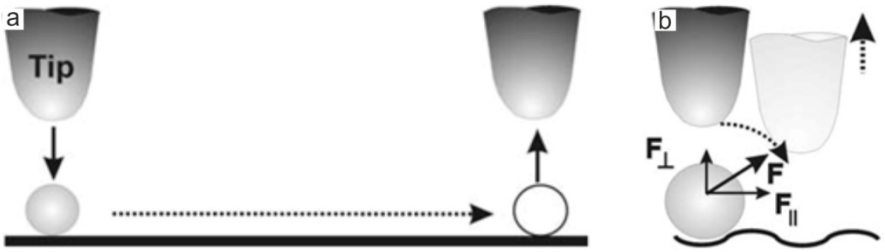

Figure 2 . 6 | Lateral manipulation (LM)

a, A schematic drawing shows the tip action during LM. **b,** the drawing demonstrates the vertical and parallel force components involved in LM. Images adapted from reference[59] _ENREF_57.

2.2.3 Vertical manipulation

Vertical manipulation (VM, Figure 2.7) describes a useful technique, similar to LM, where single atoms or molecules are transferred from tip to surface and vice versa. Thus, the STM tip is used to pick up atoms/molecules by adjusting the variables height and field (set by current and bias).

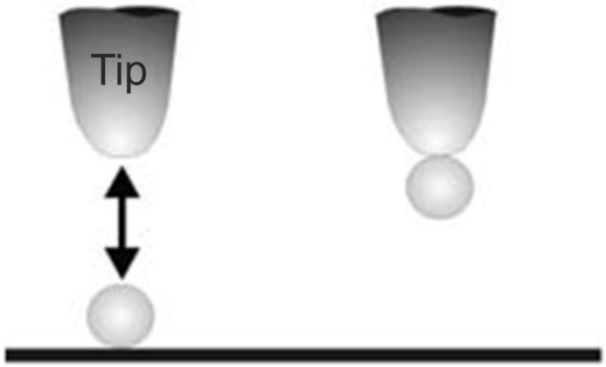

Figure 2 . 7 | Vertical manipulation (VM)

A schematic drawing that shows the process. Image adapted from reference[59] _ENREF_58.

2.2.4 Scanning tunneling spectroscopy (STS)

In a typical STS experiment *I-V* curves and *dI/dV* curves are measured in a specific position of the sample.

From a theoretical point of view, starting from equation 2.8, under the assumption that ρ_t and the transmission matrix M_{st} are independent of *V,* the *dI/dV* signal is directly proportional to the LDOS[60]:

$$\frac{dI}{dV} \propto \rho_s(eV)\rho_t(0) \tag{2.9}$$

As a result, the measurement of dI/dV gives access to the electronic structure of the sample. In order to measure the I-V curves, the tip is stabilized on top of the desired location of the sample (setting a value for I and V_{bias}, and as a result, fixing the tip-sample distance), and then the feedback loop is opened, in order to maintain the tip-sample distance fixed during the experiments. Subsequently, a bias ramp is applied and simultaneously the current in the junction is recorded, getting the I vs V_{bias} curve.

From these data, it could be possible to numerically differentiate and extract the dI/dV data. However, in this thesis we have also recorded the dI/dV vs. V_{bias} data while performing the I-V spectroscopy. To this end, an internal lock-in amplifier is used, which, after superimposing on the sample bias an AC voltage signal of high frequency and small amplitude, is able to extract the dI/dV value per each point of sample bias.

2.3 Experimental set-up

The experiments were performed at three locations, using custom design ultra-high vacuum systems that hosted a Createc low-temperature STM (three years, at TUM with Prof. J. V. Barth, Dr. Willi Auwärter and Dr. David Ecija), a variable temperature Aarhus 150 STM (two months, at IMDEA Nanoscience with Dr. David Ecija), and a variable temperature Omicron (three months, at Hong Kong University of Science and Technology with Prof. Nian Lin). The three systems operate under *Ultra High Vacuum* (UHV) conditions, with base pressures below 2×10^{-10} mbar in the LT-STM system, below 1×10^{-9} mbar in the Aarhus VT-STM, and below 3×10^{-10} mbar in the Omicron VT-STM in order to keep the sample clean during the time of growth and inspection of samples.

2.3.1 LT-STM system

A colored photo of the LT-STM system is depicted in Figure 2.8. It consists of a preparation chamber (blue), an analysis chamber that hosts the LT-STM (yellow) equipped with a cryostat system (red), a manipulator for transferring the samples (green), a pumping equipment (pink) and four dampers to isolate the STM from vibrations (brown).

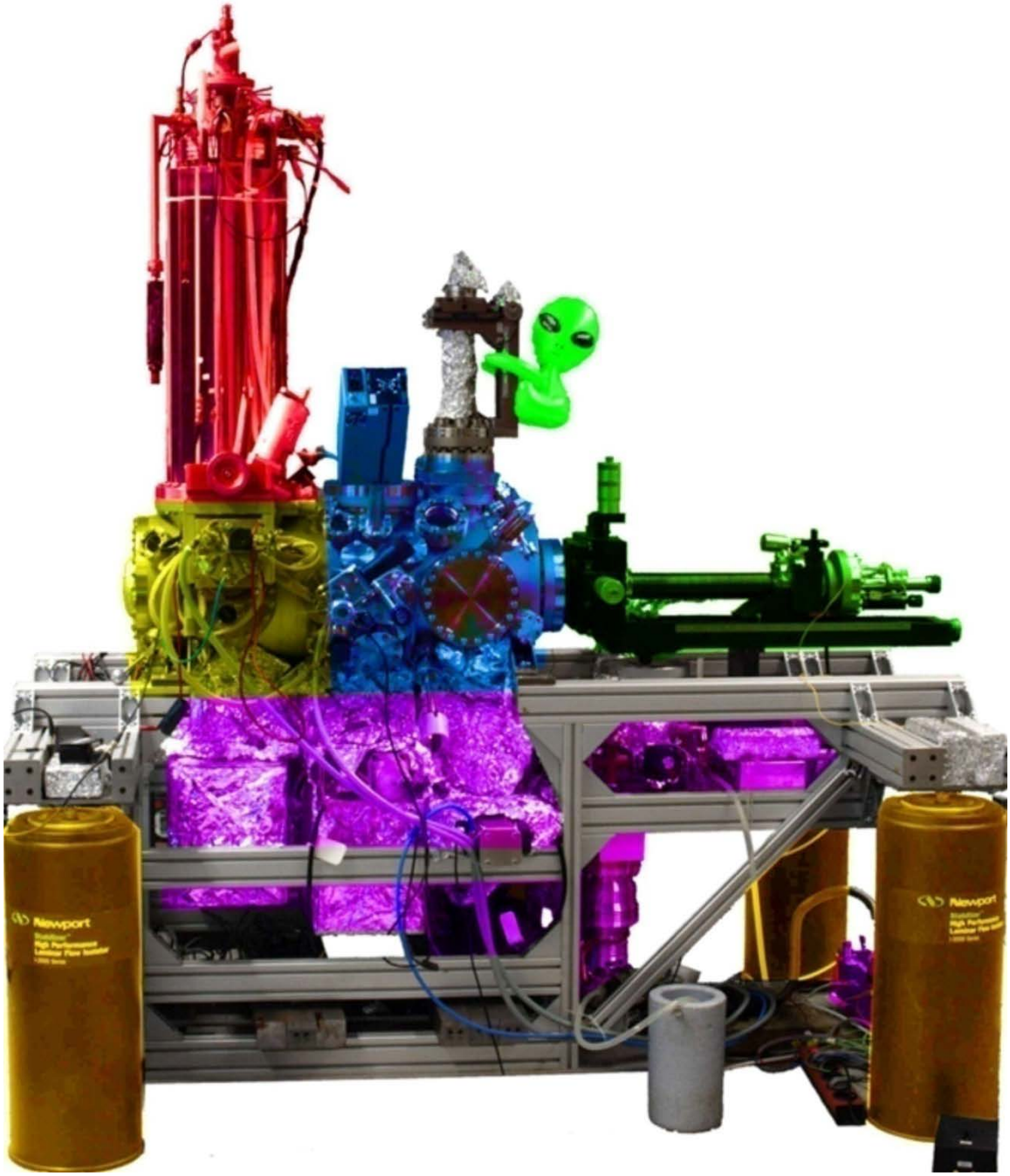

Figure 2 . 8 | Picture of the machine mainly used in this thesis

In red, the cryostat filled with liquid helium and nitrogen is shown. In yellow, the STM chamber, hosting the scanner and an in situ evaporator. In blue, the preparation chamber with several evaporators, leak valves, a mass spectrometer and the possibility to sputter. In green the manipulator used for the sample transfer between the two chambers. In orange colored the dumpers and in purple the whole pumping system. Image used with permission of Dr. Knud Seufert[61].

- ***Pumps***

At the preparation chamber an ion (getter) pump and a series of two turbo-molecular pumps (TMP) and a diaphragm pump (DP) constantly pump to maintain a UHV in the low 10^{-10} mbar range and a combination of a cold trap (CT) and a titanium sublimation pump (TSP) can be additionally run to temporarily lower the pressure. A Ce sublimation pump (CSP) can be used to lower the pressure to the low 10^{-10} mbar range. At the STM-analysis chamber only one ion pump is installed to maintain UHV, but the cryostat also works as a permanent cold trap. The different pumps operate with different pumping techniques that are shortly laid out in the following.

TMPs and DP: Widely used pumps for maintaining an UHV in the range of 10^{-10} mbar are turbo-molecular pumps[62] (TMP). The TMP's operating principle is to transfer momentum from very fast rotating rotors to gas molecules that randomly hit it. The gas molecules are pushed through a stator and then are hit by the next rotor and pushed through the next stator. In that way gas molecules are compressed in many stages and finally led out. In this setup the first TMP transports gas molecules from the preparation chamber to the second TMP after which they are compressed to the pressure of a rough vacuum (P ≈ 2 mbar) and are pumped out by the DP[63]. The DP generates a rough vacuum at a pressure of about 1.5 mbar.

Ion Getter Pump: An ion getter pumps[64] or short just ion pump lowers the pressure by ionizing and accelerating gas molecules and then burying them in a metal. It is built in a sandwich design with an array of parallel steel tubes that form an anode in between two titanium plates as cathodes that are close to the steel tube's open ends. This cathode-anode-cathode configuration is in between the two poles of a strong permanent magnet that applies a magnetic field parallel to the tube's axes. Electrons are emitted from the Ti plates and are accelerated helically in the anodic tubes. On their trajectory they ionize gas molecules which are accelerated towards the cathode and eventually hit it. Due to the impact, titanium atoms are expelled from the surface and the ions are imbedded into the surface. This process is called sputtering and also has a great relevance for preparing a clean sample surface. The sputtered Ti covers the inner walls of the ion pump and reacts chemically with the ions, thus binding them to the walls and extracting them from the vacuum volume.

TSP with Cold Trap: The titanium sublimation pump (TSP) works with a similar techniques as the ion pump. The cold trap (CT) is being filled with liquid nitrogen and, as the name already states, traps free particles by freezing them to the CT's walls. Then a titanium covered lament is heated to sublime Ti onto the CT's walls that reacts with the trapped particles to bind them. Furthermore other particles hitting the Ti film will react chemically as well and be bound permanently.

- ***Analysis chamber: LT-STM***

The analysis chamber hosts the cryostat and the LT-STM. It is separated by a gate valve and is pumped independently by an ion pump.

The cryostat is utilized to cool down the samples to 6 K for inspection, which is very useful to stop thermal diffusion (allow to measure high-resolution STM topographs) and to provide enough energy resolution while acquiring spectroscopic data.

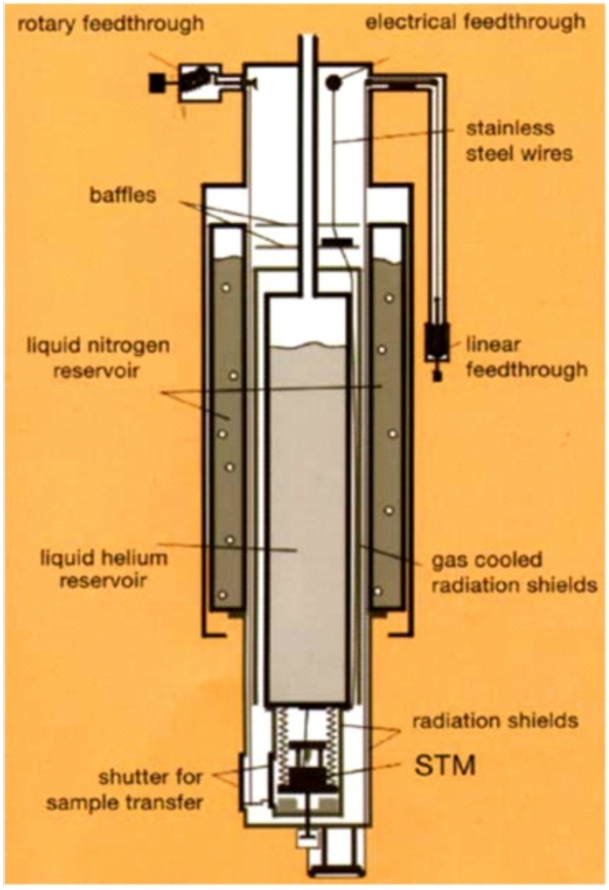

Figure 2 . 9 | Schematic drawing of the cryostat

The inner reservoir for liquid helium (light grey) and the outer one for liquid nitrogen (dark grey). Furthermore the STM scanner and the different feedthroughs are shown. Based on Reference[65].

It consists of two parts: The inner part is filled with liquid Helium and the outer part is filled with liquid Nitrogen. The two parts of the cryostat are separated by UHV to minimize the thermal transport by particles.

The STM set-up comprises three different parts: the tip, the ramp and the sample holder. The ramp is used to perform the coarse vertical approach of the tip towards the sample. It is also involved in the xy movement along the sample. It consists of a base plate on top of three sapphires spheres, each one located on a tubular piezo. The plate is properly designed presenting a slope in such a way that the elongation or contraction of the piezos results in the vertical or lateral movement of the plate. The plate has on its center concentrically placed an inner piezo, into which the tip is magnetically attached. This inner piezo will be used for the feed-back looped approach of the tip towards the sample. Later on, in tunneling conditions, the inner piezo will be responsible of the z displacement, whereas the outer piezos are in charge of the xy movement, thus allowing the decoupling of the xy and z directions.

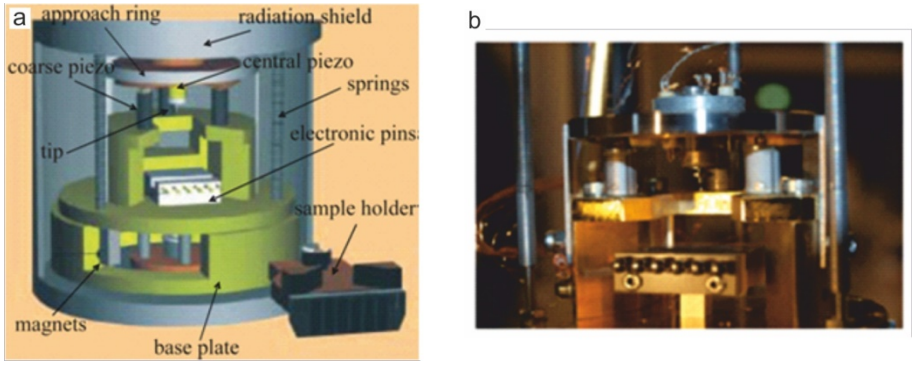

Figure 2 . 10 | Schematic drawing of the piezo tubes (coarse and inner), the tip and the sample holder

a, Schematic drawing adapted from reference[66]. **b,** Original photo from our LT-STM.

An essential feature of the STM is the feedback control loop. At constant current mode, this electronic system maintains the tunneling current constant while moving from point to point, by comparing the current at the measurement point with the set value and then approaching or retracting the tip in order to compensate the difference. Instrumentally, this feedback loop control is performed by a proportional and an integral amplifier and the whole process is regulated by a computer.

The *digital signal processor* (DSP) controls the movement of the STM-tip, the sample bias and the read out of the tunneling current. All these information is sent back and forward to a computer and the measurement software. A sketch of the complete block of electronics is shown in the Figure 2.11.

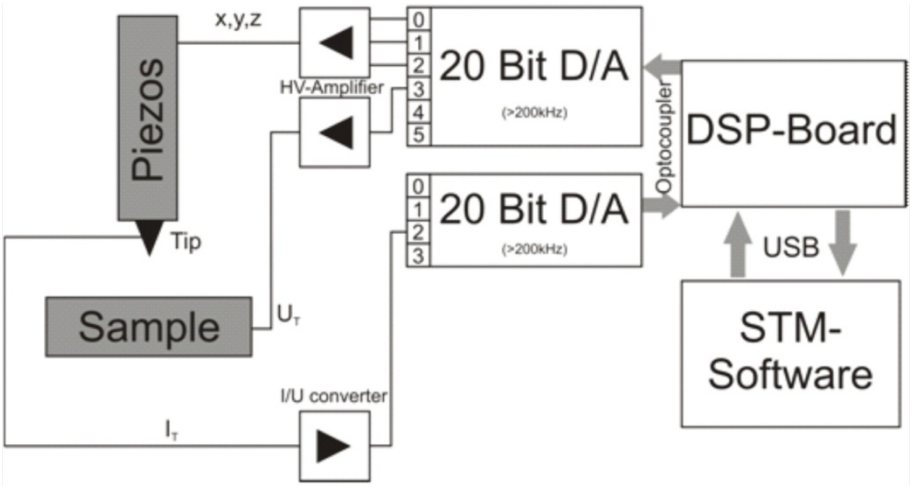

Figure 2 . 11 | Sketch of the complete block of electronics.

Based on reference[67].

The *tip* used for the experiments is an electrochemically etched tungsten wire. The tungsten wire of a diameter of 0.25 mm is placed in a lamella of 2 molar NaOH solution. By applying a bias of 2.5-3.5 V for 15 minutes between the anode (the tungsten wire) and the cathode (wire an aluminum bar) the etching is realized. The chemical reaction responsible for the etching process is:

$$W(s) + 8OH^- \rightarrow WO_4^{-2} + 4H_2O + 6e^-$$

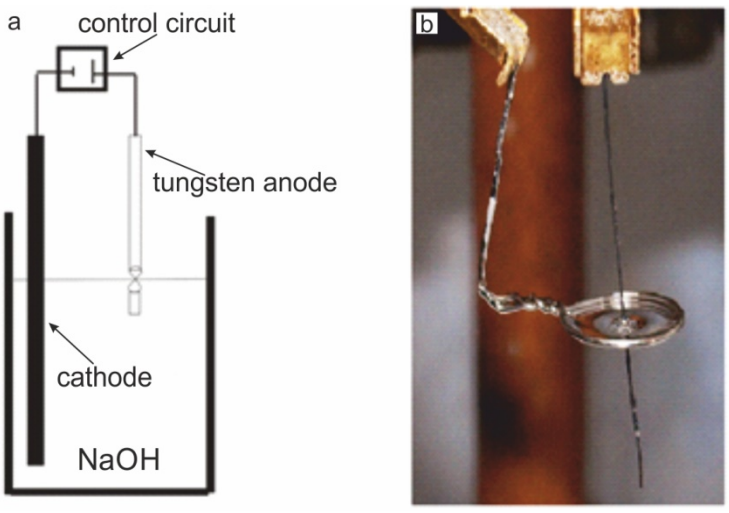

Figure 2 . 12 | Schematic drawing of the tip formation

a, Schematic drawing adapted from reference[66]. **b,** Original photo of the tip formation.

After the reaction the tip is neutralized with distilled water and acetone. Once inside the chamber and for having a better tip termination and cleanliness it can be bombarded by argon ions in a sputtering process. It is feasible to exchange the tip from the STM with the manipulator, since it is magnetically attached to the main piezo.

The *sample holder* is comprised by a gold coated framework, presenting one button heater on one side. The monocrystal is held by a molybdenum clamp onto the button heater. The button heater is used to anneal the monocrystal thermally. A Cr-CrAl contact is also fixed at the button header to record the temperature. The two extremes of the filament are welded on the back-side of the electronic plate, being electrically isolated from each other. In addition, the Cr and the CrAl wires are connected to the remaining slots of the electronic plate. When the sample is placed in the STM one of the slots of the electronic plate is used to apply the bias voltage.

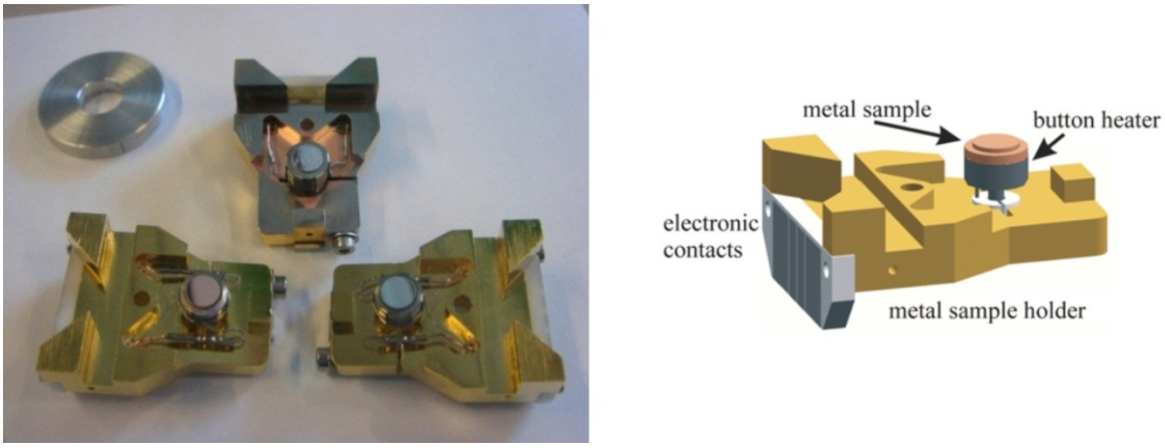

Figure 2 . 13 | Real image and schematic drawing of the sample holder

The schematic drawing is adapted from reference[66].

- ***Preparation Chamber***

The preparation chamber hosts the sputtering gun, the quadrupole mass spectrometer and the molecular beam evaporators. Thus, it is the place where monocrystals are cleaned and samples are grown. In addition, it hosts a manipulator, equipped with feedthroughs for measuring the sample temperature, annealing and cooling the sample used for transferring sample from the STM chamber to the preparation chamber and

vice versa. More information regarding the experiments realized in this thesis is detailed in chapter 9.

i) Sample preparation: All the experiments realized in this thesis were performed on silver (Ag) and copper (Cu) single crystal substrates with a (111) orientation. Ag(111) and Cu(111) have a fcc arrangement of atoms with a nearest neighbor distance of 2.89 Å and 2.55 Å, respectively. The crystals were mounted on a sample holder containing six electrical contacts, two of which are used for measuring the temperature of the sample and two for heating the sample.

ii) Sputtering and annealing: the cleaning of monocrystals is performed by a *sputtering* and *annealing* process where the principal idea is to remove enough atomic layers from the surface by ion bombardment (Ar^+). The preparation chamber is filled up with Ar (P = 2.5×10^{-5} mbar). Then, the Ar atoms passing through a sputter gun are ionized to Ar^+ by the collision of electrons, accelerated with an energy E = 0.8 - 1 keV and directed towards the sample, with an incident sputter current of 3.9 - 4.5 µA.

To recover the surface from the sputtering, an annealing process is performed. The sample is heated and depending on the nature of the sample (Ag in our case) different maximum temperatures are reached, (this temperature should be below 2/3 of the melting point of the material: in our scenario 450°C for Ag). Typically after two cycles of sputtering and annealing, the sample looks clean via STM/STS inspection.

iii) The organic molecular beam epitaxy (OMBE): this technique is used for the deposition of molecules on the surface. The molecules are placed in a quartz crucible, which is annealed thermally by a filament heated to the necessary temperature of sublimation. After stabilizing the temperature of the crucible, the shutter of the OMBE is rotated to open the proper crucible, and then the beam of molecules hit the surface.

Figure 2 . 14 | OMBE showing the four crucibles containing molecules

- ***Lanthanide evaporators***

Two different metal evaporators were used for the experiments realized in this thesis. The deposition of Ce on the surfaces is performed by a homemade *Ce evaporator,* done by resistively heating a W filament enclosing a Ce ball of high purity (around 99.95%). The deposition of Gd and Eu was realized by an e-beam EFM 3i focus evaporator[68] equipped with an ion suppressor that protects the sample against ion bombardment by a repelling lens voltage. Gd and Eu atoms were sublimated from outgassed rods (purity of 99.9% for Gd and 99.5% for Eu, MaTecK GmbH, 52428 Jülich, Germany).

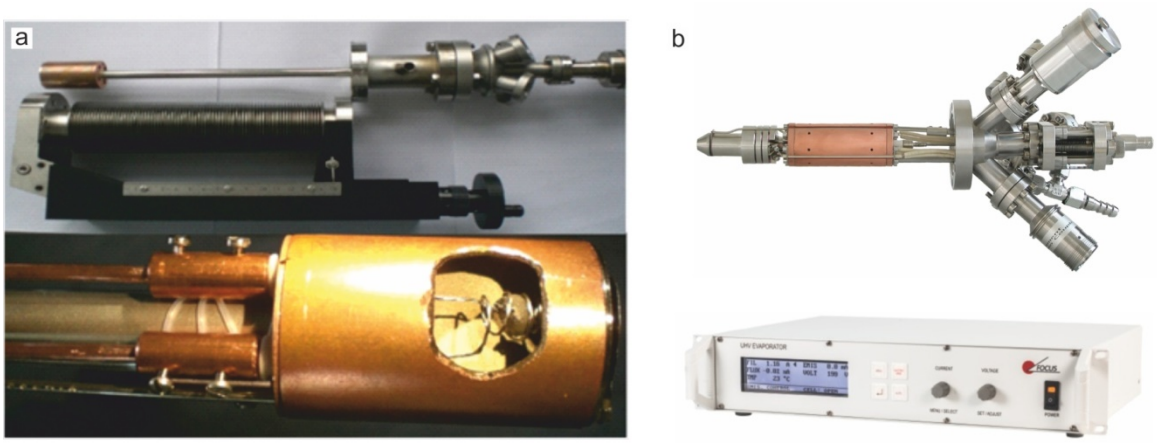

Figure 2 . 15 | Lanthanide evaporators used for the experiments

- ***Vibration isolation***

A possible important disturbance in the STM measurements is the presence of external vibrations. In order to isolate the system from these vibrations, three typical damping mechanisms are used. (i) Both analysis and preparation chambers are mounted on a frame with four damping legs fixed at the corners of the frame avoiding the transmission of low frequency vibrations from the floor. The damping legs are operated with compressed air in order to lift the frame making the system float. (ii) Furthermore, the STM head is suspended on three springs during measurement which guarantees that the STM is not in contact with the base plate inside the chamber thereby attenuating the noise. (iii) Stabilization by eddy current damping in the measurement position is also used to minimize vibrations

2.3.2 VT-STM systems

- ***Aarhus VT-STM***

The VT-STM system consists of a preparation chamber, connected to an analysis chamber that hosts a variable temperature STM. In Figure 2.16, one can see in blue the two vacuum chambers (analysis (A) and preparation (B), respectively) connected via a gate valve. The STM is located in chamber A, whereas chamber B is used for sample preparations. In the preparation chamber there are also parking lots (E) for storing additional samples and a Ce evaporator (F). Both chambers are held under ultrahigh vacuum at a base pressure of 1×10^{-9} mbar.

In this section, to avoid redundancy, we will limit ourselves to the description of the VT-STM. This is a commercial variable-temperature STM microscope, model 150, from SPECS. Remarkably it allows a range of temperatures (from -140 °C to 100 °C) for the measurements.

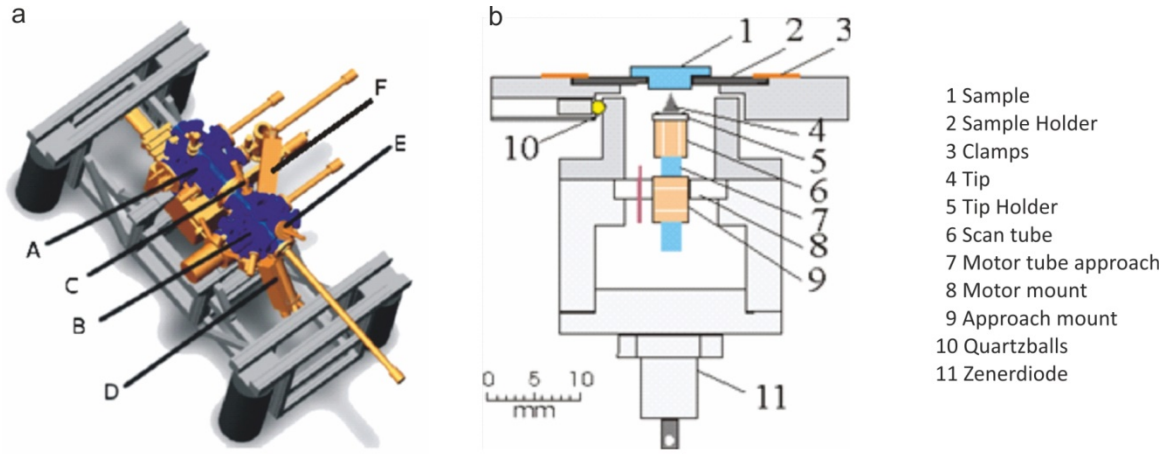

Figure 2 . 16 | Aarhus VT-STM Experimental setup

a, STM head (A), preparation chamber (B), sputter gun (C), OMBE (D), preparation stage (E) and Ce evaporator (F). Adapted from reference[69]. **b,** Sketch of the Aarhus VT-STM head. Adapted from reference[70].

Structurally, the microscope can be divided into two parts, called the sample holder and the scanning block ENREF 69.

Figure 2.16 (b) shows how the sample (1) is placed in a Tantalum sample holder (2), which can be removed from the STM and normally fixed to the top of the STM with two metallic tabs (3). This support is thermally and electrically isolated from the scanner STM by three quartz balls (10) and it is mounted on a block of aluminum which can be cooled to -183 °C or heated to 127 °C. The cooling of the sample is done by nitrogen flow, whereas the annealing is performed by a Zener diode. The Scanning block is based on two piezoelectric tubes: the scanner-piezo scanning and the coarse approach piezo. The tip (4) arranged in the tip-holder is fixed to the end of piezo scanning (6) and is mounted on a tube (7), which together with the approach-piezo constitutes the engine for approaching the tip vertically to the sample into a tunneling regime. The approach-piezo is an inch-worm apparatus divided into three sections, respectively, low, medium and high. The upper and lower section fit perfectly through two bearings to the tube. Applying a positive voltage to the high or low section causes that the respective section to trap the tube, whereas a negative voltage releases the tube. Consequently, with the

correct sequence of voltages applied to the tube, the scanner can move up or down. It can use steps below 2 Å, at maximum speed about 1mm/min. Once the STM has entered into the tunneling regime, the piezo scanning mechanism operates on constant current feedback. A Zener diode is used to keep the scanner at room temperature, in case the sample is inspected at cold temperatures.

- ***Omicron VT-STM***

The ultra-high vacuum system is formed by two chambers: the preparation chamber and the analysis chamber, respectively, separated by a gate valve.

The preparation chamber is used for sample preparation and holds: i) A precision manipulator for transferring the sample holder to the STM chamber that host the scanner. ii) An OMBE used for the growth of samples (detailed explanation in section 2.4.1). iii) Different e-beam metal evaporators used for high-purity evaporation of a wide range of materials in UHV. iv) A sputtering gun needed to remove atomic layers from the surface by ion bombardment (Ar^+). v) Pumps used to maintain the UHV, specifically a turbo molecular drag pump, two ion getter pumps (IGP) and a titanium sublimation pumps (TSP).

The analysis chamber contains the STM, which was manufactured by Omicron Nanotechnology GmbH[71].

The STM head is mounted on a platform which is spring suspended inside the UHV chamber (cf. Figure 2.17 (b)), a parking where sample holders can be placed and a turbo molecular drag pump to keep the UHV. Herein, the tip movement is carried out by piezo ceramics. The tip is supported magnetically on a tip holder coupled to the scanner. The VT-STM uses two sets of piezos: one set for the coarse approach and the other one for the fine (controlled) approach, both of them allowing movement in x,y and z directions. For the fine approach, a tube scanner that consists on multiple electrodes is implemented. The maximum travel is limited to 12 × 12 μm^2 laterally and 1.5 µm in z direction. Finally, the measured output signals are passed through a preamplifier (Omicron SPM Pre 4) outside the STM into the control unit (Omicron Matrix SPM-CU).

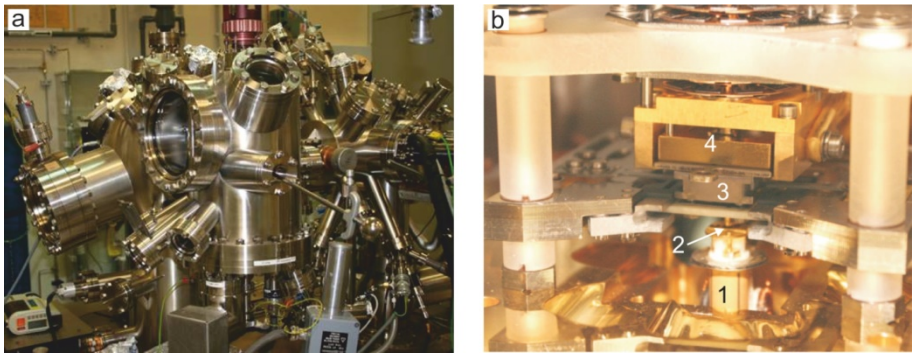

Figure 2 . 17 | Omicron VT-STM experimental setup

a, Ultra-high vacuum Omicron variable-temperature STM system at Nian Lin´s group (HKUST, Hong Kong University of Science and Technology). Image adapted from reference[72]. **b,** VT-STM head. Herein, (1) shows the tip holder with a tip pointing upwards (2), (3) shows the sample plate and (4) the clamping block for thermal coupling to the cryostat. Image adapted from reference[73].

3. Five-fold lanthanide (Ce/Gd)-carbonitrile coordination on surfaces

During the last decades, supramolecular chemistry on surfaces has emerged as a skillful strategy to design surface-confined nanoarchitectures[18,74,75]. _ENREF_2 _ENREF_2 In particular, conjugated polyaromatic molecules like Oligo (p-phenyl)s have been intensely investigated due to their important electronic and optical properties as well as the ability of fine-tuning their properties through functional group manipulation[76-78].

Protocols relying on metal-directed assembly provide frequently an excellent option given their advantageous performance with respect to the robustness and spatial regularity. Accordingly, several procedures were introduced in order to exploit the coordination capabilities of transition metals and their affinity to molecular species specially equipped with carbonitrile[14,79,80], pyridyl[81-84] _ENREF_79 or carboxylate functional groups[85-87]. Therefore, this approach should be extended to the unexplored lanthanide family of elements, with exceptional chemical, optical and magnetic properties[88] _ENREF_86, giving rise to the first designs based on Ln-carbonitrile motifs.

3.1 The importance of five-fold symmetry

The property of being five-fold appears to play a crucial role in diverse fields ranging from natural and applied sciences like biology, chemistry, physics and architecture to social sciences or art[89]. This relevance is mainly attributed to the intimate connection between the five-fold symmetry and the golden number (φ = 1.618…) because φ itself is inherently linked to the number five, trigonometrically and mathematically speaking. Importantly, some statements claim that the golden number was used by Leonardo da Vinci in the painting of “La Gioconda”, in the Parthenon built by the ancient Greeks in the V century BC and by ancient Egyptians in the construction of the Great Pyramid of Khufu at Giza around 2560 BC. In addition, the golden number or golden ratio is in-depth relation with the Fibonacci series due to the fact that the ratio between two consecutive

numbers in the Fibonacci series seems to be settling down to a specific value which is the golden number. Extensive literature on the relation between the golden number and the Fibonacci series is summarized elsewhere[90].

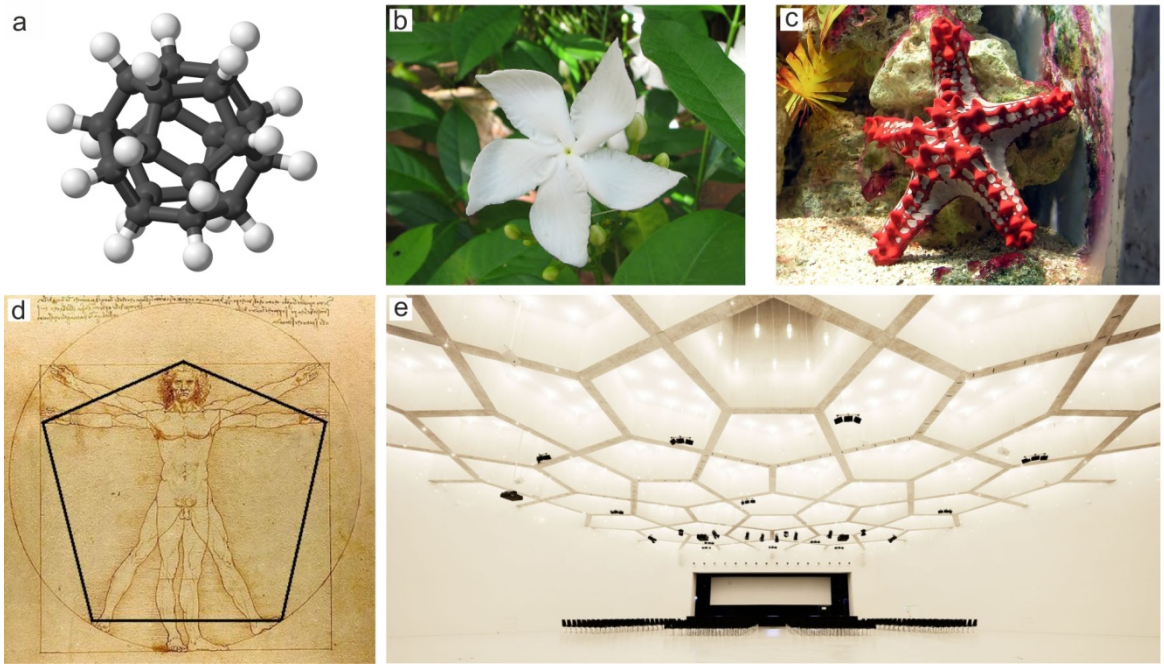

Figure 3 . 1 | Five-fold in diverse fields

a, Dodecahedrane molecule ($C_{20}H_{20}$)[91] _ENREF_81. Every vertex presents a carbon atom that bonds to three neighbouring carbon atoms. **b,** *Tabernaemontana corymbosa*, a species of plant of the Apocynaceae family that shows five white petals[92]. **c,** The red-knobbed starfish (*Protoreaster linckii*), also known as the red spine star that demonstrates the presence of five-fold symmetry in the animal kingdom[93]. **d,** Vitruvius Pollio drew by Leonardo Da Vinci. Herein, the human body is drawn as a regular pentagon[94] _ENREF_92. **e,** Pentagonal ceiling in a congress hall (Davos, Switzerland)[95].

In the two-dimensional world, the absence of translational symmetry is noteworthy in five-fold architectures. The Euclidean space can be fully and symmetrically filled with tiles of 3, 4 and 6 sides, nevertheless it was believed that it was impossible to fill an area with a pentagon. This symmetry mismatch has fascinated mankind for several centuries. For instance, it captivated Johannes Kepler, who is doubtless better known for his work in astronomy, in particular because of his three laws regarding planetary motion, though also very much interested in tessellations and polyhedra.

Thus, Johannes Kepler accomplished a rigorous analysis revealing four centuries ago that eleven tessellations based on symmetric polygonal units exist in the Euclidean plane:

three consist of a specific polygon (so-called regular tilings with squares, triangles or hexagons, respectively), whereas eight require the combination of two or more different polygons (named semi-regular or Archimedean tilings from triangles, squares, hexagons, octagons and dodecagons)[96]. Specifically, three of the semi-regular Archimedean tilings correspond to five-vertex configurations (section 3.2.3).

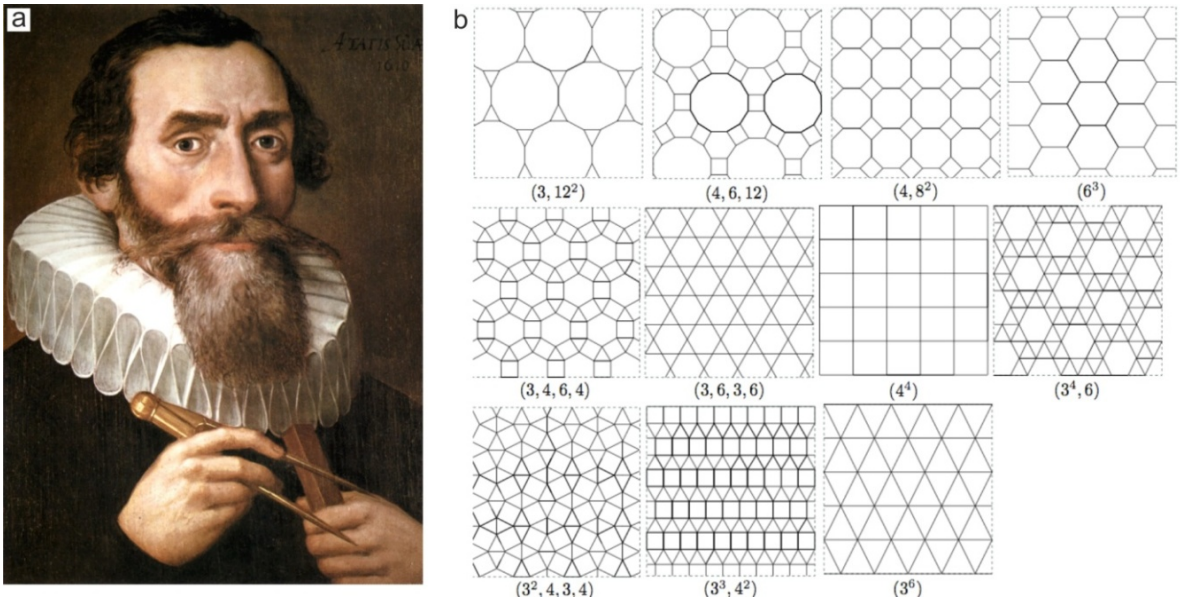

Figure 3 . 2 | Euclidean Archimedean tessellations

a, Johannes Kepler´s portrait. Image adapted from reference[97]. **b,** Eleven Archimedean tilings in which all polygons are regular and each vertex is surrounded by the same sequence of polygons[98]. For instance, the notation (3^3, 4^2) means that every vertex is surrounded by three triangles and two squares.

In the field of surface science, manifestations of regular tessellations at the atomic and molecular level are widespread, including crystalline planes and surfaces of elemental or molecular crystals, and honeycomb structures encountered, e.g., for graphene sheets, strain-relief patterns and supramolecular lattices. In addition, the family of semi-regular Archimedean tilings features intriguing characteristics. They have been identified in bulk materials, such as layered crystalline structures of complex metallic alloys, supramolecular dendritic liquids, liquid crystals, and special star-branched polymers and may represent geometrically frustrated magnets[99] or provide novel routes for constructing photonic crystals[100] _ENREF_97. Moreover, recent experiments with colloids at a quasicrystalline substrate potential induced by five interfering laser beams, conceived to specifically address the surface tiling problem, yielded a distorted, 2D

Archimedean-like architecture[101]. However, with the exception of the frequently addressed trihexagonal tiling[102-104] (also known as the kagomé lattice), the other semi-regular Archimedean tiling patterns remain largely unexplored.

In this section we introduce a novel approach towards complex surface tessellations by the combination of lanthanide metal atoms with linear dicarbonitrile molecular linkers on a smooth Ag(111) substrate. Our molecular-level scanning tunneling microscopy (STM) observations reveal the expression of distinct five-fold coordination nodes, which are flexible and thus useful for complex periodic surface tessellations, including the five-vertex semi-regular Archimedean snub square tiling. A further important aspect of the 2D lanthanide metal-organic coordination networks is the integration of f-block elements, which bears promise for a new generation of surface nanoarchitectures.

LT-STM and VT-STM experiments realized in this chapter were carried out at TUM. DFT simulations were performed by Dr. Ari Paavo Seitsonen at Universität Zürich, Switzerland.

3.2 Five-vertex lanthanide coordination: *p*-NC-(Ph)$_{3,4}$-CN-*p* + Ce/Gd

Dicarbonitrile-polyphenyl species have been previously used for the engineering of 2D metal-organic networks on surfaces with transition metal atoms, where three- and four-fold coordination nodes prevail[14,79]. In bulk chemistry lanthanide ions present high coordination numbers, ranging from 6 to 12[88] ENREF_105. Accordingly, lanthanide elements are promising candidates to explore high coordination number metal-ligand chemistry on surfaces.

Specifically, terphenyl-4,4''-dicarbonitrile species (*p*-NC-(Ph)$_3$-CN-*p* (linker **1)**, Figure 3.3 (a)) and quaterphenyl-4,4''-dicarbonitrile species (*p*-NC-(Ph)$_4$-CN-*p* (linker **2)**, Figure 3.3 (d)) organic molecules, which chemical synthesis is based on a Suzuki coupling scheme, were used in our lanthanide coordination investigations.

Depending on the length of the linear molecular building block, the network arrangement varies on the Ag(111) surface[103] (Figure 3.3). Linker **1** forms a densely packed chevron-like pattern with molecules lying along two different directions for a

given domain. The introduction of an additional phenyl ring in the molecular backbone generates a spreading in the molecular assembly, giving rise to rhombic chiral cavities (Figure 3.3(e-f)). Both architectures are stabilized by the N···H interaction (selective and directional) between two axial carbonitrile groups and hydrogen atoms of adjacent molecules. The distance between the nitrogen of the carbonitrile groups and the hydrogen ranges from 2.3 to 3.3 Å which is reasonable taking into account the nature of the interaction.

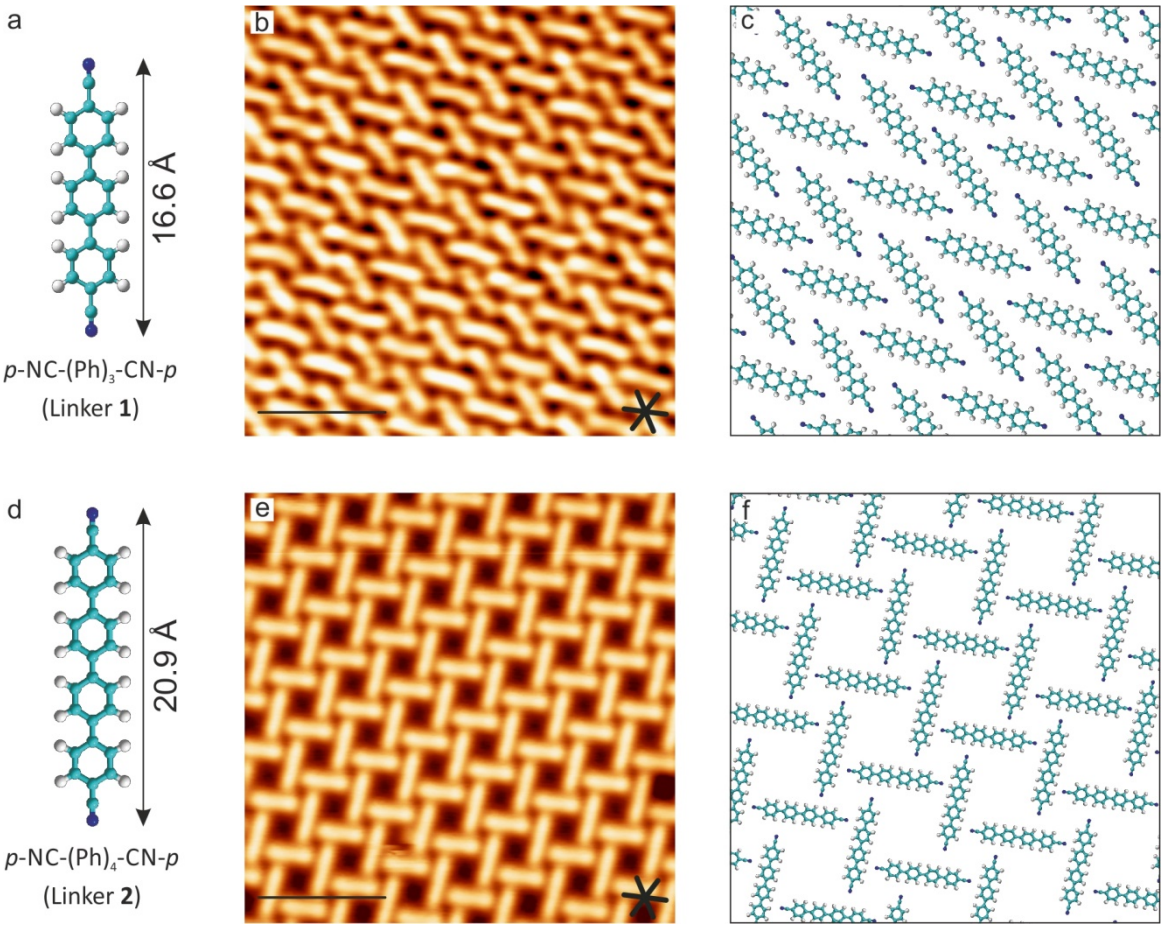

Figure 3 . 3 |Molecular self-assembled networks of *p*-NC-(Ph)$_{3,4}$-CN-*p* species on Ag(111)

a, d Atomistic models of molecular building blocks with their respective lengths (green, C; dark blue, N; white, H). **b,** High-resolution STM image displaying the densely packed chevron layer formed by *p*-NC-(Ph)$_3$-CN-*p* species. **c,** Atomistic model of the molecular self-assembled network presented in **(b)**. **e,** High-resolution STM image displaying an open rhombic network formed by *p*-NC-(Ph)$_4$-CN-*p* species. **f,** Atomistic model of the molecular self-assembled network presented in **(e)**. **b,e** Scanning conditions: V_b = 0.2 V, I = 83 pA; Scale bar: 5 nm.

Upon deposition of Ce or Gd atoms onto the precursor layer a flexible five-fold Ce (Gd)-linker coordination is detected[40,41] changing completely the former scenario (Figure 3.4). In particular, in this chapter we inspect the supramolecular assemblies created by depositing Ce and linker **1**, Ce and linker **2**, and Gd and linker **2** on the selected substrate. Remarkably, we have observed that these nanoarchitectures are equivalent, independently of the lanthanide employed (Ce or Gd), due to their chemical similarities. Thus, depending on the ratio lanthanide : molecular linker, the presence of different phases based on a flexible five-fold Ce (Gd)-linker coordination is detected.

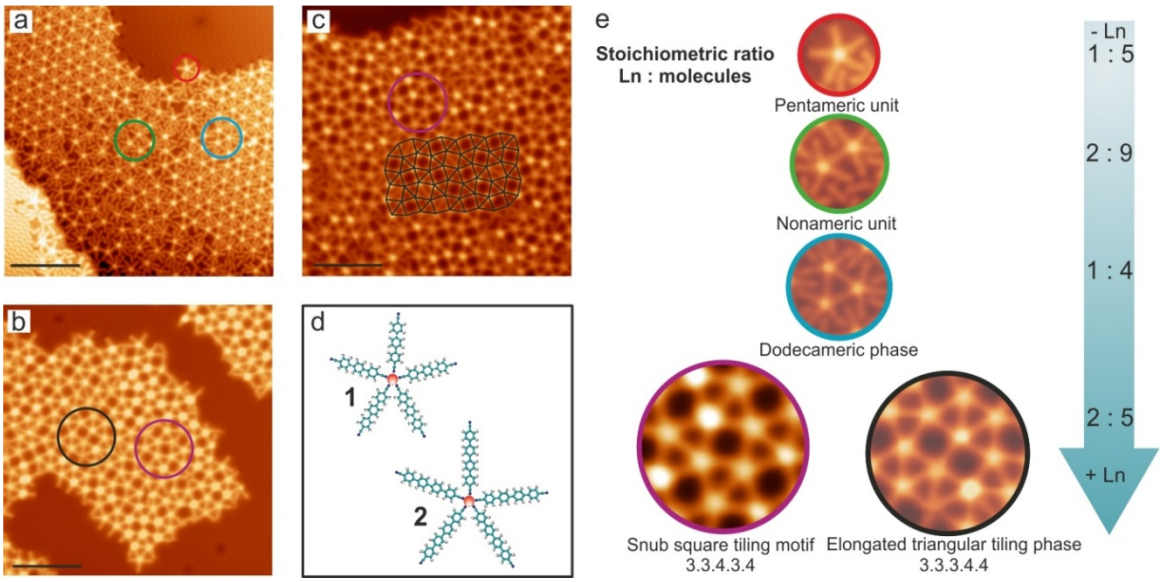

Figure 3 . 4 | Five-vertex lanthanide supramolecular architectures on Ag(111)

a, Large-scale STM image displaying the coexistence of the disordered phase α and the dodecameric phase β, obtained by mixing linker 1 and Ce with a local stoichiometric ratio (Ce : molecule) close to 1 : 4 (V_b = 0.2 V, I = 80 pA). **b-c,** Large-scale STM images of the snub square Archimedean tessellation and elongated triangular tiling phase on Ag(111), achieved by mixing linker **2** and Ce with a local stoichiometric ratio (Ce : molecule) of ≈ 2 : 5 (V_b = 0.2 V, I = 70 pA). Black lines in **c** drawn to connect the Ce centers highlight the triangular and square tiles, which combine in a 3.3.4.3.4 fashion, i.e. the snub square Archimedean tiling. **a-c,** Scale bar: 10 nm. **d,** Sketch of the five-fold Ce(*p*-NC-(Ph)$_3$-CN-*p*)$_5$ (**1**) and the Ce/Gd(*p*-NC-(Ph)$_4$-CN-*p*)$_5$ (**2**) pentameric units. C, N, H, and Ce atoms are depicted in green, violet, white, and red, respectively. **e,** Zoom-in of **(a-c)** showing with high-resolution the pentameric, nonameric, and dodecameric units, and the snub square Archimedean tiling motif, respectively.

3.2.1 Supramolecular pentameric units (phase α)

For small surface concentrations and a Ce/Gd to linker stoichiometric ratio around 1 : 5, individual pentameric units made of linker **1** and Ce (cf. Figure 3.5(a,e)), linker **2** and Ce (cf. Figure 3.5(b,f)) or linker **2** and Gd (cf. Figure 3.5(c,d,g)) are visualized in separated experiments. Herein, organic molecules are imaged like rods, whereas the Ce/Gd atoms appear as bright protrusions. Usually, the pentamers are found isolated near steps or forming disordered patches.

The spontaneous expression of this five-fold planar coordination node is atypical in two-dimensional metal-organic architectures and diverges from the bonding motifs found for the coordination of the same linkers with transition metals. The five-fold lateral coordination expression of the lanthanide node by the carbonitrile units can be justified mainly because of the size of the lanthanide and its propensity towards high coordination numbers, the surface confinement of the linkers, and possible steric limitations at the coordination sphere, where the phenyl rings come rather close, thus preventing higher coordination numbers. Remarkably, the geometry of pentameric species reveals a high degree of flexibility, exhibiting opening angles between two adjacent molecular linkers deviating from the ideal 72° pentagonal angle and ranging from 60° ± 5° to 85° ± 5°, as confirmed by STM images before and after voltage pulses (cf. Figure 3.5(c,d,g)).

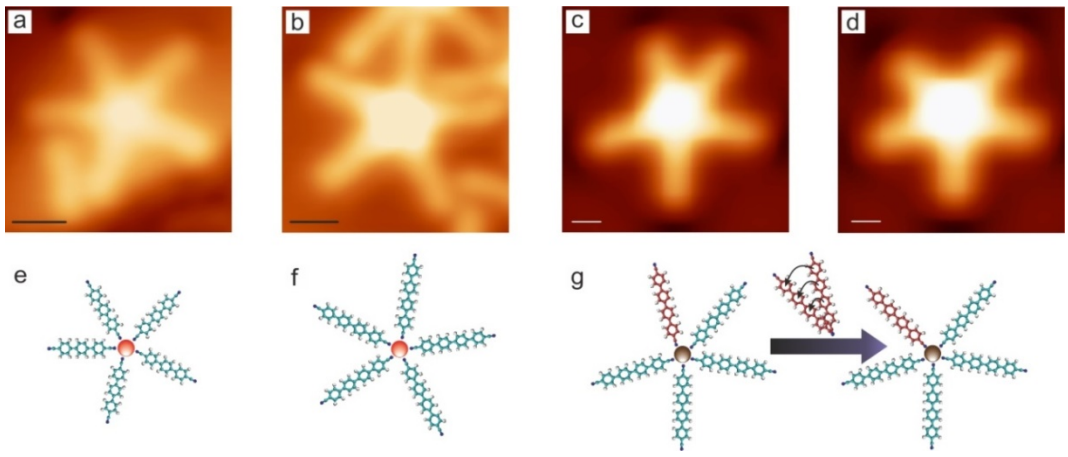

Figure 3 . 5 | Individual Supramolecular pentameric units based on a five-fold Ce/Gd coordination to dicarbonitrile polyphenyl linkers 1 and 2 on Ag(111)

a, STM image of a Ce(linker 1)$_5$ pentameric unit (V_b = 0.2 V, I = 50 pA). **b,** STM image of a Ce(linker 2)$_5$ supramolecule (V_b = 0.2 V, I = 100 pA). **c-d,** STM images of a Gd(linker 2)$_5$ pentamer displaying conformational flexibility before and after applying a voltage pulse with the STM tip (V_b = -0.02 V, I = 100 pA). Scale bar in **a-d**: 1 nm. **e-g,** Atomistic models of **(a-d)** where C, N, H, Ce, and Gd atoms are depicted in green (maroon), violet, white, red, and brown, respectively. Maroon is used to highlight the C atoms of the linker that was manipulated by the tip.

Lateral manipulation experiments of the pentamers reveal the robustness of the supramolecules and highlight the adequate balance between flexibility and strength of the lanthanide-linker coordination required to produce the advanced networks at higher Ce/Gd : molecule stoichiometries (cf. above). In addition, a more detailed study of pentamer´s lateral manipulation will be shown in section 3.3.

In order to complement our experimental findings, we got support from density functional theory (DFT) calculations involving *p*-NC-Ph$_3$-CN-*p* species and Ce atoms. The purely molecular phase on the surface is studied, and after the relaxation of the chevron supramolecular structure the binding energy was 2.69 eV per molecule compared to the free molecules in the gas phase. The average height of the carbon atoms in the molecules is 3.17 Å above the first layer of the substrate. Upon adsorption on the Ag(111) surface the molecules become much more flat with the average phenyl dihedral angle being 0.9° and the phenyl rings oriented parallel with respect to the surface (for comparison in the gas phase molecule this dihedral angle is 38.5°)[105]. The flattening of the molecule is in agreement with the small distortion energy of the molecule, 0.18 eV between the flat rotated conformations in gas phase. The final value of the average dihedral angle is a competition among: i) the van der Waals forces between the molecular species and the surface, which tend to flatten the molecule in order to make the phenyls approach the surface more before the Pauli-repulsion limits the adsorption height, ii) the steric hindrance of the phenyl rings, which favors non-planarity; and iii) the resulting supramolecular packing on the surface, which due to intermolecular interactions interferes with the rotation of the phenyls. In this sense, for submonolayer *p*-NC-Ph$_4$-CN-*p* species adsorbed on Ag(111) it was reported that the terminal benzonitrile groups are planar on the surface. It was suggested that the absence of packing constraints in the submonolayer regime, together with the lateral

supramolecular hydrogen bonds planarize the terminal groups. Since the supramolecular chevron pattern formed by *p*-NC-Ph_3-CN-*p* species on Ag(111) presents more CN···H bonds per molecule than the supramolecular assembly exhibited by *p*-NC-Ph_4-CN-*p* linkers, it is reasonable to assume a higher planarization of the phenyl rings in the case of species **1** as compared with linkers **2**, which is in agreement with our simulations.

Subsequently, we have inspected a pentameric supramolecule adsorbed on Ag(111), comprising five *p*-NC-Ph_3-CN-*p* species coordinated to one Ce atom. Figure 3.6 depicts the relaxed geometry. The Ce atom is located 2.64 Å above the first substrate layer. The average Ce-N distance is 2.58 Å, in good agreement with our experimental values, and the C-N bond length (1.17 Å) of the carbonitrile group bound to the Ce has hardly increased ($\Delta d < 0.01$ Å) due to the bonding. The molecules are again flatter than in the gas phase, with an average dihedral angle of about 10°, their height from the substrate is almost unaltered at 3.14 Å, and the molecular backbone lies parallel to the surface. The binding energy of the linker molecules in this structure is 3.26 eV, thus considerably higher than in the molecular phase: the Ce-linker bond strength exceeds the molecule-molecule interaction in the molecule-only phase, and the linker-substrate interaction is similar in both cases.

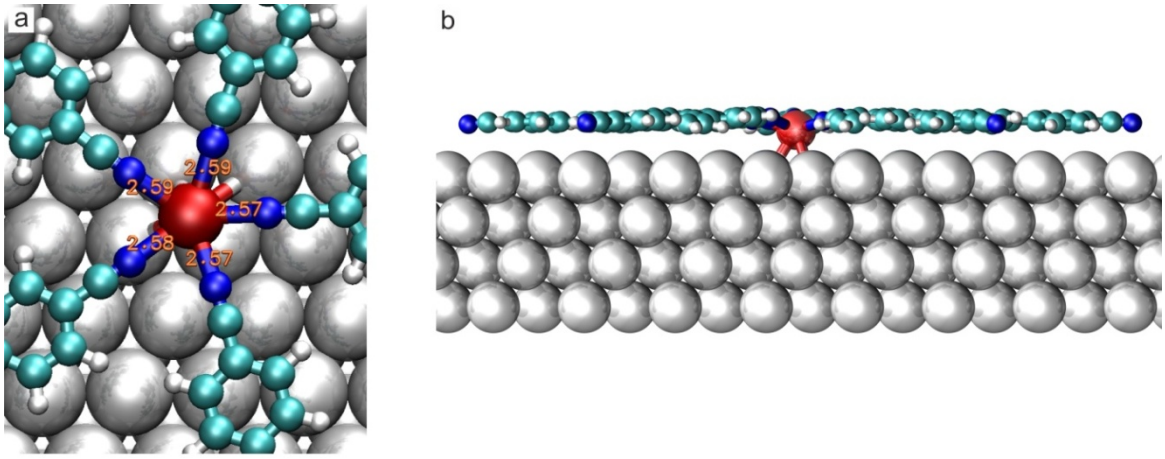

Figure 3 . 6 | Ball-and-stick model derived by density-functional theory simulations of a five-fold Ce coordination to *p*-NC-Ph_3-CN-*p* species adsorbed on Ag(111)

a, Top view of the bonding of the linker molecules to the Ce atom. The Ce-N distances are indicated in red. **b,** Perspective view of **(a)** revealing the planarity of the five organic linkers connected to the central Ce atom. Ce, nitrogen, carbon and hydrogen are depicted in red, violet, green and white colors, whereas silver substrate atoms are shown in grey.

3.2.2 Supramolecular dodecameric network (phase β)

For a Ce/Gd : linker ratio of ≈ 1 : 4, a new phase appears giving rise to extended domains and coexisting with isolated pentameric units (cf. Figure 3.4(a)). Equivalent assemblies could be produced by the combination of linker **1** and Ce, linker **2** and Ce (or Gd) on Ag(111). Herein, each individual Ln atom, imaged as a bright protrusion, is strictly surrounded by five molecules, imaged as rods, i.e. the planar five-fold coordination predominates again. This network is based on a two-level hierarchical design formed by dodecameric units, which forms a hexagonal network[106] (cf. Figure 3.7(b,c,e,f) and Table 2 for structural details). A dodecamer comprises three Ce/Gd centers and twelve linkers, arranged in a fashion in which three linkers are coordinated at both ends with lanthanide atoms, forming a triangle, and the nine remaining linkers are just singly coordinated to the Ce/Gd centers. The stability of the dodecamer is based on a five-fold Ce/Gd-linker coordination, whose projected lengths are shown in Table 2. The second level of hierarchy reveals the assembly of the dodecamers on the surface in a hexagonal fashion via CN···phenyl attractive interactions between adjacent dodecamers (cf. projected CN···H distances in Table 2). The surface registry of the linkers is manifested by a distinct angle of the hexagonal network with respect to the close-packed <1-10> directions of the silver surface, corresponding to 10° for Ce and linker **1**, and to 30° for the Ce or Gd and linker **2** cases, respectively. Importantly, Ce or Gd hierarchical dodecameric phases involving linker **2** are geometrically indistinguishable.

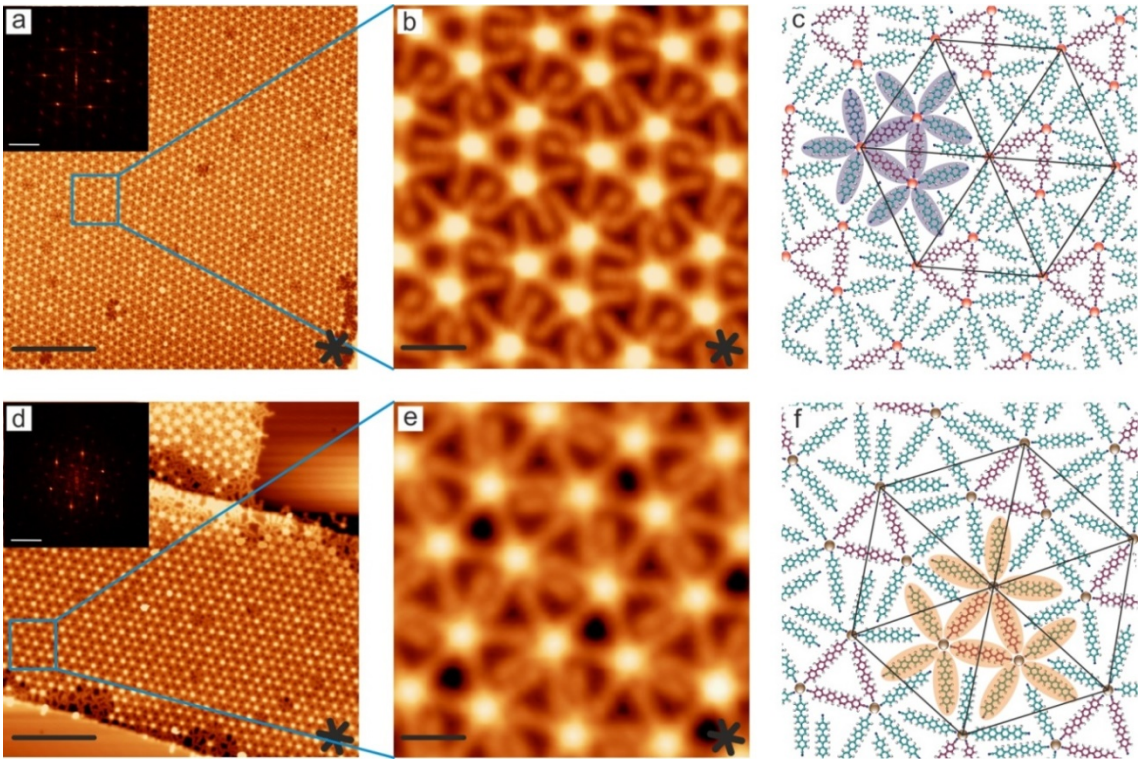

Figure 3 . 7 | Dodecameric network based on a 1 : 4 (lanthanide : molecular linker) stoichiometric ratio on Ag(111)

a, Large-scale topographic STM image of the hierarchical network employing Ce and linker **1.** (V_b = -0.2 V, I = 80 pA, scale bar = 20 nm). Fast Fourier transform is also depicted revealing the spatial periodicity of the tiling pattern (the white scale bar represents 0.045 $Å^{-1}$). **b,** Zoom-in of image **(a)** displaying the hierarchical network based on dodecameric units. (V_b = 0.6 V, I = 95 pA, scale bar = 2 nm). **c,** Atomistic model of **(b)** highlighting the dodecameric unit (violet lobes) and depicting the hexagonal network arrangement of the Ce centers described in the text. **d,** Large-scale topographic STM image of the hierarchical network obtained with Gd and linker **2** (V_b = 0.7 V, I = 50 pA, scale bar = 20 nm). Fast Fourier transform is also depicted revealing the spatial periodicity of the tiling pattern (the white scale bar represents 0.045 $Å^{-1}$). **e,** Zoom-in of image **(d)** (V_b = 0.3 V, I = 69 pA, scale bar = 2 nm). **f,** Atomistic model of **(e)** in which the orange lobes highlight the dodecameric unit. In **c** and **f** C atoms of the linkers involved in a single coordination with Ce/Gd are depicted in green, whereas those connecting two Ce/Gd atoms are represented in maroon. N, H, Ce, and Gd atoms are depicted in violet, white, red, and brown, respectively.

System	Unit cell vector [Å]	CN-Ln [Å]	<CN···H> [Å]
Ce and linker **1**	42 ± 2 Å, DFT: 43.0 Å	2.2 ± 0.5 Å, DFT: 2.6 Å	2.3-3.5 Å, DFT: 2.3-3.0Å
Ce and linker **2**	50 ± 3 Å	2.8± 0.5 Å	2.5-3.6 Å
Gd and linker **2**	50 ± 3 Å	2.6 ± 0.3 Å	2.3-3.6 Å

Table 2 | Structural distances of the hierarchical dodecameric assemblies produced by the deposition of Ce and linker 1, Ce and linker 2, and Gd and linker 2 on Ag(111). All experimental distances refer to projected lengths.

In addition, both dodecameric networks present two organizational domains entitled domain β_1 and domain β_2, related by a 180° rotation featuring supramolecular organizational chirality, which results in the formation of two sets of mirror symmetric domains (cf. Figure 3.8).

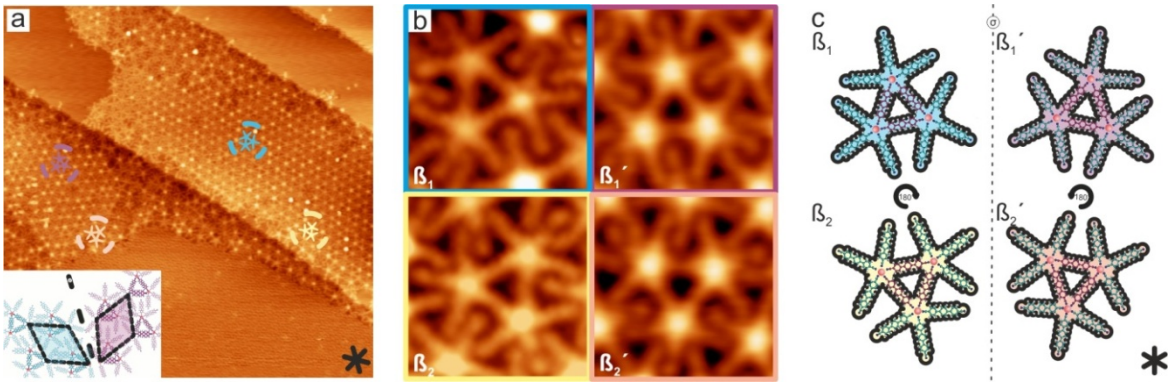

Figure 3 . 8 | Supramolecular organizational chirality

a, Large-scale STM image displaying the coexistence of the four organizational chiral domains achieved by mixing linker **1** and Ce on Ag(111) with a local stoichiometric ratio (Ce : molecule) of ≈ 1: 4 (V_b = -0.2 V, I = 80 pA and image size = 957 x 957 Å²). Black lines mark the Ag(111) high symmetry axes. **b,** High resolution STM images of the four organizational chiral domains. **c,** Atomistic models of the dodecamers shown in **(b)**. In order to facilitate the inspection of the mirror symmetry, the close-packed directions (shown in solid black lines) of the substrate are rotated to be aligned with the vertical.

As well as for the supramolecular pentameric unit described in section 3.2.1, a careful analysis of the internal structure of the dodecamers reveals a random variation of the opening angles between constituent linkers of the dodecameric units, thanks to the adaptiveness of the lanthanide coordination sphere. This variation is related to the CN···phenyl interaction of each supramolecule with its adjacent dodecamers, since the length of the linkers allow for two equivalent contacts between dodecameric supramolecules for any linker length, as depicted in Figure 3.9. This flexibility can be inspected by STM measurements, and, in addition, it can be induced by applying voltage pulses of 1.2 V (Ce-linker **2**) and of 1.5 V (Ce-linker **1**) on the metal centers with the STM tip. Figure 3.9 shows one transition in a Ce-linker **2** (a,b) and in a Ce-linker **1** (c,d) dodecameric contact, where a change in the opening angle of 11° and of 15° is observed.

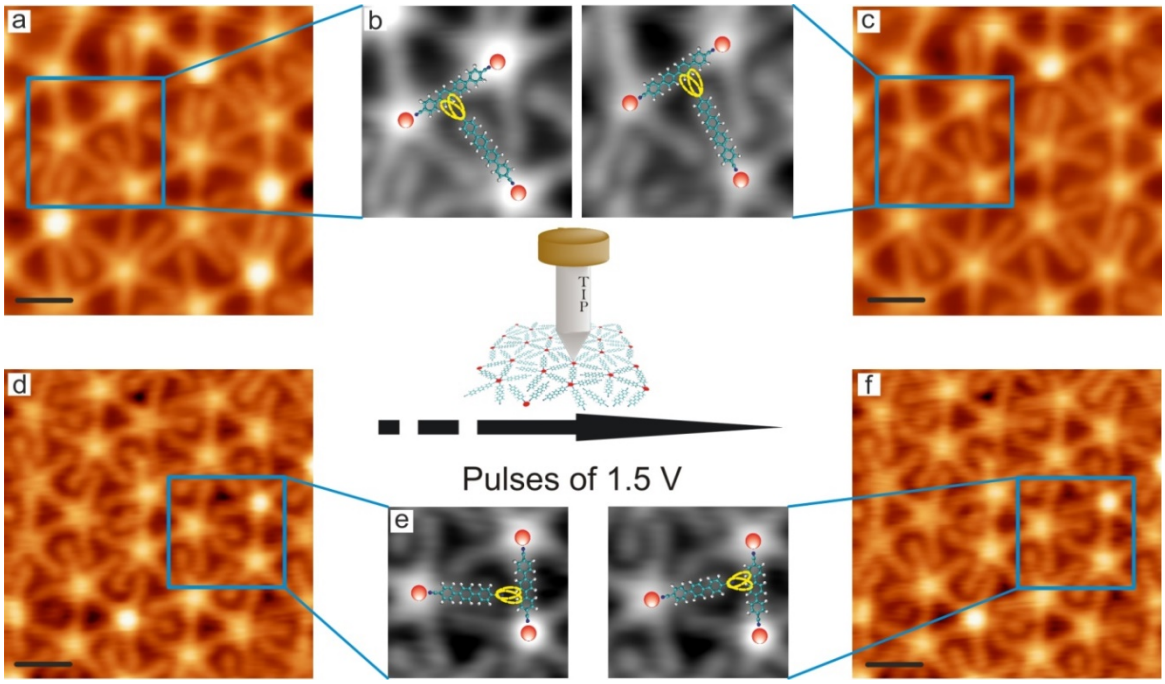

Figure 3 . 9 | Dodecameric phase flexibility as probed by voltage pulses with the STM tip

a-c, High-resolution STM images of the dodecameric phase created by Ce and linker **2** on Ag(111) (V_b = 0.2 V, I = 73 pA). **b,** Maximized insets of **(a, c)** show the change of the lateral coordination CN···H between dodecameric units by applying voltage pulses of 1.2 V on top of the Ce centers (4.8 × 4.8 Å²). **d, f** High-resolution STM images of the dodecameric phase produced by Ce and linker **1** on Ag(111) (V_b = -0.2V, I = 80 pA). **e,** Maximized insets of **(d, f)** show the change of the lateral coordination CN···H between dodecameric units by applying voltage pulses of 1.5 V on top of the Ce centers (3.7 × 3.7 Å²). **a, c, d, f** Scale bar: 2 nm.

Finally, we have simulated the hierarchic supramolecular architecture (phase β) created by *p*-NC-Ph_3-CN-*p* species and Ce adsorbed on Ag(111). Our results reveal that the structure around the Ce-linker bonds is only slightly different, with the largest effect being the average height of the Ce atoms above the substrate, now 2.75 Å, 0.11 Å higher than in phase α. The Ce-N bond lengths are similar, here 2.55 Å, and the C-N bonds again are little changed from the gas phase. The binding energies of the singly and doubly coordinated molecular species are 3.37 eV and 4.07 eV, respectively. The average height of the linker molecules from the substrate is 3.14 Å, only 0.03 Å closer than in phase α. The average dihedral angle is about 7°.

3.2.3 Supramolecular snub square Archimedean tessellation (phase γ)

Upon increasing the proportion of lanthanide, domains of a fully reticulated 2D metal-organic network evolve (cf. Figure 3.10). For stoichiometric ratios equal to 2 : 5 these architectures present all linkers with both terminal carbonitriles coordinated to a Ce/Gd atom, being only stabilized by five-fold Ce/Gd-carbonitrile bonds.

Thus, employing linker **1** and Ce (cf. Figure 3.10(b,c)), linker **2** and Ce (cf. Figure 3.10(a,d)) and linker **2** and Gd (cf. Figure 3.10(e)) the reticulated network is formed. Analogous to the dodecameric phase, networks produced using linker **2** and Ce or Gd are structurally indistinguishable. Notably, as in other phases a minority of the lanthanide nodes (less than 15%) present a different appearance, which is attributed to axial ligation by residual gas contamination, since they could be modified by applying voltage pulses with the tunneling tip. It is also observed that the Ce/Gd nodes are five-fold vertexes connected to adjacent nodes by the molecular linkers, following a design scheme that can be understood as a surface tessellation based on triangles and squares where each node is sharing three triangles and two squares according to a 3.3.4.3.4 pattern, i.e. a snub square Archimedean tessellation. Thus, the reticulated network is stabilized by a flexible five-fold Ce/Gd-NC coordination (cf. atomistic model for linker **2** in Figure 3.10(f)), presenting opening angles between adjacent linkers of 60° or 90° (strongly deviating from the 72° expected for a regular pentameric coordination), and exhibiting Ce/Gd-NC bond lengths of 2.4 ± 0.5 Å for linker **1** and Ce, of 2.7 ± 0.5 Å for linker **2** and Ce, and of 2.6 ± 0.3 Å for linker **2** and Gd architectures. In addition, is important to noticed that when the molecular stoichiometric ratio is increased to concentrations higher than 2 : 5 (Ce/Gd : linker) organic molecules appear trapped inside the squared network pores and no variation in the number of organic molecules linked to lanthanide nodes is observed.

The thermal stability of the snub square Archimedean tessellation is also investigated. A detailed inspection close to room temperature of the surface enhanced by linker **1** and Ce in the network stoichiometry shows the coexistence of a 2D "sea" of mobile adsorbates (evidenced by streaking and the higher apparent height of the area outside the empty molecular pores circled) with some snub square Archimedean tessellation motifs (cf. Figure 3.10(c)). This hints to the potential of the lanthanide coordination on

surfaces to create room-temperature stable architectures, provided a proper engineering of the linking functional groups.

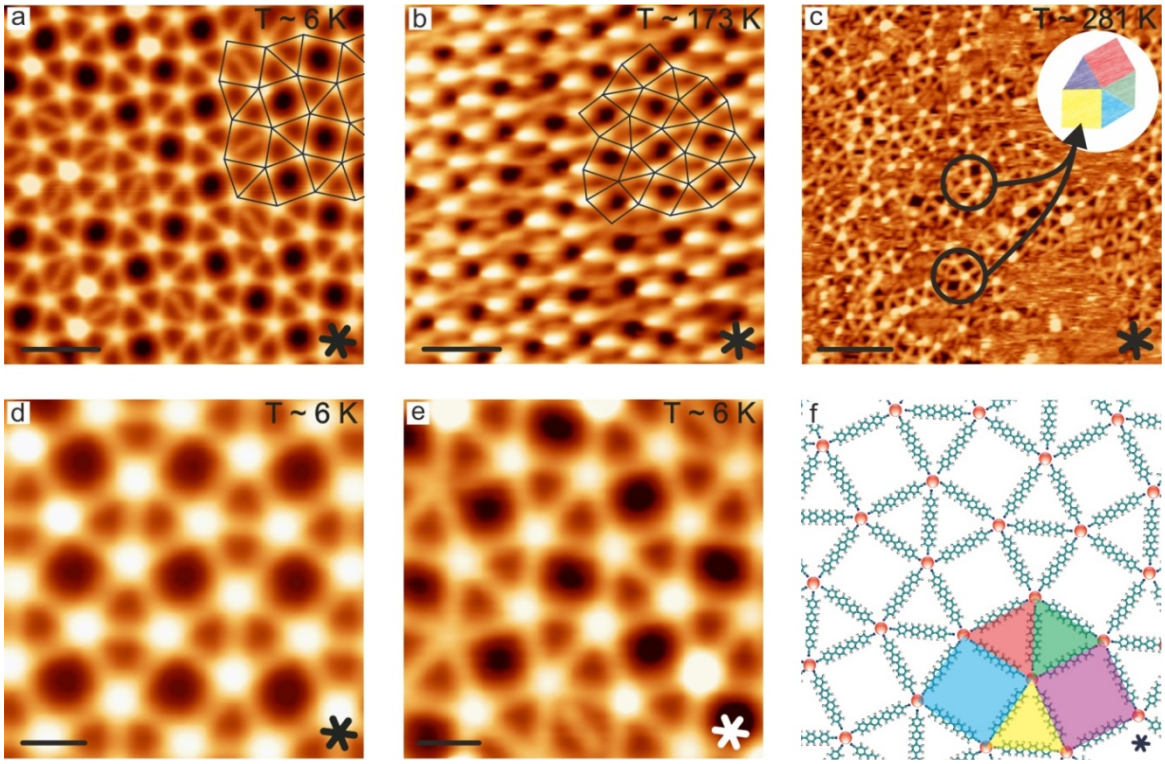

Figure 3 . 10 | Supramolecular snub square Archimedean tessellation on Ag(111) based on a 2 : 5 (lanthanide : molecular linker) stoichiometry

a, Large-scale topographic LT-STM image of the snub square Archimedean tessellation employing Ce and linker **2** (V_b = 2.4 V, I = 100 pA, T_{STM} = 6 K). **b,** Large-scale STM image of the snub square Archimedean tiling obtained by using Ce and linker **1** (V_b = 2.4 V, I = 100 pA, T_{STM} = 173 K). **a-b,** Scale bar: 5 nm. **c,** STM image of the coexistence at 281 K of snub square Archimedean tiling motifs, produced by the coordination of Ce and linker **1**, with diffusing species. (V_b = 2.3 V, I = 100 pA, scale bar: 10 nm). **d,** High resolution STM image of the snub square Archimedean tiling obtained by the self-assembly of Ce and linker **2** (V_b = 0.2 V, I = 100 pA). **e,** High resolution STM image of the snub square Archimedean tessellation phase achieved by the coordination between Gd and linker **2** (V_b = 0.3 V, I = 69 pA). **d-e,** Scale bar: 2 nm. **f,** Atomistic model of **(d)** superposed with 3.3.4.3.4 sequence tiling motif. The different tile color represents the different orientation. Red circles are assigned to single Ce centers and linkers are depicted in green. The unit cell of the network is defined by two squares and three triangles on each vertex. **a-f,** Black or white stars represent the close-packed directions of Ag(111).

A further analysis displays three different organizational domains, interrelated by a rotation of 60° extended over a maximum area of 300 Å x 300 Å, where six different

molecular orientations with respect to the three-fold substrate are observed as shown in Figure 3.11.

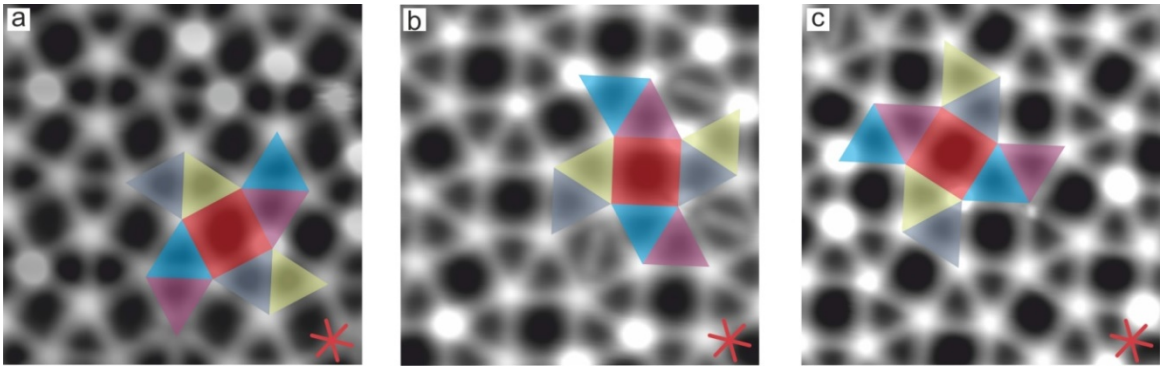

Figure 3 . 11 | Organizational domains of the snub square tessellation of Ag(111)

a-c, STM images of the three supramolecular orientational domains of the snub square tessellation, obtained by depositing Ce and linker **2** at a local Ce : molecule stoichiometry of ≈ 2 : 5 (Vb = 0.2 V, I = 80 pA, 136 × 136 Å²).

One of the most significant characteristics in the lanthanide-organic coordination is the flexibility that Ce/Gd presents when they interact with the molecular linkers. As result of this property, another pattern, also based in one of the semi-regular Archimedean tilings correspond to five-vertex configurations is sporadically detected. Herein, three triangles and two squares are joined in five-fold vertexes and arranged according to a 3.3.3.4.4 scheme (cf. Figure 3.12), which is identified as an elongated triangular Archimedean tiling motif. Only the snub hexagonal tiling, one of the three semi-regular Archimedean tessellations based on five-fold nodes with 3.3.3.3.6 motifs (Figure 3.12(e)) was not achieved due to the coherent limitations in the adaptability of the lanthanide coordination sphere.

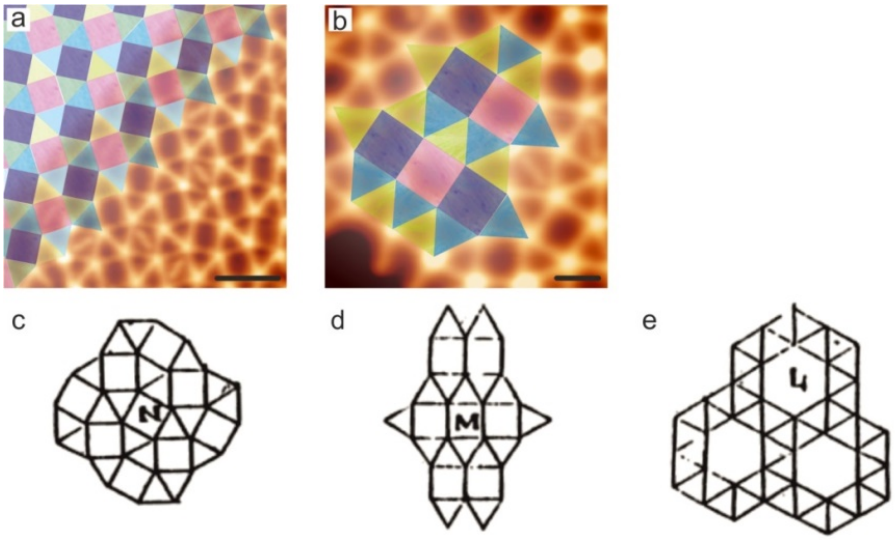

Figure 3 . 12 | Supramolecular Archimedean tiling motifs on Ag(111)

a, STM image of the snub square Archimedean tessellation (V_b = 0.2 V, I = 70 pA). Scale bar: 5nm. **b,** STM image of elongated triangle tiling motifs (V_b = 0.2 V, I = 50 pA). Scale bar: 2 nm. **c-e,** Five-vertex Archimedean tilings of the plane as sketched by Johannes Kepler in "Harmonices Mundi"[107].

3.3 Controlled manipulation of gadolinium coordinated supramolecules

The atomistic capabilities of scanning tunneling microscopes were decisive to lay the foundation of nanoscale science and technology. They have fascinated scientists over the last decades, and accordingly, low-temperature STMs have been used as an analytical or engineering tool in the manipulation of single atoms/molecules on surfaces[10,108-117] (Figure 3.13), designing artificial architectures and inspecting their electronic, magnetic, catalytic and mechanical properties with extraordinary spatial resolution.

Generally, manipulation techniques on metal surfaces include the use of direct tip-adsorbate forces (lateral or vertical manipulation), electric fields or inelastic tunneling electrons[59,118-120]. The "lateral manipulation" procedure (LM) is normally used to relocate single atoms/molecules with extraordinary control over the tip-atom/molecule-surface interaction. Taking advantage of the lack of thermal motion at low-temperature, scanning tunneling microscopes (STMs) have been used in the last decade to trigger conformational changes[121-124], tautomerization and switching[110,114,125-129], chemical

reactions[117,129-135], or desorption of adsorbates[136], and recently to induce the walking of a molecular nanocar across a surface[124]. Nevertheless, the systematic lateral manipulation and tuning of supramolecular systems stabilized by coordination interactions is still not addressed.

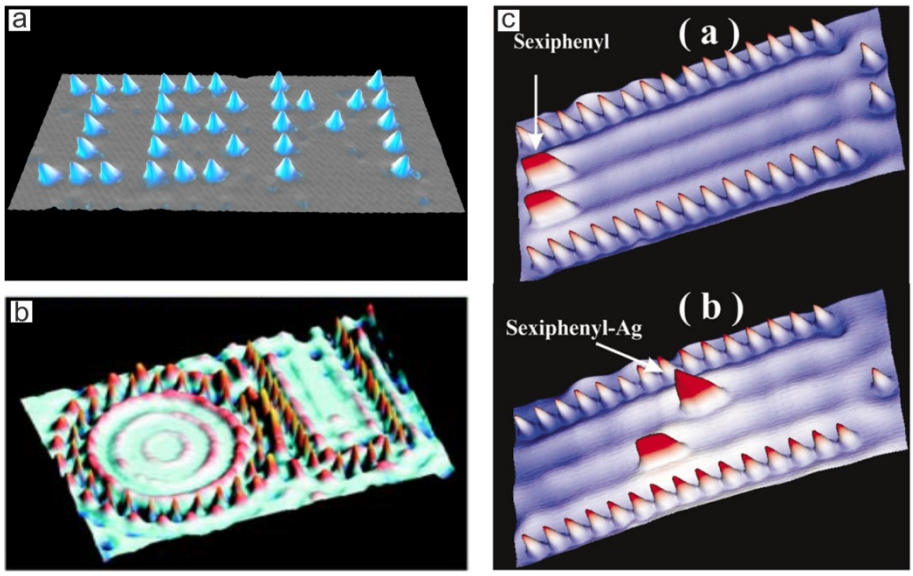

Figure 3 . 13 | Atom/molecule manipulation by means of scanning tunneling microscopy

a, IBM logo constructed with 35 Xe atoms on a Ni(110) surface by Don Eigler in 1989[137]. **b,** OU logo[59] writing using individual silver atoms on a Ag(111) surface at 6 K. **c,** Molecular shooting of two sexiphenyl species (left) and two target atoms (right) positioned along the standing wave track. A silver-sexiphenyl complex is formed by shooting the upper sexiphenyl[59].

In this section we study the potential of the low-temperature scanning tunneling microscope to manipulate and tailor supramolecules formed by coordination interactions of Gd nodes and *p*-NC-$(Ph)_4$-CN-*p*[42] ENREF 138. By positioning the STM tip above the lanthanide node and adjusting the tip-metal distance to get into an attractive regime, pentameric units are laterally moved across a Ag(111) surface with high fidelity. Furthermore, the LM procedure is employed to in-situ create and displace different supramolecular units, including tetramers, pentamers, nonamers and dodecamers, which highlights its potential to purposely engineer supramolecular systems stabilized by coordination bonds with meticulous control.

Pentameric units formed by the gadolinium-directed assembly with *p*-NC-$(Ph)_4$-CN-*p* species on Ag(111) are exhibited in Figure 3.14. Under specific stoichiometric conditions (local ratio Gd : molecule of ≈ 1 : 5) the pentamers comprise five rod-like shaped molecular species linked to a Gd node that appears as a bright protrusion, as described in section 3.2.1. In addition, the Ag(111) substrate plays a crucial role in the alignment of the pentameric units where two or three of the molecular linkers, constituting the supramolecule, are positioned following the close-packed directions of Ag(111).

In order to demonstrate the supramolecular robustness and mobility of the pentameric units, they are laterally manipulated following a three step protocol: 1) Vertical approach of the STM tip towards the gadolinium node of the pentamer to increase the tip-supramolecule interaction; 2) Movement of the tip along the surface to the desired final location displacing the pentamer; and 3) Retraction of the STM tip back to the normal image-height conditions. Remarkably, the tip-gadolinium distance should be delicately chosen to establish a weak chemical bond between tip and metal in order to translate the supramolecule. In the LM process, the tunneling resistance R_t points out the tip-atom separation and their interaction strength. Thus, for large/small tunneling resistances far/close tip-atom distances are achieved.

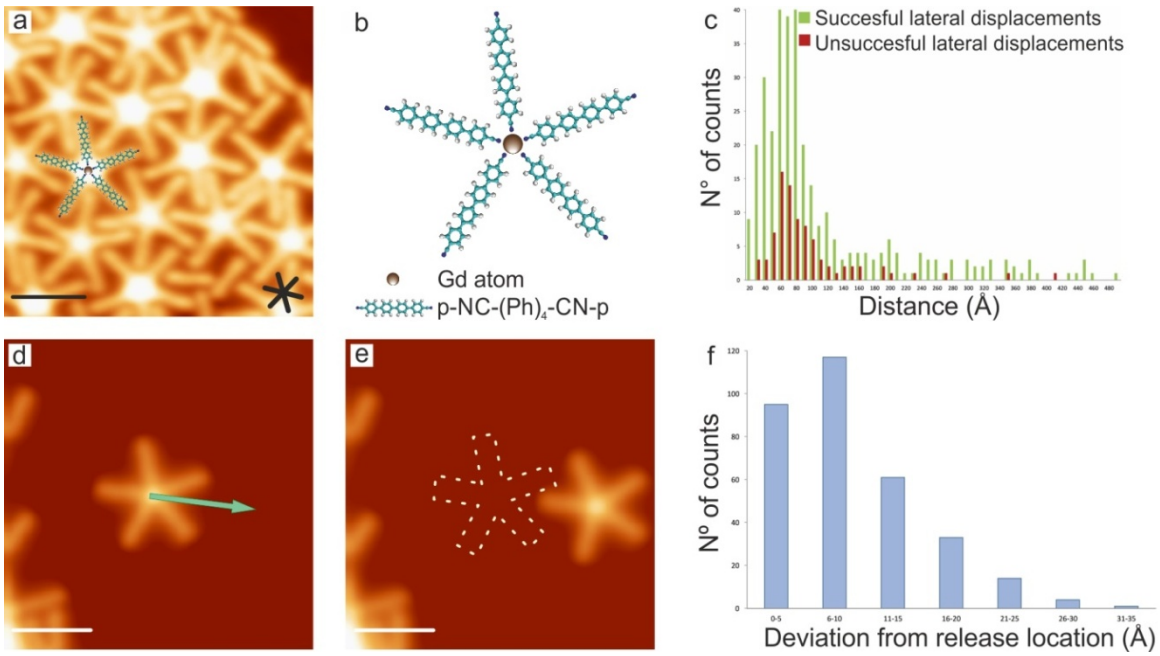

Figure 3 . 14 | Lateral manipulation of a five-fold Gd-carbonitrile coordinated supramolecule (pentamer) by a STM tip on Ag(111)

a, High resolution STM image of pentameric supramolecules coexisting with some non-coordinated molecular linkers, obtained by the deposition of *p*-NC-$(Ph)_4$-CN-*p* species and Gd on Ag(111). **b,** Atomistic model of a pentameric unit showed in **(a)** formed by five molecular linkers and a Gd atom. **c,** Histogram of the lateral manipulation events vs. travelled distance. Unsuccessful lateral displacements account for those experiments were the supramolecule was detached or not translated. Lateral translations are shown in green while no displacement events are displayed in red. **d-e,** High resolution STM images illustrating the lateral manipulation in constant current mode (R_t = 2 MΩ) of a pentameric unit. The green arrow sketched in **(d)** reveals the path followed by the tip during the lateral manipulation, while the white dashed silhouette in **(e)** reveals the position of the pentamer before the movement of the supramolecule. **a, d, e,** Scanning parameters: V_b = 0.3 V, I = 60 pA. Scale bar: 3 nm. **f,** Histogram of the deviation of the center of the supramolecular entity from the expected position after a lateral manipulation.

In our experiments tunneling resistances (R_t) between 0.3 and 10 MΩ are used for the displacement of the pentamers, whereas experiments performed at closer distances (R_t < 0.3 MΩ) resulted in the desorption of the pentamer, and at higher distances (R_t > 20 MΩ) the supramolecules cannot be displaced. Additionally it is important to notice that the supramolecular units can be equally displaced on the surface without following any special substrate direction, i.e. Ag(111) high symmetry directions.

More in detail a numerous series of experiments were carried out covering distances from 10 to 500 Å in a single process (cf. Figure 3.14(e)), whereby approximately 80% of supramolecules was successfully translated (> 400 experiments). The histogram of displacement accuracy (cf. Figure 3.14(f)) reveals that in most of the experiments the center of the supramolecule is slightly displaced from the final desired location (average value of ≈ 9 Å), regardless of the distance travelled.

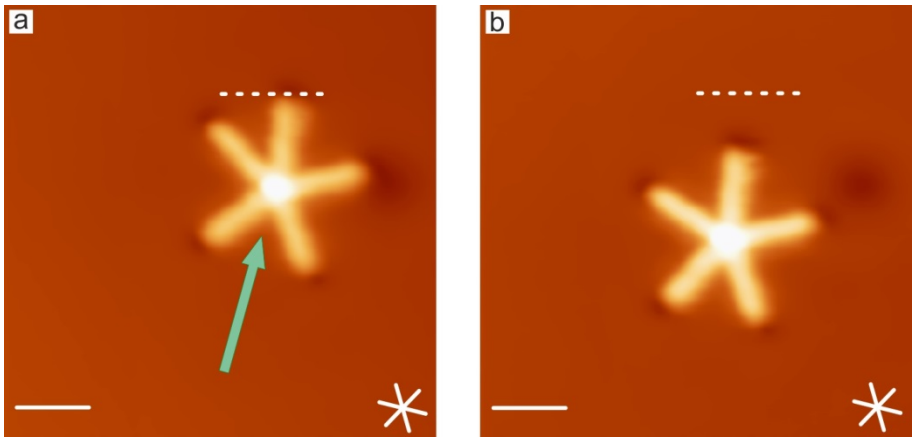

Figure 3 . 15 | Attraction of a pentameric supramolecule by the STM tip

a, High resolution STM image of a pentameric supramolecule. The green arrow indicates the length and direction of the constant current lateral manipulation process. **b,** High resolution STM image that reflects the lateral displacement of the pentameric supramolecule showing the attractive nature of the tip-supramolecule interaction. The white dashed lines are a guide for the eyes. **a-b,** Scanning parameters: V_b = 0.3 V, I = 90 pA. Tunneling resistance during lateral manipulation, R_t = 10 MΩ. Scale bar = 2 nm.

The nature of the lateral manipulation mechanism has also been investigated. The forces involved in the LM process and the mechanism of atom/molecule movement can be resolved by the tunneling current signals. They have been previously reported by other authors[59] concluding that three LM modes are plausible: "pushing", "pulling" and "sliding". In the pushing mode the repulsion presented in the tip-atom/molecule interaction forces the atom/molecule to move in front of the tip while in the pulling and sliding modes the atom/molecule follows the STM tip due to an attractive tip-atom/molecule interaction. By positioning the STM tip at a lateral distance of 5 Å with respect to the gadolinium node of a pentameric unit, an attractive displacement of the supramolecule towards the tip is observed (Figure 3.15), tough the specific mode could not be achieved.

In order to examine the capabilities of our approach for tailoring advanced supramolecular architectures, the lateral manipulation protocol is used in the design of a pentagon with five pentameric units (cf. Figure 3.16(a-c)), and the letter-sequence "TUM" (acronym of the Technical University of Munich) with 14 supramolecules (cf. Figure 3.16(d)). For this purpose, individual pentamers are extracted from supramolecular islands composed of pentameric units (cf. Figure 3.16(a)). Due to the interactions between supramolecules, the minimum separation between adjacent pentameric entities providing structural stability of the resulting design was found to be 35 Å for supramolecules presenting different orientations.

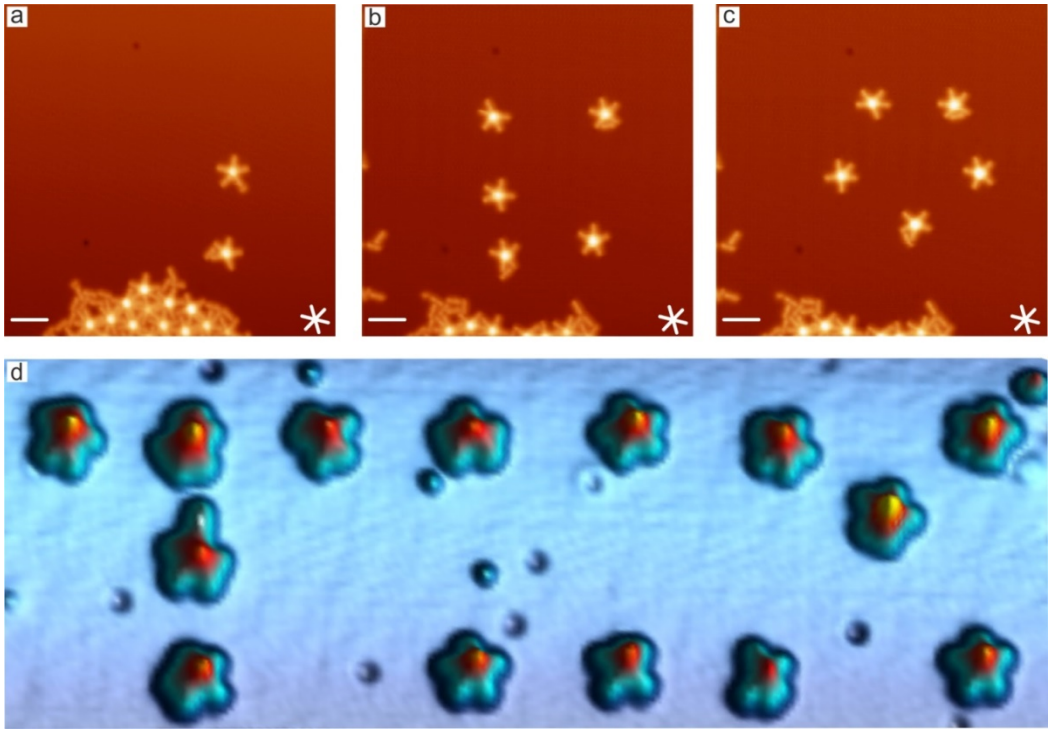

Figure 3 . 16 | Design of advanced molecular architectures by lateral manipulation of pentameric supramolecules with a STM tip

a-c, High resolution STM images of the formation of a pentagon by pulling five pentamers. **d,** High resolution STM image of the design of the TUM (Technische Universität München) logo by lateral manipulation of 14 pentameric entities. **a-d,** During the lateral manipulation the tunneling resistance (Rt) was set in the range of 0.3-0.6 MΩ. Scanning parameters: **a-c,** V_b = 0.7 V, I = 50 pA. Scale bar = 3 nm. **d,** V_b = 0.7 V, I = 80 pA.

Inner transition metal´s coordination chemistry allows geometrical possibilities that cannot be reached by the rigid polyhedra formed in d-block elements[138]. In a 2D environment and taking advance of the capabilities of scanning tunneling microscopy for in-situ synthesis, _ENREF_36 _ENREF_43 _ENREF_19 _ENREF_37 we have employed the STM tungsten tip to detach single organic molecular linkers from the pentamer complexes, creating 4-fold coordinated supramolecules. Figure 3.17(a-b) illustrates the transformation of a pentameric complex into a tetramer, by pulling out one linker species from the supramolecule, resulting in the desorption of the missing molecule. These tetramers can be displaced across the surface under similar manipulation conditions as the pentamers (cf. Figure 3.17(b-d)) and they could be transformed back into pentamers (cf. Figure 3.17(e-h)), by displacing a *p*-NC-$(Ph)_4$-CN-*p* molecule into the Gd sphere, and subsequently lateral manipulated as before, which highlights the

potential of the in-situ chemistry of the lanthanide elements. The addition of further organic linkers to the Gd sphere was not possible, probably due to steric limitations of the coordination environment.

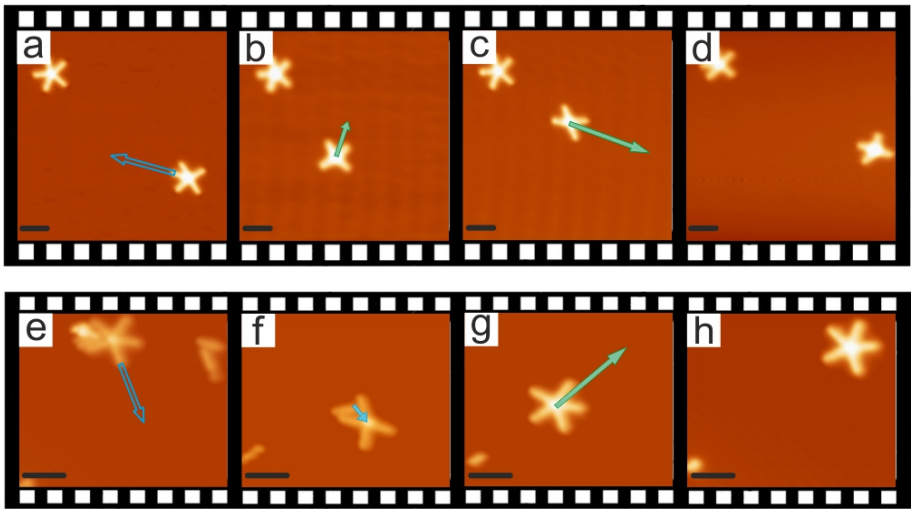

Figure 3 . 17 | In-situ tailoring and displacement of Gd-carbonitrile metal-organic supramolecules

a-c, Detachment of one *p*-NC-$(Ph)_4$-CN-*p* species from a pentameric supramolecule by the lateral manipulation of one constituting linker (R_t = 0.4 MΩ), which gives rise to the formation and displacement of a four-fold Gd-carbonitrile coordinated supramolecule. **b-d,** Tunneling resistance during lateral manipulation of the tetrameric species, Rt = 0.4 MΩ. **a-d,** Scanning parameters: V_b = 0.7 V, I = 58 pA. **e-f,** Removal of one *p*-NC-$(Ph)_4$-CN-*p* molecule from a pentameric supramolecule by applying the lateral manipulation procedure describe in the text (R_t = 6 MΩ), which results in the creation and displacement of a four-fold Gd-coordinated supramolecule. **f-g,** A *p*-NC-$(Ph)_4$-CN-*p* linker is fused to the four-fold species recovering the pentameric supramolecule. **g-h,**Lateral manipulation of the pentamer (R_t = 6 MΩ). **e-h,** Scanning parameters: V_b = 0.9 V, I = 65 pA. Blue arrows indicate the path of the STM tip during a lateral manipulation process giving rise to the formation of a tetramer **(a, e)** or a pentamer **(f)**, whereas green arrows displays the path of the tip during an ordinary lateral manipulation procedure keeping the coordination number of the Gd sphere (**b-d, g-h)** . **a-h,** Scale bar = 3 nm.

In order to analyze the adaptability and the robustness of the Gd coordination sphere, nonameric and dodecameric supramolecules were designed by lateral manipulation procedures (as previously described in Figure 3.16). Figure 3.18(a,b) depicts the formation of a nonameric species (consisting of nine linkers and two Gd nodes), by merging one pentamer into another, involving the release of a *p*-NC-$(Ph)_4$-CN-*p* molecule and the creation of the supramolecular nonamer. Furthermore, Figure 3.18(e-n) shows the in-situ formation of a dodecamer complex, obtained thanks to the same lateral

manipulation protocol used in Figure 3.18(a,b) which consists in the crash of one pentamer into a nonamer, producing a triskaidecameric supramolecule (composed of thirteen linkers and three Gd nodes). Subsequent displacement across the surface induces conformational changes that lead to the formation of a dodecameric supramolecule after the detachment of one *p*-NC-$(Ph)_4$-CN-*p* species.

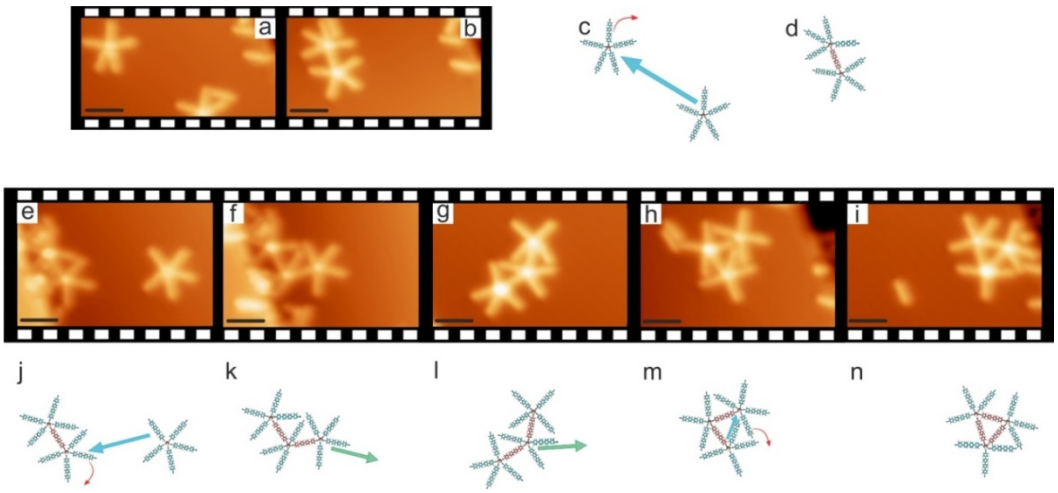

Figure 3 . 18 | In-situ synthesis of nonameric and dodecameric species by the lateral manipulation of self-assembled Gd-carbonitrile coordinated supramolecules

High-resolution STM images **(a-b)** and schemes **(c-d)** of the formation of a nonameric supramolecule by the lateral manipulation and crash of one pentameric species into another pentamer. **a-b,** Scanning parameters: V_b = 0.85 V, I = 60 pA. Tunneling resistance during lateral manipulation, R_t= 1.1 MΩ. High-resolution STM images **(e-i)** and schemes **(j-n)** of the design of a dodecameric supramolecule by the lateral manipulation (R_t = 6 MΩ) of a pentamer into a nonameric species giving rise to a triskaidecameric species **(e,f,j,k)** which is displaced across the surface to release a *p*-NC-$(Ph)_4$-CN-*p* unit, resulting in a dodecamer **(e-g, k-n)**. **e-i,** Scanning parameters: V_b = 0.9 V, I = 65 pA. Tunneling resistance during lateral manipulation, R_t= 6 MΩ. Green and blue arrows display the path followed by the tip during the lateral manipulation resulting in the synthesis of novel species (blue) and the displacement of the supramolecular entities (green), respectively. The curve red arrow illustrates the detachment of a *p*-NC-$(Ph)_4$-CN-*p* species. Molecular linkers singly coordinated to Gd are depicted in green, whereas those double coordinated are represented in maroon. Scale bar: 3 nm.

3.4 Conclusion

In summary we have presented the rich versatility of five-fold coordination chemistry on surfaces, based on lanthanide-carbonitrile interactions, to produce 2D advanced architectures with intricate designs, including disordered patterns, hierarchical short-range orientational disordered crystalline networks, and snub square Archimedean tessellations coexisting with elongated triangular Archimedean tiling motifs. The potential of these supramolecular designs in different fields can be significant, including heterogeneous catalysis via the axial activity of the lanthanides (all phases), molecular recognition by structural adaptation, and novel photonic crystals[100] or frustrated magnets[99] predicted for the snub square Archimedean tessellations.

In addition, we have introduced novel protocols to manipulate and design molecular nanoarchitectures on surfaces, by exploiting the potential of lanthanide coordination chemistry to create gadolinium-carbonitrile coordinated supramolecules, and the versatility of scanning tunneling microscopy to deliberately displace them. In particular, pentamers built up by the five-fold coordination of quaterphenyl-4,4''-dicarbonitrile species and Gd atoms, were lateral positioned in a constant current mode dominated by attractive tip-supramolecule interactions. Furthermore, the lanthanide coordination sphere of the pentameric nodes was tailored and molecular bridges between different Gd-centers were established by the STM tip. The afforded multi-center metallosupramolecular arrangements, together with the lateral manipulation capabilities, provide versatile prospects for the in-situ design of advanced surface-confined molecular architectures incorporating the functionalities of the lanthanides elements, thus presenting novel opportunities in different areas such as organic electronics, nanomagnetism and catalysis.

Thus, based on the versatility of surface-confined coordination chemistry concepts, we expect that our approach is of general relevance for other molecular linkers and f-block metal centers. By developing assembly protocols on surfaces that make use of the high coordination numbers provided with the family of the lanthanides, complex metal-organic nanoarchitectures and networks with unique metal-organic bonding motifs and surface tessellations can be engineered and manipulated. Following this protocol and as

an illustration of its scope, in the next chapter we employ europium atoms, instead of cerium or gadolinium used in this chapter, in order to inspect possible differences in the metallosupramolecular networks structure. Furthermore, we also inspect the importance of the adlayer/substrate interactions comparing the results obtained on the Au(111) and Ag(111) surfaces.

4. Manifold lanthanide (Eu)-carbonitrile coordination on surfaces: A route to quasicrystallinity

Traditionally the atomic structure of solids has been separated in two groups: crystalline and glassy structures. On one hand, crystalline structures, which are extremely ordered, follow strict rules: i) they present long-range translational order distinguished by a regular spacing of unit cells; ii) they show long-range orientation order with symmetry axes (two-, three-, four-, and six-fold) compatible with periodicity, i.e. the five two-dimensional and the fourteen three-dimensional Bravais lattices that determine many of their physical properties; iii) they exhibit rotational symmetry also related to the Bravais lattices. Nevertheless, unit cells based on five-, seven- and all higherfold symmetries are forbidden according to the traditional definition of crystal structures. On the other hand, glassy structures have no long-range correlations as the ones observed for crystals.

It was 1984 when Don Levine and Dan Shechtman identified for the first time a rapidly quenched Al_6Mn alloy that diffracted electrons like a crystal but with the peculiarity of having a decagonal strictly forbidden symmetry[139] _ENREF_139_ENREF_134. They termed this new discovery as "Quasicrystal" (QC) and since then, this peculiar ordered atomic structure has revolutionized our established knowledge in material science. In the last decades, quasicrystallinity has been the focus of intensive research[139-143], steered by its fundamental relevance in mathematics, physics, chemistry and materials science, and stimulated by its potential applications in advanced coatings, reinforced composites, optics, photovoltaics and magnetism[144-146]. Initial observations involved metallic alloys[140], but recently further materials were associated with quasicrystals, such as three-dimensional (3D) dendritic liquids micelles[147], ABC star polymers[148], mesoporous silica[149], natural quasicrystals[150-152] and two-dimensional (2D) surface-confined assemblies of binary nanoparticles[153] or hydrogen-bonded molecules[154]. These novel

quasicrystalline systems are characterized by long-range orientational order, and exhibit 10-fold[154], 12-fold[147-149,153] or even 18-fold[155] _ENREF_155 diffraction symmetry.

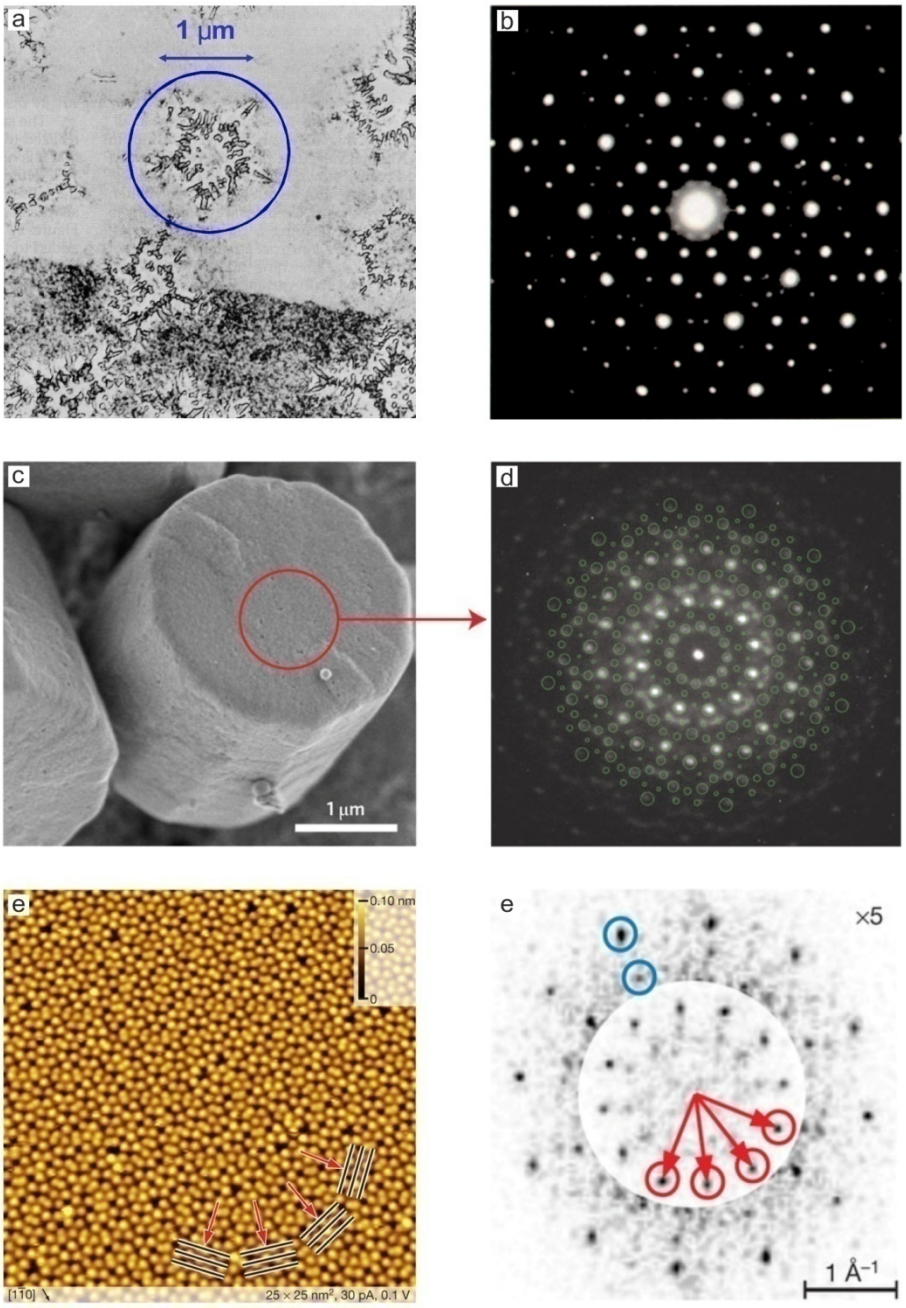

Figure 4 . 1 | Quasicrystalline structures found in different fields of study

a, Al_6Mn alloy. First QC structure discovered by Dan Shechtman in 1984. **b,** Electron diffraction pattern showing a symmetry strictly forbidden for crystals. Adapted from reference[139] _ENREF_156. **c-d,** Mesoporous silica material showing micrometer-scale grains with the morphology of a dodecagonal prism. In **(d)** an electron diffraction pattern of **(c)** shows well-ordered quasicrystalline behavior. Adapted from reference[149]. **e-f,** Low-temperature STM image of the dodecagonal $BaTiO_3$-derived thin film phase on

Pt(111) **(e)**, and its Fourier transform **(f)**. The Bragg planes of four first-order diffraction spots (arrows in **e**) are indicated in **f**. Adapted from reference[156].

Specifically, a random-tiling model is formed by dodecagonal quasicrystals (ddQC), which have appeared first in alloy particles[157,158] and tantalum-telluride clusters[159]. However, subsequent work revealed its universal character; indeed 12-fold symmetry prevails in soft-matter and other recently identified non-metallic QC[158,160,161] _ENREF_158. It has also been recognized that it is closely related to Frank-Kasper phases (close-packed phases known for their complex crystallographic structure and physical properties),[147,149,157,162-166] whereby notably the sigma-phase represents a so-called crystal approximant to ddQC, meaning that the arrangement of its unit cell constituents resembles local structures expressed in the QC state[167] _ENREF_167.

There are several routes towards a theoretical foundation of ddQCs[140-142,161,164,168-172]. They can be rigorously derived from mathematical considerations, e.g., by projections from regular higher-space lattices, which construction implies the presence of certain self-similarity and hierarchic order elements in the corresponding real-space manifestations[170-175] _ENREF_171. This class of QCs is designated 'deterministic'. A widely employed alternative approach towards ddQCs, that was invoked beforehand for the modeling of 2D amorphous systems[176] _ENREF_177, employs nonperiodic tessellations of the Euclidean plane comprising randomly distributed equilateral triangles and squares. Such stochastic square-triangle tilings produce a 12-fold diffraction pattern due to necessarily inherent dodecagonal symmetry elements[177-179].

Deterministic ddQCs are likely to be energetically stabilized (which means that they are thermodynamically stable at arbitrarily low temperatures), in contrast to the entropically-driven formation of random-tiling configurations[148,155,158,163,177,180]. Thus it is not surprising that a random-tiling phase with ddQC signature could also be identified in molecular dynamics (MD) modeling of a monatomic liquid during a cooling treatment[181] _ENREF_183. The underlying interaction was approximated by tailored pair potentials, similarly applicable for other condensed matter QC systems,[155,161,163,182,183] that were recently advanced to a level such that an entire series of QC mosaic structures could be described in a unified scheme[184]. These achievements not only help to disentangle the intriguing physics and chemistry of QC evolution and establish

commonalities among different classes of materials[142], but they also could provide important assets for conceiving novel functional materials[161,185].

Although clearly successful from multiple points of view, the experimental exploration of ddQC species can be a tiresome task, and most, if not all reported investigations suffer from the limited size of quasicrystalline regions, the frequently inherent structural inhomogeneities[158]. Beyond the notorious presence of defects, the very identification of which can pose a challenge by itself, subtle variations in the preparation conditions or the constituents' stochiometry may shift the balance from QC order to amorphous or approximant lattices, all of which may coexist in a given specimen. Also the distinction of metastable vs. ground state configurations can be problematic. Nevertheless, a sizable number of ddQC systems could be clearly identified,[147-149,153,157-159] and following direct visualization by transmission electron microscopy (TEM) and careful data analysis, several ones could be conclusively interpreted as random-tiling representations[148,149,153]. Moreover, a recent combined low-energy electron diffration and scanning tunneling microscopy (STM) study revealed the expression of an epitaxial thin-film ddQC layer on a homogenous Pt(111) surface with clear indications of ddQC order in extended domains, nicely expressing self-similarity features in agreement with deterministic ddQC patterning[156].

Under the framework of 2D surface-confined metal-organic coordination networks (MOCNs), the combination of europium (Eu) metal nodes with ditopic linear molecular linkers on smooth Ag(111) and Au(111) substrates is explored. Molecular-level scanning tunneling microscopy (STM) observations reveal that for specific stoichiometry the prevailing expression of three-, four-, five- and six-fold coordination nodes when the Au(111) is used and four- or five-fold coordination nodes for experiments realized onto the Ag(111) surface is observed. The designed networks exhibit distinct coordination motifs reflecting the importance of the molecule-substrate and molecule-lanthanide interactions and the coordination sphere adaptability observed for Eu atoms, in contrast with experiments realized in chapter 3 where five-fold Ce/Gd coordination nodes were prevalent. This behavior is tentatively explained by the physical and chemical properties of lanthanide elements which are determined by the nature of the ion-to-ligand chemical bonds and by the geometrical arrangement of the ligands around the metal

atom. In this sense, ligand-field effects in f-internal transition metal complexes are much smaller than the pertinent effects for d-transition metal complexes due to the shielding of the 4f orbitals by filled sub-shells of higher principal quantum number.

VT-STM experiments realized in this chapter were carried out at HKUST (Hong Kong University of Science and Technology) under the supervision of Prof. Dr. Nian Lin.

4.1 *p*-NC-(Ph)$_4$-CN-*p* + Eu on Ag(111)

In order to explore the chemical similarities and/or differences between two-dimensional lanthanide-organic architectures (Chapter 3), Eu atoms and *p*-NC-(Ph)$_4$-CN-*p* linkers are co-deposited onto a bare Ag(111) substrate and examined at room temperature (RT). Figure 4.2 describes the formation of long-range ordered square planar networks. Herein, molecular species are imaged as rod-like protrusions linked by Eu nodes with a stoichiometric ratio of 1 : 2 (Eu : *p*-NC-(Ph)$_4$-CN-*p*). The Eu···NC interactions between four axial carbonitrile groups and one Eu atom present a distance between nitrogen of carbonitrile groups and the Eu node of 2.6 ± 0.2 Å.

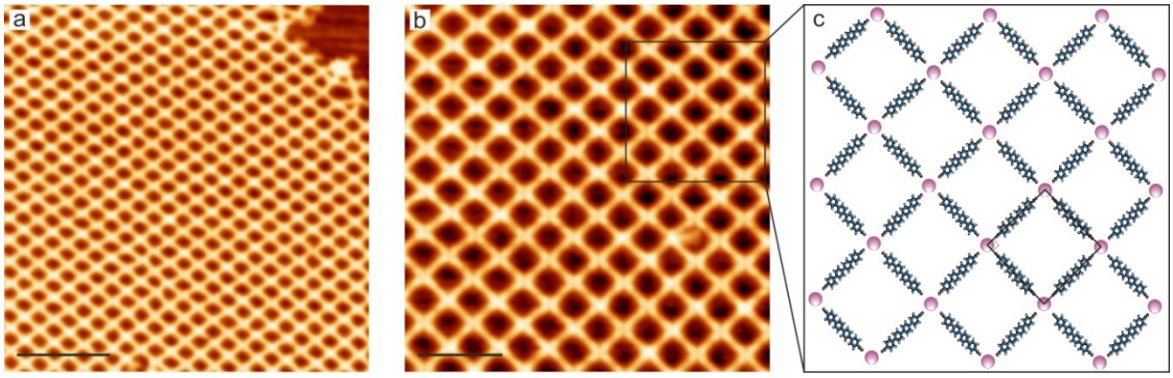

Figure 4 . 2 | Long-range Europium : *p*-NC-(Ph)$_4$-CN-*p* square planar networks

a, Large-scale topographic STM image of extended Eu-molecular linker networks (V_{bias} = -1.2 V, measured at 300 K). Scale bar: 13 nm. **b,** High-resolution STM image of **a** (V_{bias} = -1.2 V, measured at 300 K). Scale bar: 7 nm. **c,** Atomistic model of **(b)** that shows the Eu···NC interaction between four axial carbonitrile groups and one Eu atom. Carbon atoms are depicted in blue, nitrogen atoms in brown, hydrogen atoms in white and Eu atoms in purple.

Remarkably, the formation of four-fold Ce/Gd : *p*-NC-$(Ph)_{3,4}$-CN-*p* networks was never detected in our STM investigations independently of the ratio linker : Ce/Gd observed (section 3.2[40,41]). Thus, Eu metal-organic coordination on Ag(111) offers a new scenario where, for a specific stoichiometric ratio 1 : 2 (Eu : *p*-NC-$(Ph)_4$-CN-*p*) a four-fold square network prevails. This behavior can be tentatively explained by the chemical differences presented in the coordination sphere of Eu atoms. Among the divalent lanthanides, Eu^{2+} has the most accessible divalent oxidation state because of its half-filled $4f^7$ electronic configuration and, consequently, a high stabilization from exchange energy[186].

For increasing Eu : molecular linker stoichiometric ratios (2 : 5), domains of fully reticulated metal-organic networks stabilized by five-fold Eu-carbonitrile bonds emerge (cf. Figure 4.3). This reticulated network presents opening angles between adjacent linkers of 60° or 90° exhibiting Eu-NC bond lengths of 2.5 ± 0.4 Å.

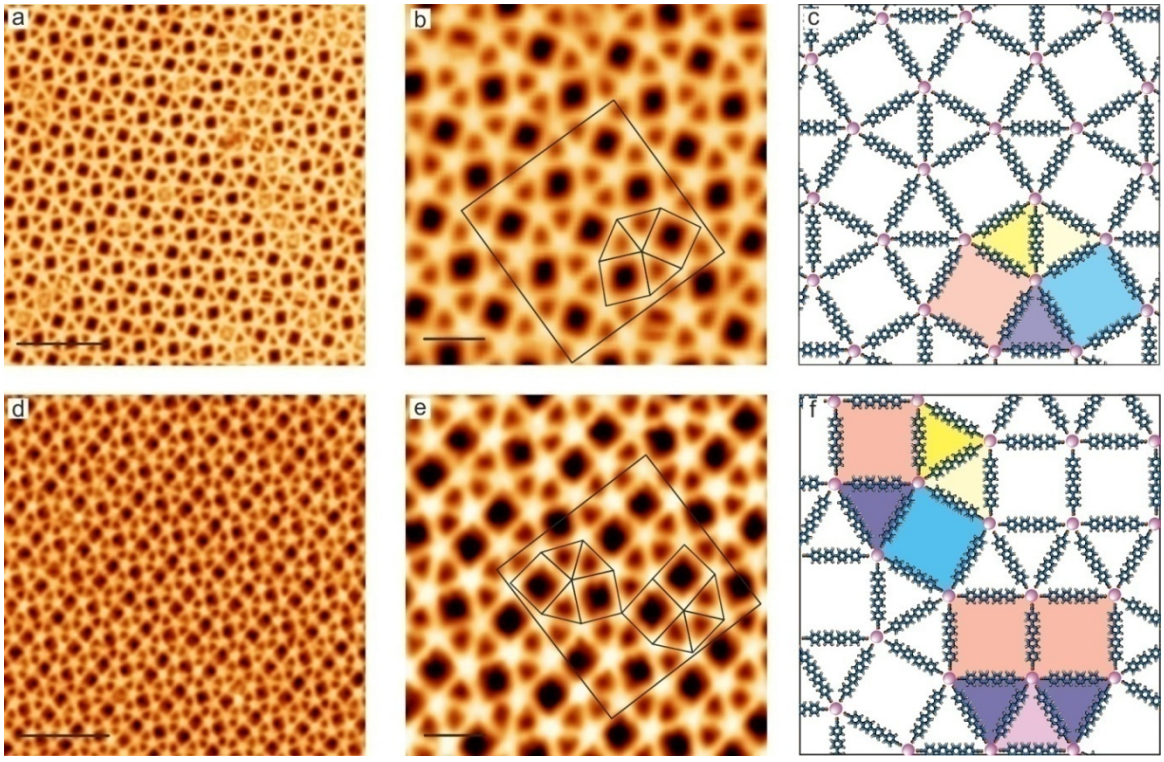

Figure 4 . 3 | Supramolecular five-fold tessellations on Ag(111) based on a 2 : 5 (Eu : molecular linker) stoichiometry

a, Large-scale topographic LT-STM image of the snub square Archimedean tessellation employing Eu and *p*-NC-$(Ph)_4$-CN-*p* linker. **b,** High resolution STM image of the snub square Archimedean tessellation phase achieved by the coordination between Eu atoms and *p*-NC-$(Ph)_4$-CN-*p* linker. **c,** Atomistic model of **(b)**

superposed with 3.3.4.3.4 sequence tiling motif. The different tile color represents the different orientation. Purple circles are assigned to single Eu centers and linkers are depicted in blue. The unit cell of the network is defined by two squares and three triangles on each vertex. **d,** Large-scale topographic LT-STM image of the mixture of semi-regular tiling motif based on 3.3.4.3.4 and 3.3.3.4.4 patterns, i.e. snub square and elongated triangular Archimedean tessellations employing Eu and *p*-NC-$(Ph)_4$-CN-*p* linker. **e,** High resolution STM image of **(d). f,** Atomistic model of **(e)** superposed with 3.3.4.3.4 and 3.3.3.4.4 sequence tiling motifs. The different tile color represents the different orientation of the unit cells. Scanning conditions: V_{bias} = -1.2 V, measured at 300 K. Scale bars: **a, d** 10 nm and **b, e** 5 nm.

It is noticed that Eu nodes are five-fold vertexes connected to adjacent nodes by the molecular linkers, following a scheme again understood as a surface tessellation based on triangles and squares. Herein two plausible scenarios are found: i) extended domains where each Eu node shares three triangles and two squares according to a 3.3.4.3.4 pattern, i.e., a snub square Archimedean tessellation (cf. Figure 4.3(a-c)), also observed in nanoarchitectures formed with Ce/Gd[40,41] and ii) extended domains where each Eu node shares three triangles and two squares according to a mixture of semi-regular tiling motif based on 3.3.4.3.4 and 3.3.3.4.4 patterns, i.e. snub square and elongated triangular Archimedean tessellations (cf. Figure 4.3(d-f)).

Even for increased stoichiometric ratios (> 2 : 5) the appearance of six-fold or higher coordination nodes is never observed. Nevertheless single organic molecules appear as cross-like motifs confined inside the square pores of the semi-regular Archimedean networks (cf. Figure 4.3(a) and Figure 4.4).

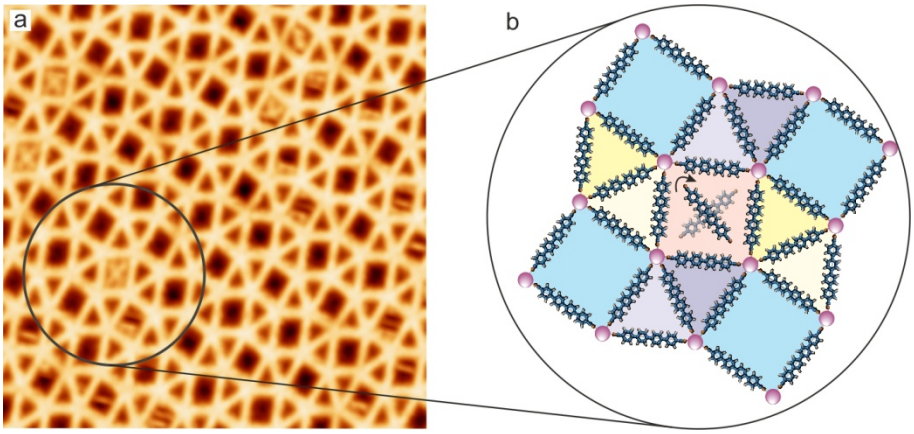

Figure 4 . 4 | Supramolecular snub square tiling tessellation

a, High-resolution STM image that shows a snub square tiling network. The black circle emphasizes a molecular linker trapped inside a square pore (V_{bias} = -1.2 V, measured at 300 K). **b,** Atomistic model of **(a).** The black arrow displays the movement of the molecular linker trapped inside the pore. The diverse colors in the background represent the different orientations of the square and triangular tilings.

This "cross-shape" is proposed to be caused by their rotation, thermally driven, which is faster than the STM scanning timescale and can be described as a molecular rotor[187,188] where the long axis of every confined molecule points at Eu nodes (Figure 4.4 (b)).

Finally, the adaptability of the Eu coordination sphere is investigated. Several studies were carried out revealing a certain degree of reversibility between the different four-fold and five-fold coordination networks as more molecular linkers or Eu atoms are deposited onto the Ag(111) surface (cf. Figure 4.5). In this sense, Figure 4.5(a-b) depicts the formation of the five-fold snub square tiling architecture after molecular deposition onto the four-fold square planar network. Furthermore, additional Eu atoms were deposited onto the mentioned five-fold snub square tiling architecture and the appearance of the four-fold square planar network is observed (cf. Figure 4.5(b-c)), emphasizing the adaptability of the Eu coordinated networks.

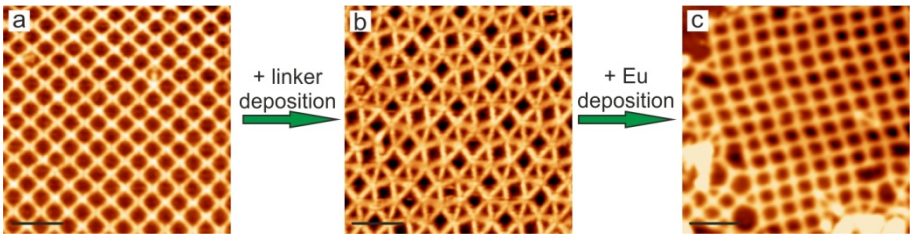

Figure 4 . 5 | Reversibility of the different Eu : *p*-NC-(Ph)$_4$-CN-*p* architectures on the Ag(111) surface

a, High-resolution STM image of the four-fold square planar network. **b,** High-resolution STM image of the five-fold snub square tiling network after deposition of molecular linkers onto the four-fold square planar network displayed in **(a). c,** STM image of the four-fold square planar network after deposition of Eu atoms onto the five-fold snub square tiling network. **a-c,** Scanning conditions: V_{bias} = -1.2 V, measured at 300 K. Scale bars: 4 nm.

4.2 *p*-NC-(Ph)$_4$-CN-*p* + Eu on Au(111)

As previously described in chapter 3, *p*-NC-Ph$_4$-CN-*p* linkers (cf. Figure 4.6(a)) have been previously used for the engineering of 2D metal-organic networks on surfaces with

transition metal centers[14,79] and with Ce and Gd lanthanide metal centers[40,41], in which, thanks to the bigger size of the rare earth vertex, five-fold coordination nodes were expressed giving rise to snub-square and elongated-triangle Archimedean motifs. Figure 4.6 illustrates the adaptability of the nanostructures designed on Au(111) following coordination of europium to quaterphenyl-4,4''-dicarbonitrile species. The europium to linker stoichiometric ratio is carefully controlled to design specific supramolecular networks: i) arbitrary string networks based on three-fold coordination nodes (cf. Figure 4.6(b,f)), ii) reticular four-fold assemblies (cf. Figure 4.6(c,g)), iii) random-tiling quasicrystals (cf. Figure 4.6(d,h)), and iv) a hexagonal lattice stabilized by six-fold nodes (cf. Figure 4.6(e,i)). Importantly, for specific Eu to linker stoichiometries only pure phases were found forming domains of hundreds of nm.

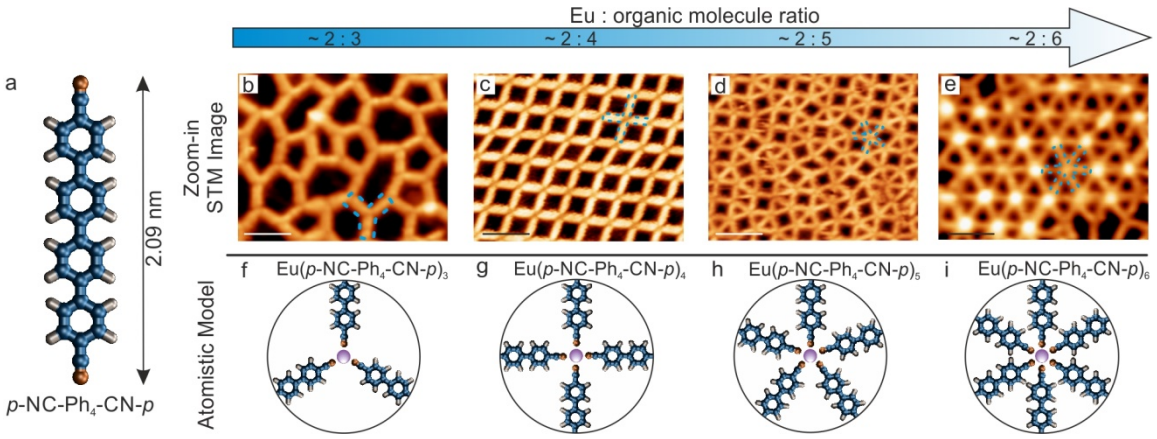

Figure 4 . 6 | Europium-directed assembly of metal-organic coordination networks on Au(111)

a, Quaterphenyl-4,4''-dicarbonitrile molecule. Carbon atoms are depicted in blue, nitrogen atoms in brown and hydrogen atoms in white. **b-e,** High resolution STM images of the distinct coordination networks designed at varying Eu : linker stoichiometries (V_{bias} = -1.2 V, measured at 300 K). Scale bar: 5 nm. **f-i,** Atomistic models of **(b-e)** highlighting the distinct coordination nodes stabilizing the assemblies. Eu atoms are illustrated in purple.

In addition, mixtures of phases based on combinations of: i) three-fold and four-fold nodes and ii) four-fold and five-fold vertexes could also be fabricated by selecting an intermediate stoichiometry between two pure phases (Figure 4.7). This degree of adaptability is uncommon for surface-confined coordination nodes and arises from the size of Eu center combined with the specific properties of lanthanides, whereby the

resulting metal-organic bonds are predominantly ionic with a minor contribution of covalency and thus allow for augmented flexibility[88].

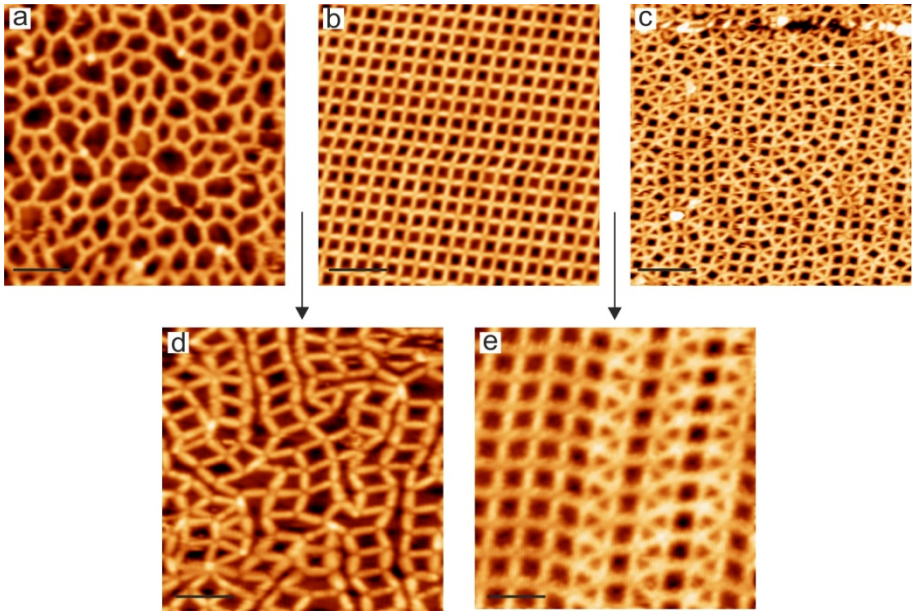

Figure 4 . 7 | Distinct europium-directed assemblies fabricated on Au(111) by regulating the Eu to linker stoichiometry

a-e, High-resolution STM images. **a,** Arbitrary string network based on three-fold coordination. **b,** Reticular four-fold assembly and c, Random-tiling quasicrystal (V_{bias} = -1.2 V, measured at 300 K). Scale bars: 10 nm. **d,** Irregular nanoarchitecture based on three-fold and four-fold nodes. **e,** Mixture of the reticular phase and an elongated triangle tiling tessellation, based on four-fold and five-fold coordination nodes, respectively. V_{bias} = -1.2 V, measured at 300 K. Scale bars: 5 nm.

The most interesting phase is the porous open network obtained at a ≈ 2 : 5.1 (Eu : *p*-NC-Ph_4-CN-*p*) stoichiometry (cf. Figure 4.6(d), Figure 4.8(a) and Figure 4.9(a)). Molecular linkers are imaged as rod-like protrusions connected by Eu nodes. Herein, we identify distinct coordination nodes interconnected by the linkers and spanning a complex and fully reticulated MOCN. Individual Eu centers are surrounded by four, five or six molecules, establishing Eu-NC bonds with a projected length of 2.6 ± 0.4 Å. Moreover, Eu vertexes are distributed in such a fashion that the design can be interpreted as a tessellation based on a random-tiling of squares and triangles ENREF_71, as highlighted in white in Figure 4.8(a). The expressed four types of coordination motifs are classified as six-fold hexagonal 3.3.3.3.3.3 (cf. Figure 4.8(c,g)), five-fold snub-square 3.3.4.3.4 (cf. Figure 4.8(d,h)), five-fold elongated-triangle 3.3.3.4.4 (cf. Figure 4.8(e,i)), and four-fold

4.4.4.4 (cf. Figure 4.8(f,j)). The six-fold node (3.3.3.3.3.3) is the center of a dodecagonal distribution of Eu nodes (highlighted in black in Figure 4.8(a) and emphasized artistically in Figure 4.8(b)). High-resolution images and modelling of the nodes show the expected intermolecular opening angles of ≈ 60° and ≈ 90° for the triangle and the square tiles, respectively.

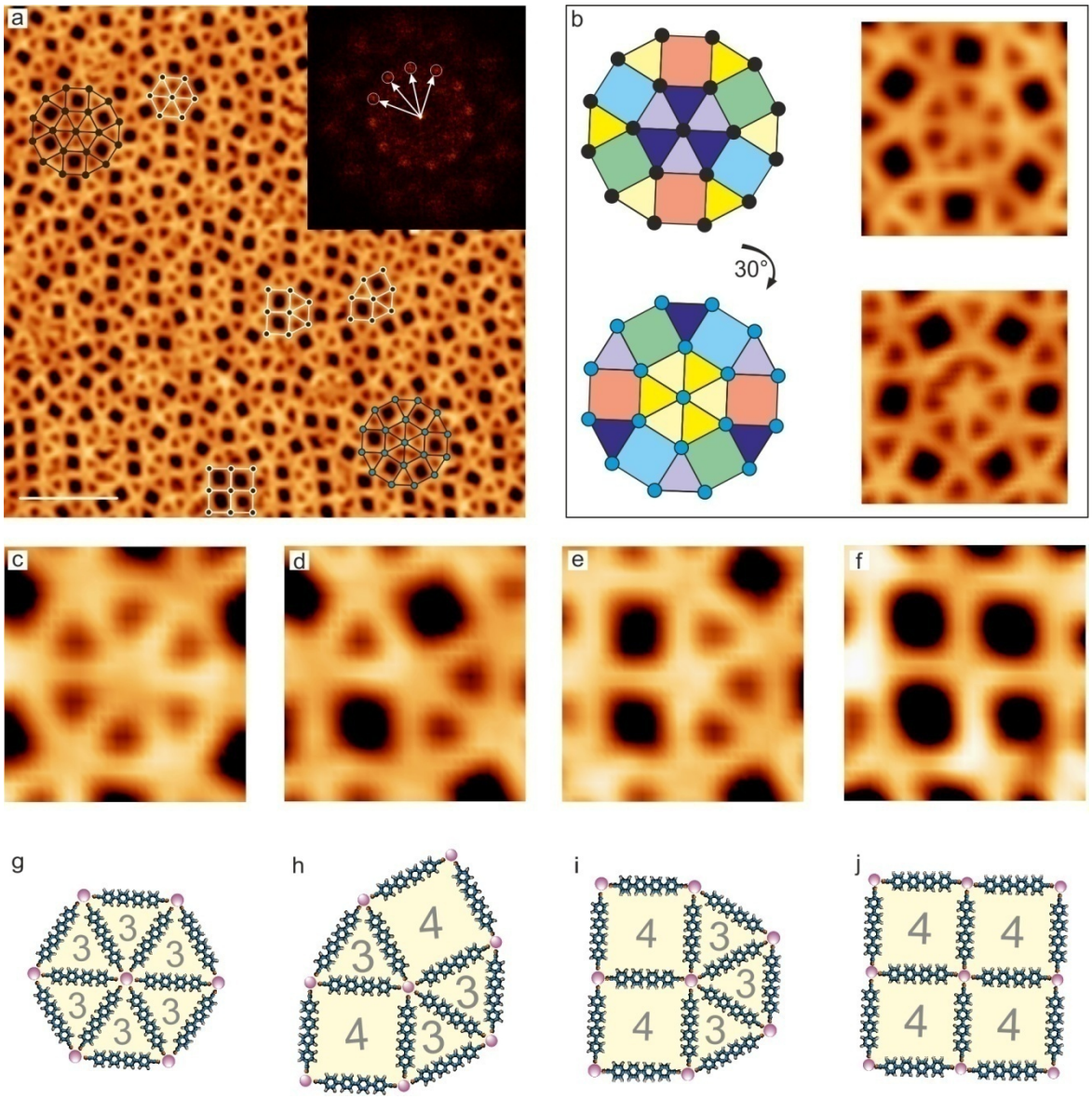

Figure 4 . 8 | 2D metal-organic random-tiling quasicrystal

a, Long-range STM image of the quasicrystalline MOCN designed on Au(111) by depositing *p*-NC-Ph_4-CN-*p* and Europium at a ≈ 2 : 5.1 stoichiometric ratio (V_{bias} = -1.2 V, measured at 300 K). Scale bar: 10 nm. The inset represents the 12-fold symmetry 2D-FFT. **b,** The incorporated dodecagonal motifs with 30° rotational symmetry: Different colors of squares and triangles symbolize distinct orientations with respect to the underlying surface. **c-f,** Classification of distinct network motifs with six-fold (3.3.3.3.3.3), five-fold (3.3.4.3.4 or 3.3.3.4.4) and four-fold coordination (4.4.4.4); **g-j,** show corresponding atomistic models.

The six-fold node at the center of a 3.3.3.3.3.3 arrangement induces an alternating square-triangle decoration at its exterior with dodecagonal distribution of Eu centers (highlighted in black in Figure 4.8(a) and emphasized artistically in Figure 4.8(b)). For symmetry reasons, two 3.3.3.3.3.3 arrangements must exist differing in their orientation by 30°, which can be readily identified in the STM data (cf. Figure 4.8(b)). This illustrates at the same time the specific orientations of the tiling units, where three distinct orientations exist for the squares and four for the triangles, respectively. Accordingly the 12-fold symmetry is also manifested in the twelve possible orientations of the molecular linkers.

In addition, a statistical analysis (> 400 nodes) reveals prevalence of the 3.3.4.3.4 node (62 %), followed by 3.3.3.4.4 (13 %), 3.3.3.3.3.3 (6 %), and 4.4.4.4 (2 %), with 17 % of defective nodes. These type of irregularities, identified as D_1, D_2 and D_3 in Figure 4.9(d-e), have been previously reported in other studies of quasicrystallinity assuming their inherent disorder[148,153].

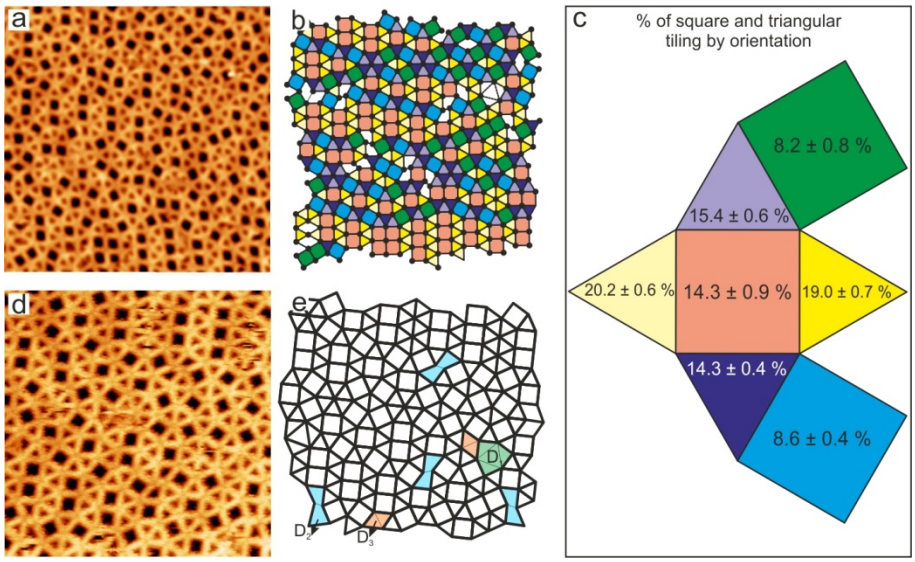

Figure 4 . 9 | 2D random-tiling quasicrystal and its structural defects

a, Long-range STM image of a dodecagonal random-tiling quasicrystal achieved on Au(111) by depositing *p*-NC-Ph_4-CN-*p* and Europium at a ≈ 2 : 5.1 stoichiometric ratio (V_{bias} = -1.2 V, measured at 300 K). **b,** Geometrical model of **(a)**. The different colors of squares and triangles point out the distinct orientations with respect to the surface of the triangle and square tiles. In white three types of defective nodes are observed. **c,** Percentage of square and triangular tiling given by their orientation. **d,** High resolution STM

image of a dodecagonal random-tiling quasicrystal (Vbias = -1.2 V, measured at 300 K). Scale bar: 4 nm. **e,** Stick model where typical defects are depicted. D_1, D_2 and D_3, illustrated in green, blue and orange respectively, show the structural imperfections presented in the 2D random-tiling QC.

Detailed data analysis of this random-tiling quasicrystalline structure reveals specific orientations of the tiles with respect to the substrate: three orientations for the squares and four orientations for the triangles. Thus, a slight preference of some orientations (cf. Figure 4.10(a-c)), implying deviations from a perfect quasicrystalline lattice, similarly encountered in other random-tiling quasicrystalline systems[158].

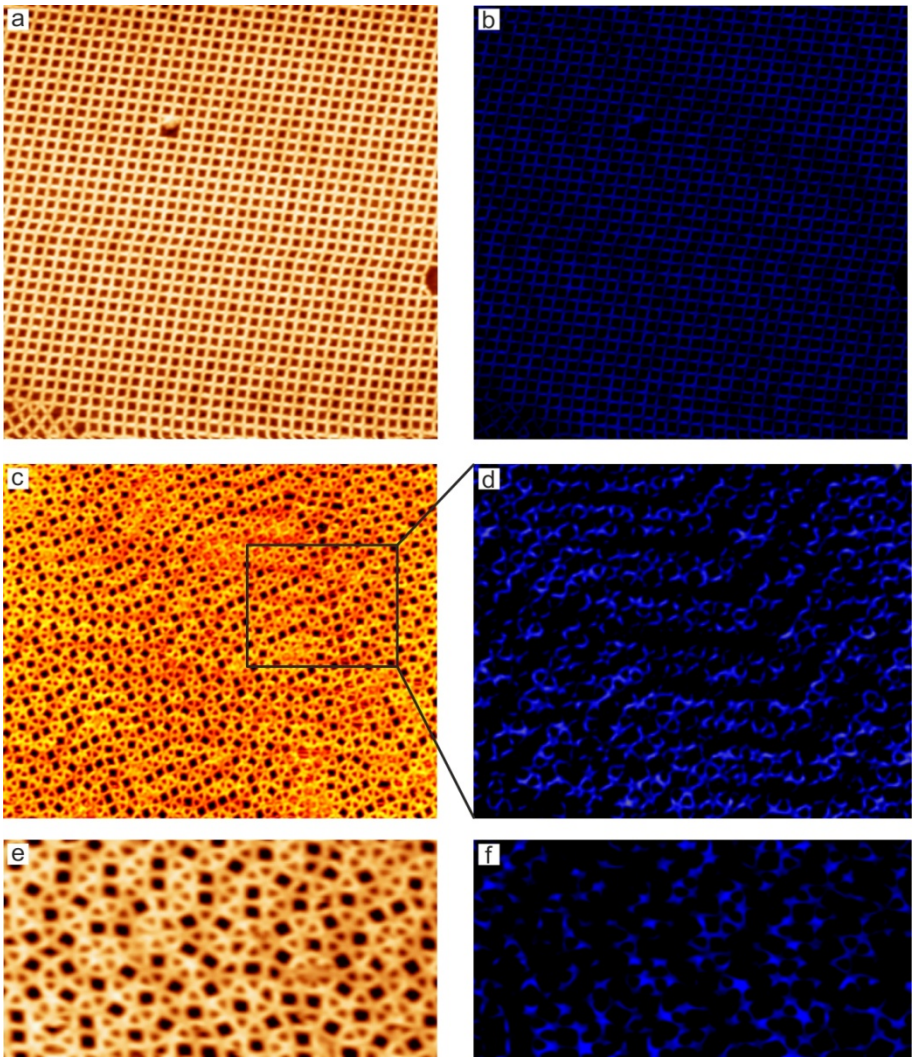

Figure 4 . 10 | Mesoscopic substrate patterning due to the chevron √3 x 22 reconstruction of Au(111)

a, c, e, High resolution STM images of fourfold, fivefold and ddQC phases respectively. **b, d, f,** Bluish-black color-code to enhance the presence of the chevron reconstruction. Scanning conditions: V_{bias} = -1.2 V, measured at 300 K.

A possible reason for this behavior might be the influence of the Au(111) surface reconstruction originating from a locally uniaxial contraction of the surface layer with a $\sqrt{3}$x22 unit cell. On large terraces the pertaining chevron pattern introduces an overall inhomogenous contraction of the surface layer, where two from three possible rotational domains prevail. Following the MOCN formation this mesoscopic substrate patterning persists.

The influence of surface templating and preparation conditions can moreover locally stabilize small areas with elongated triangle 3.3.3.4.4 patterns, as shown in Figure 4.11, where they appear in the vicinity of step edges. This underlines the established close relationship of these phases also for the present MOCN-type ddQC. However, the respective stochiometries are slightly different: whereas the random-tiling ddQC implies a Eu : *p*-NC-Ph_4-CN-*p* ratio of 2 : 5.1, that of the approximants is exactly 2 : 5, i.e. slight concentration variations may also interefere in the stabilization of a ddQC vs. an approximant phase.

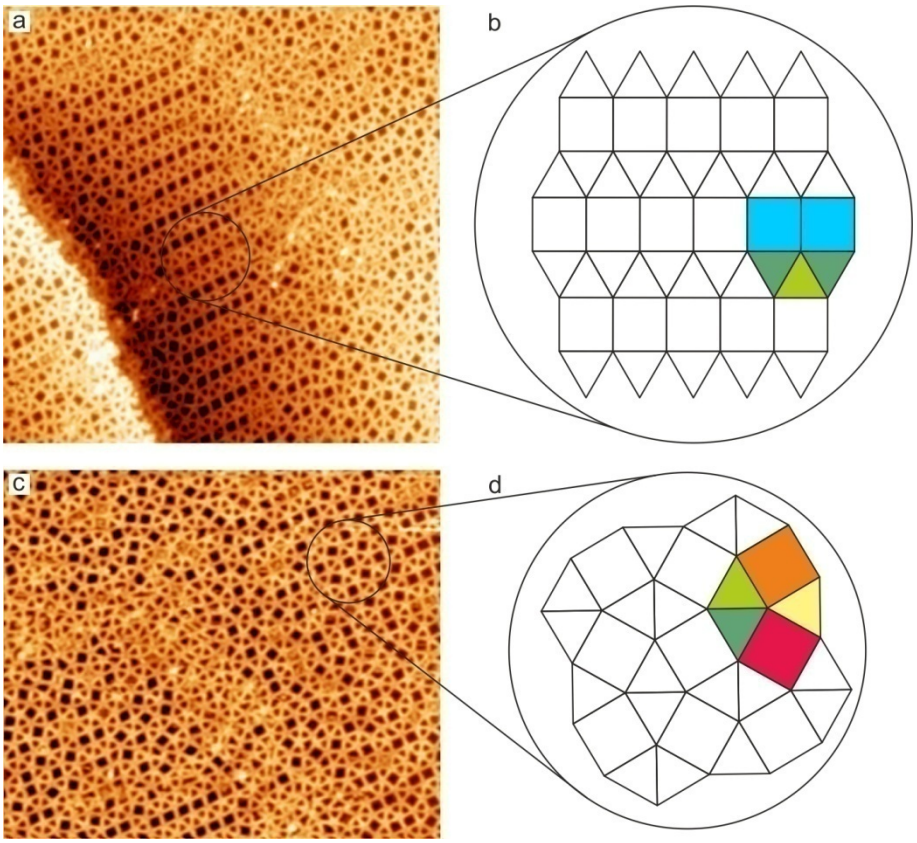

Figure 4 . 11 | Formation of semi-regular tiling domains

a, c, High resolution STM images of the elongated triangular tiling (3.3.3.4.4) and the snub square tiling (3.4.3.4.4) domains. **b, d,** Zoom-in models of the elongated triangular tiling and the snub square tiling respectively. Colored squares and triangles represent the 3.3.3.4.4 and the 3.3.4.3.4 unit cells. Scanning conditions: V_{bias} = -1.2 V, measured at 300 K.

Random square-triangle tilings are associated with dodecagonal quasicrystallinity[178]. The FFT is depicted in Figure 4.8(a) and Figure 4.12 revealing modulated ring-patterns with dodecagonal symmetry. Similar diffraction signatures were found in other dodecagonal quasicrystals in experiments[148,149,153,156,162] or simulations[183,184,189].

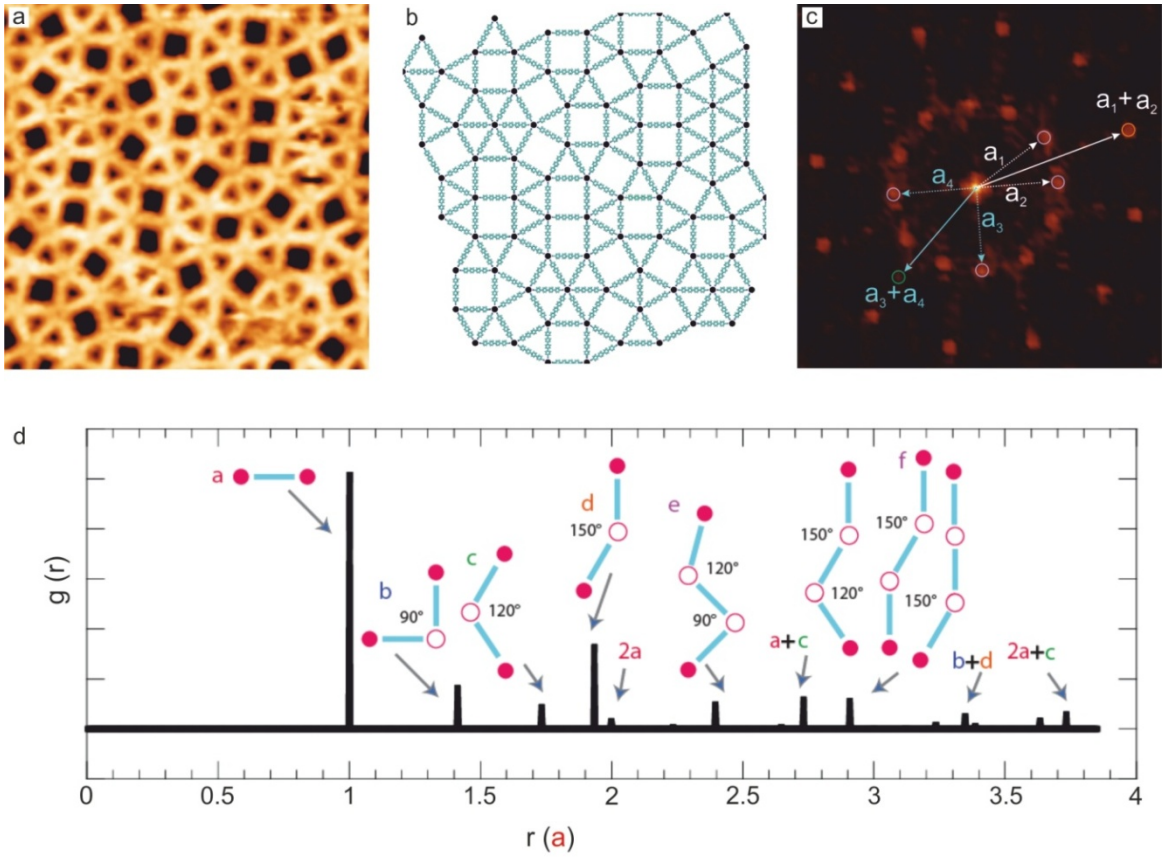

Figure 4 . 12 | Dodecagonal random-tiling quasicrystal

a, High-resolution STM image (data obtained at 300 K. Image size: 146 $Å^2$; scanning parameters: V_{bias} = -1.2 V). **b,** Molecular mechanics relaxed structure of **(a)**, with Eu-N distance from MP2 calculations. The different colors of squares and triangles point out the different orientations presented in the dodecagon. **c,** 2D-FFT of (**b)** showing a 12-fold rotational symmetry. The inner ring contains the basis vectors $\mathbf{a}_i$. The second ring is obtained from all sums of vector pairs in the inner ring that are separated by 90 degrees. The third ring is achieved from all the sums of two adjacent vectors in the inner ring. **d,** radial distribution function of the metal nodes in b showing a series of connection motifs. Units are in increments of the Eu-linker-Eu side distance of a = 25.96 Å.

Thus the rationalization of the metal-organic architecture as random square-triangle tiling, comprising a repetition of dodecagonal structural units with adequate distribution of triangles and squares, the distinct FFT peaks with dodecagonal symmetry reminiscent of the evidence in quasicrystalline micelles[147], binary nanoparticles[153,162] and polymers[148], allow us to conclude that the Eu-directed assembly of quaterphenyl-4,4''-dicarbonitrile linkers on Au(111) drives the expression of dodecagonal random-tiling quasicrystals. Furthermore, a statistical analysis of the assembly, clearly shows signatures of a random square-triangle pattern, giving an inherent triangle to square number ratio of 2.36 ± 0.01. This value holds at the mesoscopic level (average ratio of 2.22 ± 0.02) and comes close to the expectation for a perfect quasicrystal ($\approx 4/\sqrt{3} = 2.31$)[148].

Finally, we briefly address the possible reasons for the appearance of quasiperiodicity in 2D MOCNs. Previous modeling approaches (e.g., employing Monte-Carlo methods) indicate the balance between enthalpy and entropy as key parameter for random-tiling quasiperiodicity[161,163,164,182,183,190]. Regarding entropy, the present system can be interpreted as the classical random tessellation of triangles and squares[179,190], whereby entropic forces maximize randomness. Concerning enthalpy, two main contributions are relevant: adlayer/substrate and lateral metal-ligand interactions. On Au(111) the spontaneous formation and coexistence of surface-confined four-, five- and six-fold planar coordination nodes is an exceptional situation and points to weak surface interactions, which are reflected by the conservation of the substrate's chevron reconstruction (cf. Figure 4.10). In order to study the propensity of flexible Eu-nitrile coordination nodes towards quasicrystallinity the Ag(111) surface was utilized for comparison (section 4.1). Although formation of distinct MOCNs depending on the stoichiometry of the constituents occurs (cf. Figure 4.6), the variety of vertexes is reduced and quasiperiodic patterns are absent, mainly because the six-fold node is not expressed. It is suggested that: (i) surface interactions are weaker for Au(111) than Ag(111) allowing increased adaptivity of the CN-endgroups during the coordination. This argument is also supported by the fact that the interphenyl twist angle of the oligophenylene backbones on Au(111)[191] _ENREF_191 exceeds that on Ag(111)[105,192] _ENREF_192 _ENREF_56, implying a more relaxed molecular geometry and an

increased adsorption height, in agreement with trends of other aromatic adsorbate systems[193] _ENREF_194. Possibly in relation to this, because the higher twist angle may reduce packing constraints in the vicinity of the vertex, (ii) the Eu coordination sphere can be engaged in up to six lateral coordinative links. Thus, at a specific stoichiometry, the balance between in-plane metal-organic and adlayer-substrate interactions combined with entropy contributions are responsible for the network formation_ENREF_31[182,183,190]. In the case of the Au(111), weak templating allows the full expression of random-tiling quasicrystallinity, whereas on Ag(111), a slightly stronger adsorption of the constituents precludes such a manifestation. Finally, it is sugggested that efforts to model these findings will provide further insights into the intriguing questions associated with QC evolution. The open-network assembly, variation of coordination nodes with minute flexibility for internode distances offers an interesting testbed for computational modeling useful to disentangle entropic and energetic contributions. The system can be described in a scenario with weighted distribution of linker connections (4-6-fold coordination nodes with different binding energy) while imposing a rather rigid connection between adjacent vertices, given by the metal-ligand bonding distance and linker extension, where only minor variations are expected.

4.3 Conclusion

In summary, we have introduced the chemistry of Eu-directed surface-confined metal-organic networks on different substrates as Ag(111) and Au(111) manifesting the importance of the adlayer/substrate interaction.

On the Ag(111) surface the adaptability of the Eu coordination sphere is investigated giving rise to four-fold reticular architectures and five-fold semi-regular Archimedean tilings. A new tessellation of the plane is found based on the coexistance of 3.3.3.4.4 and 3.3.4.3.4 five-fold coordination nodes. The expression of manyfold coordination networks depending on the stoichiometric ratio Eu : molecular linker was not observed for surface-confined Ce and Gd directed networks on Ag(111) (cf. chapter 3). Two of the most relevant characteristic properties of Eu ions are their large ionic radius which largely depends upon the coordination number and the differences in the electronic configurations of Ce/Gd lanthanide elements. Eu possesses a ground state electronic

configuration [Xe] $4f^7$ $6s^2$ and the formation of Eu^{+2} ([Xe] $4f^7$) can be produced because of its half-filled $4f^7$ electronic configuration, though Eu^{+3} ([Xe] $4f^6$) is still the most stable oxidation state. Consequently, Eu ions can easily adapt to many different coordination environments, making them one of the most versatile elements of coordination chemistry.

On the Au(111) surface the expression of manyfold coordination nodes is observed. Herein, the Eu : molecular linker stoichiometric ratio is carefully controlled to design specific metallosupramolecular networks. In addition, by selecting an intermediate stoichiometry between two pure phases, a mixture of them based on three-fold and four-fold nodes and four-fold and five-fold combined nodes was also fabricated. For a stoichiometric ratio 2 : 5.1 (Eu : molecular linker) a dodecagonal random-tiling quasicrystal, whose expression is estimulated by the big and flexible coordination sphere of the lanthanide center is observed. Herein, the adequate adlayer/substrate interaction, and the convenient entropic tessellation of the surface, favored by low demanding steric restrictions play a crucial role in the expression of the quasicrystalline structure. By exploiting the versatility of lanthanide coordination chemistry, we envision to design more perfect quasicrystals in two-dimensions and to extend the quasiperiodic order to other fields in materials science, taking advantage of metal-organic coordination.

In chapters 3 and 4 we have inspected the interactions between dicarbonitrile polyphenyl linkers and Ce, Gd or Eu atoms on the Ag(111) surface for the three of them and on Au(111) for the Eu system. In the next chapter we introduce a carbonitrile porphyrin derivate as the molecular building block, exploring its coordination interactions with gadolinium and cobalt atoms on a Ag(111) substrate.

5. Orthogonal insertion of lanthanide (Gd) and transition metal (Co) atoms in metal-organic networks on surfaces

Since Protoporphyrin IX (a β-substituted free-base precursor for haemoglobin, cytochrome c and chlorophylls) was identified and recognized as a fundamental mediator in several biosynthetic pathways formidable efforts were dedicated to the understanding of even more complex tetrapyrrole species[194]. This fact is due to their extraordinary variety of functional properties used in artificial and natural arrangements. The porphyrinic macrocycle is exceptionally stable and the four internal nitrogen atoms form a central pocket perfectly located for the incorporation of metal atoms (Fe, Co or Mg are predominant in biological systems).

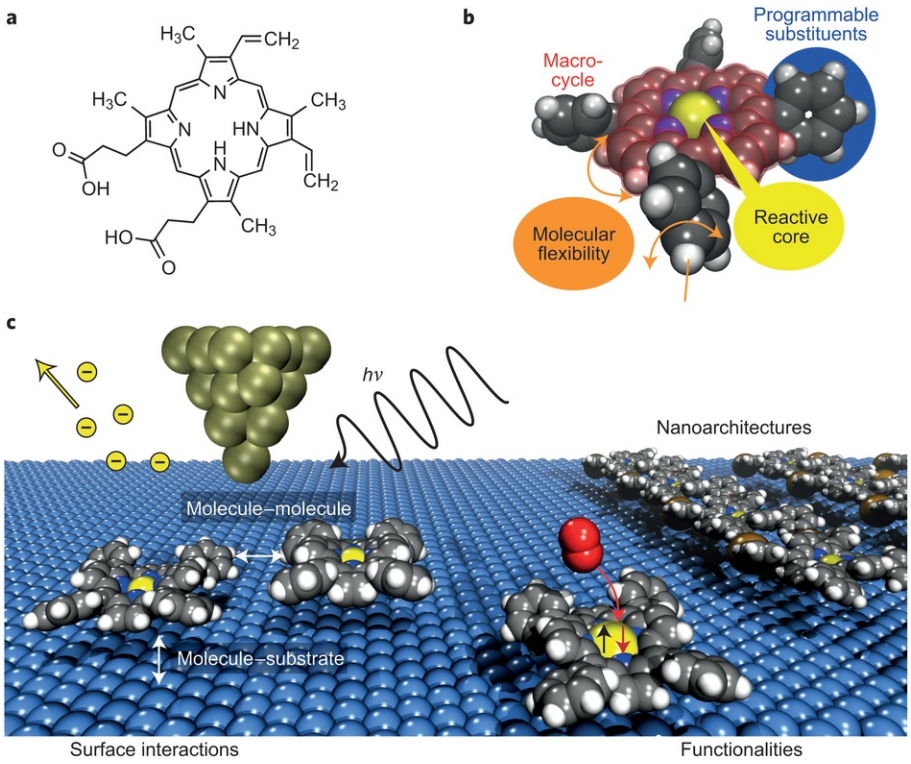

Figure 5 . 1 | Key characteristics of porphyrins and their control at surfaces

a, Protoporphyrin IX, a β-substituted free-base precursor for haem, cytochrome c and chlorophylls in biosynthesis. **b,** The possible incorporation of different metal centers (yellow) with four-fold coordination

in the tetradentate ligand bestows extraordinary versatility on tetrapyrrole units. The flexibility of the macrocycle and its interplay with *meso*-substituents, illustrated for a tetra-aryl species, plays a part in many processes and co-determines the molecule´s attributes. Arrows indicate dihedral angle rotation and macrocycle flexure. **c,** Upon adsorption, characteristic conformational adaptations arise because of the interfacial bonding, frequently favoring the configuration shown, with a distorted macrocycle facing the substrate. The pertaining electronic features and functional properties are affected by the surface confinement and ligation of axial adducts. Lateral interactions between molecular units mediate the expression of specific nanoarchitectures that can be tailored by appropriate substituents and assembly protocols. Scanning probe microscopy investigations provide molecular-level insight, and space-averaging spectroscopies offer detailed knowledge on physicochemical properties. Figure adapted from reference[15]. ENREF_114

Tailored substituents can improve their performance guiding their arrangement in specific environments and mediating in their molecular assembly. In particular, free-base and metalated porphyrins[195,196] have revealed to be exceptional scaffolds[197] to be deposited on surfaces[15,198,199]. Surface interactions can influence the coordination sphere of complexed metal centers, with repercussion for their chemical, magnetic or electronic properties. Thus, metallo-tetrapyrroles in flat adsorption geometry present coordinative unsaturated sites that depending on the metal affinity towards axial ligands provide potentials for sensing[200-202], catalysis[203,204] and magnetochemistry[202].

Molecular-level investigations focused on assembly protocols exploiting orthogonal coordination interactions (understood as functional groups that exhibit significant differences in their chemical reactivities) were rarely reported to date. Though this approach has been recognized as a versatile conceptual basis to engineer novel materials and nanoarchitectures providing multimodal functionalities, mostly limited to space-averaging studies employing surface-tethered self-assembled monolayers as platforms[205]. This approach is particularly promising regarding the exploration of pathways to control the organization of different units, including metal centers in a programmed fashion. Scheme 1 illustrates potential routes to organize specific metal centers by combining orthogonal metal-organic interactions on surfaces, either exploiting peripheral ligand groups (cf. Scheme 1a, illustrating a hypothetic case) or by making use of both peripheral moieties and intramolecular macrocycles (cf. Scheme 1b, illustrating the scenario realized successfully). In this respect, surface-confined hybrid systems containing both lanthanides and transition metal centers are particularly

promising as they could afford new functional materials with properties that cannot be obtained from the single elements[206-208]. Potential applications include magneto-responsive devices and molecular spintronics, where unique features can be obtained by magnetic exchange interactions between 3d and 4f elements[38,208].

Considering the low activation barrier for the metalation reaction of tetradentate free-base tetrapyrroles toward small-size metal atoms like Co or Fe[209-211], one could in principle orthogonally coordinate[205,212] peripheral ligands with larger-size atoms like lanthanides. Given this premise, we introduce an approach exploiting the combination of orthogonal coordination interactions on surfaces towards exemplary d-f nanoarchitectures.

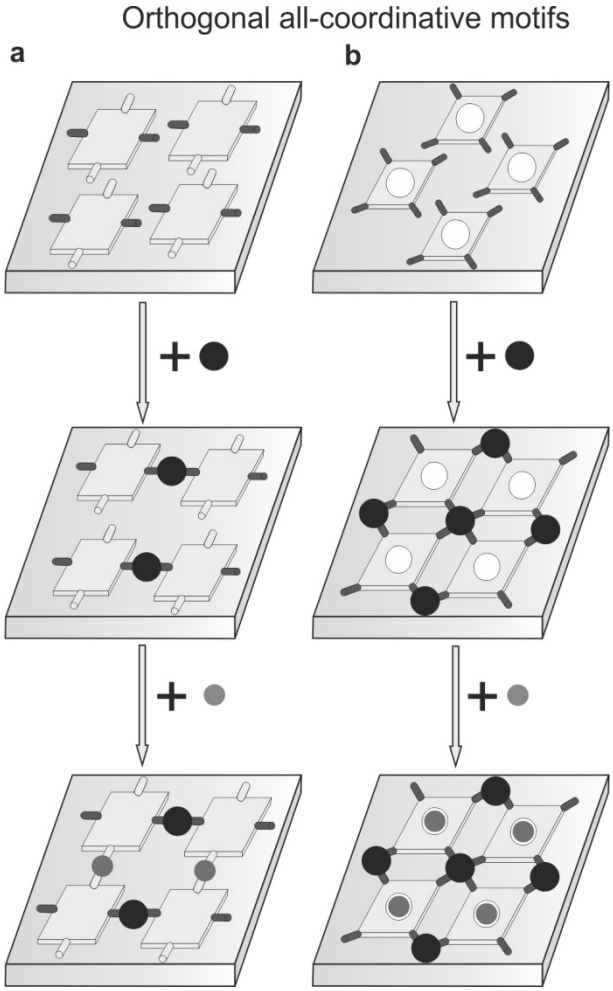

Scheme 1 | Illustration of envisaged approaches towards bimetallic networks exploiting coordinative interactions

Combination of two orthogonal coordinative motifs **(a)** making use of peripheral ligands and **(b)** benefiting from peripheral moieties and intramolecular macrocycles. Metal atoms are depicted by light and dark grey spheres, respectively.

LT-STM experiments realized in this chapter were carried out at TUM (Technische Universität München).

5.1 Deposition of 2H-TPCN on Ag(111)

The deposition of a submonolayer coverage of tetra-biphenylcarbonitrileporphyrin (2H-TPCN, see Figure 5.2) on Ag(111) held at room temperature results in the formation of a two-dimensional molecular close-packed tetragonal assembly (cf. Figure 5.2(b)). This network presents single domains spanning extensions of several hundreds of nanometers, which reveals a low-diffusion barrier of 2H-TPCN, as observed for similar substituted porphyrins on Ag(111). High-resolution STM data (cf. Figure 5.2(c)) allow us to discern submolecular features and the layer organization. The molecular species present a two-fold symmetric appearance, where the peripheral 4-cyano-biphenyl ligands are observed as four bright protrusions and the tetrapyrrolic macrocycle of each porphyrin species is visualized as a ring exhibiting a bright or a dim appearance (blue or green contour plot in Figure 5.2(c)).

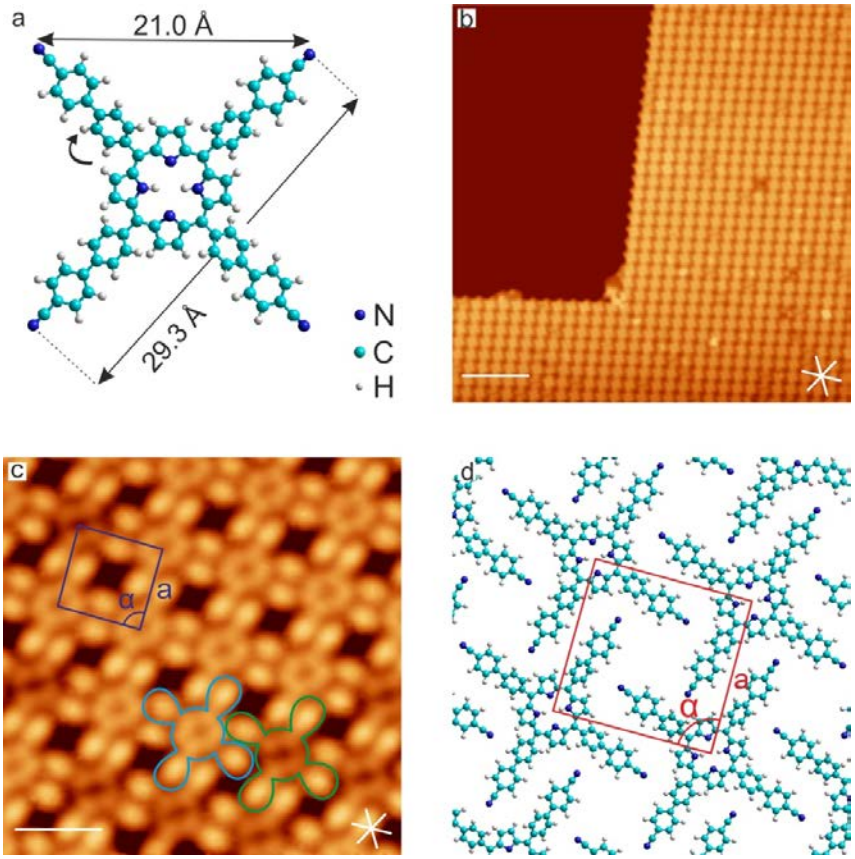

Figure 5 . 2 | Tetragonal network formed upon self-assembly of 2H-TPCN on Ag(111)

a, Top-view: ball-and-stick model of 2H-TPCN. **b,** Overview STM image showing a single long-range ordered molecular domain (V_b = 1 V and I = 100 pA). **c,** High-resolution STM image where submolecular features can be identified. The colored contours (green and blue) indicate the two tetrapyrrolic tautomers (V_b = -0.5 V and I = 70 pA). **d,** Zoom-in molecular model of the assembly presented in **(c)**. The square unit cell is shown in red, where *a* represent the unit vector and *α* the unit cell angle. For **(a)** and **(d)** C, N, and H atoms are depicted in green, blue and white, respectively.

2H-TPCN species present two hydrogen atoms in their inner cavity being localized at opposite pyrrole groups, existing two possible configurations described by a rotation of 90° of the proton pair. Applying a tunneling current at a voltage that exceeds a given threshold can derive in a reversible switching between configurations, associated to a transfer of the proton pair. Thus, the appearance of the inner cavity is the result of the proton tautomerization equilibrium of the inner cycle (cf. Figure 5.3), previously observed in surface-confined tetrapyrroles[135].

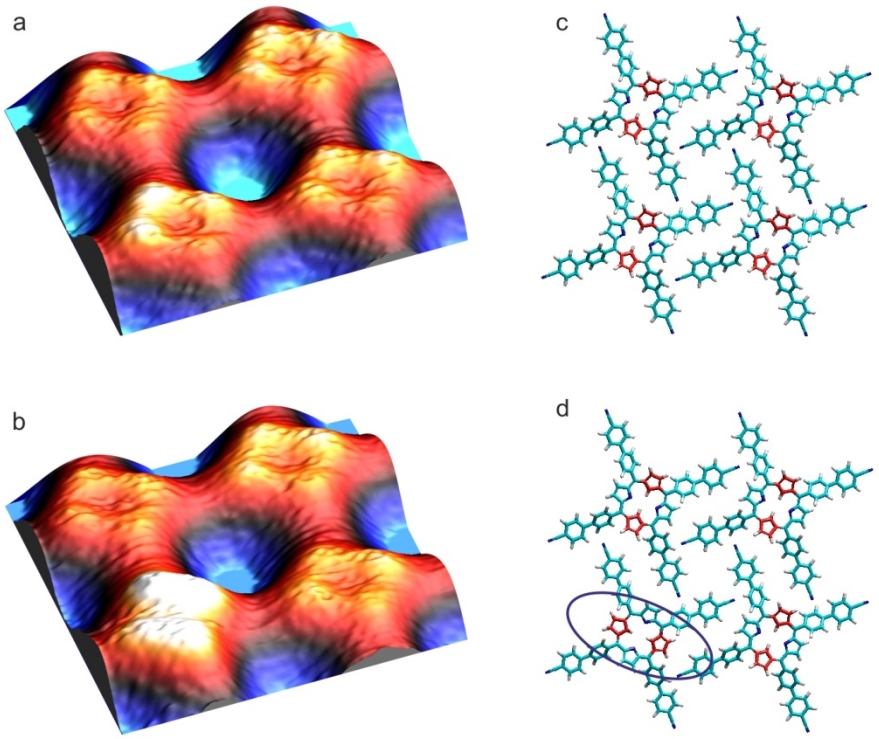

Figure 5 . 3 | Double proton transfer in 2H-TPCN species

a-b, Pseudo three-dimensional rendering of STM high resolution images presenting a brighter 2H-TPCN molecule after a voltage pulse of 1.5 V. **c-d,** Atomistic models of **(a)** and **(b)**, highlighting in red the inner protonated pyrroles.

The supramolecular network presents a tetragonal unit cell of a = 20.4 ± 0.4 Å (internal angle α = 90 ± 1°) and features organizational chirality exhibiting three pairs of mirror-symmetric domains (cf. Figure 5.4). Within each domain only one molecular orientation is detected.

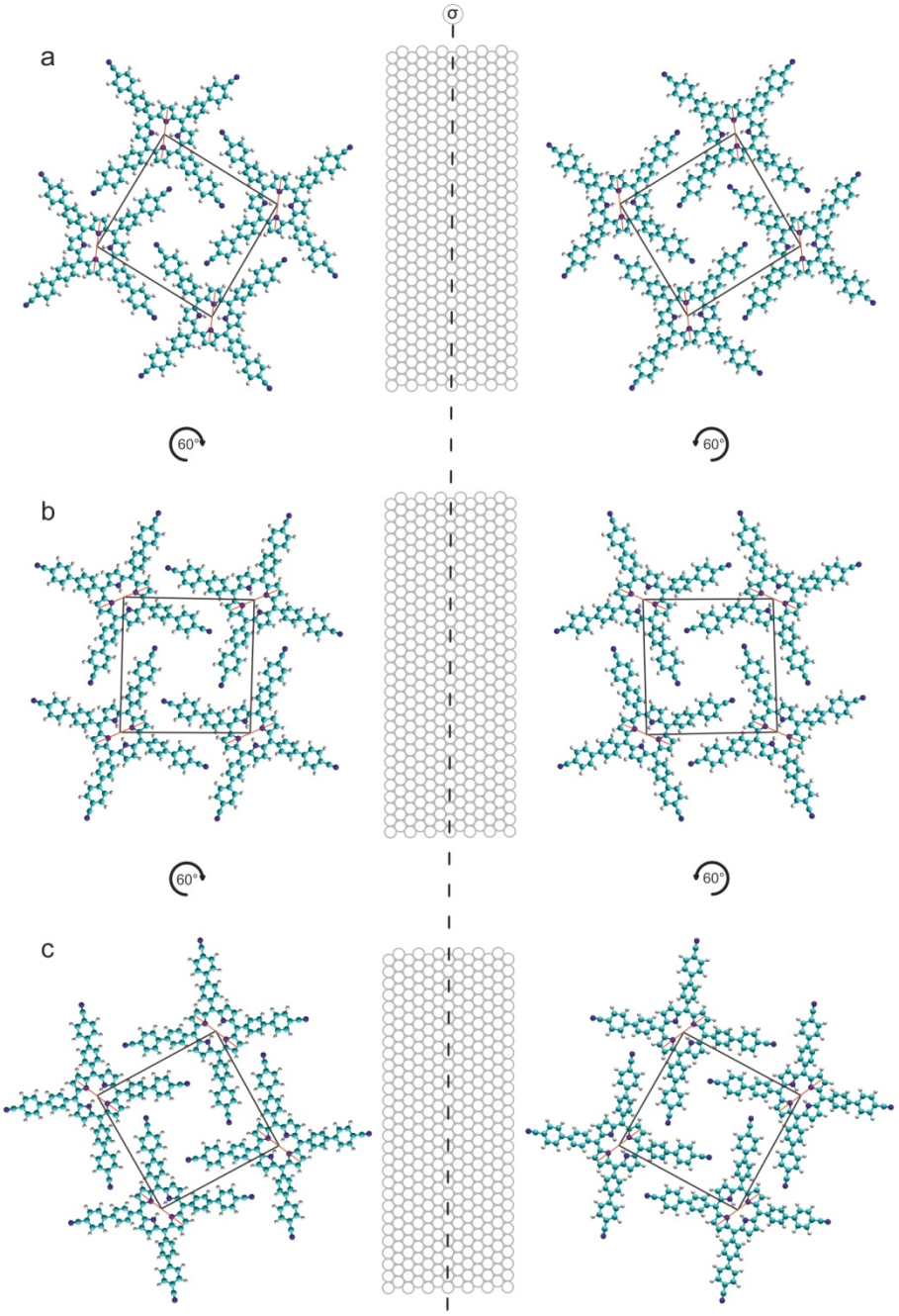

Figure 5 . 4 | Atomistic model of six mirror-symmetric domains observed for 2H-TPCN on Ag(111)

5.2 Orthogonal insertion of lanthanide-transition metal nanoarchitectures by selective metal-organic coordination

5.2.1 Gd : TPCN metal-organic coordination networks

In order to explore the affinity of 2H-TPCN towards a lanthanide element, Gd atoms are evaporated at ≈ 300 K onto a previously prepared submonolayer molecular coverage. Following, a drastic change in the structure of the network is detected. Figure 5.5(a-b) displays a large-scale image revealing the formation of an extended porous network featuring a grid-like topology. High-resolution images (cf. Figure 5.5(c)) clearly display the four-fold coordination of Gd with the terminal carbonitrile groups, following a 1 : 1 (Gd : 2H-TPCN) stoichiometric ratio, as schematized in the model of Figure 5.5(d). Hereby, the Gd nodes are distinguished as the brightest round protrusions, whereas the porphyrin species present a four-fold appearance with a striking difference as compared to the non-coordinated molecules described above: the terminal groups look dimmer, indicating the formation of a lanthanide-organic bond.

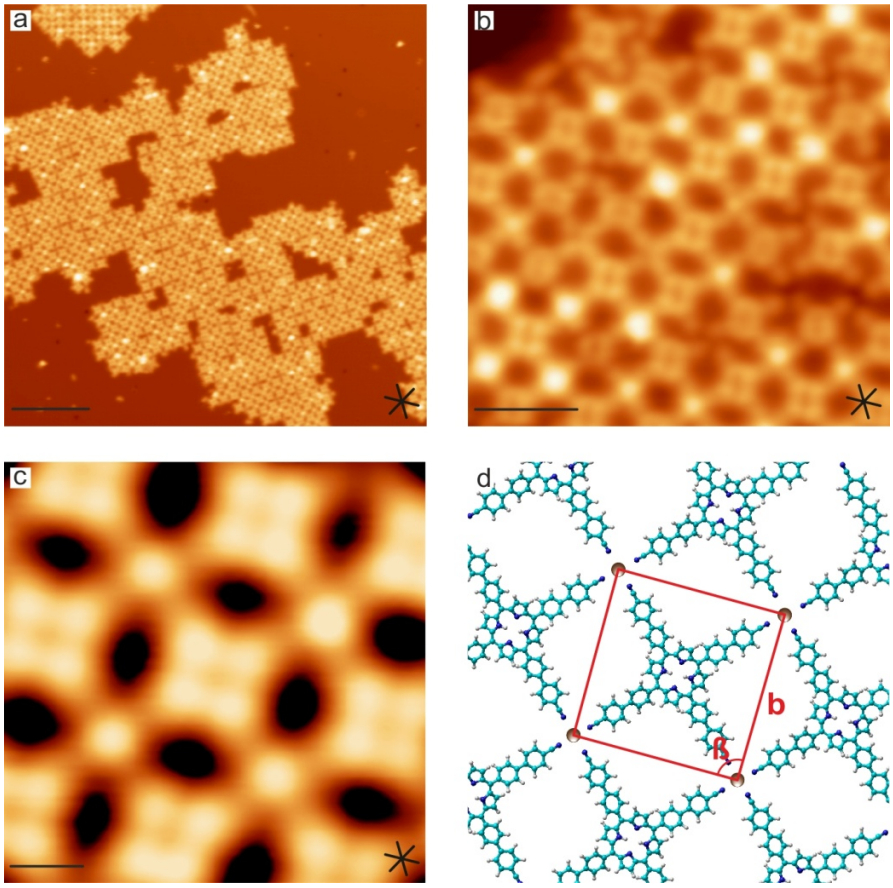

Figure 5 . 5 | Four-fold Gd-carbonitrile supramolecular architecture on Ag(111), obtained from the Gd-directed assembly of 2H-TPCN species

a, Overview STM image (V_{bias} = 0.5 V and I = 53 pA). **b,** Medium-range zoom-in image, revealing a grid-like assembly. Bright round protrusions are assigned to Gd atoms. Less than 30% of nodes are not fully coordinated or decorated with residual gas ligands (V_{bias} = 0.5 V and I = 70 pA). **c-d,** High-resolution image and model of the assembly, revealing a 1 : 1 (2H-TPCN : Gd) stoichiometric ratio (Vb = 1 V and I = 67 pA). In **(d)** C, N, H, and Gd atoms are depicted in green, blue, white and brown, respectively. The square unit cell is shown in red, where b represents the unit vector and β the unit cell angle.

The adsorption orientation of the porphyrin units with respect to the close-packed directions of the substrate is identical in the non-coordinated and coordinated instances, highlighting the role of the surface. The Gd atoms span a square network with unit cell vector b = 24.5 ± 0.3 Å and a statistical analysis of Gd-NC distances show a projected average bond length of 2.7 ± 0.5 Å. These observations are in accordance to STM observations involving Gd atoms and dicarbonitrile polyphenyl organic ligands (Chapter 3).

The lack of metalation of the porphyrin macrocycle by Gd is tentatively assigned to a high activation barrier of the metalation together with a more difficult access of the Gd atoms to the tetrapyrrole pocket due to the bulky character of the TPCN species.

Furthermore, the shape of the porphyrin derivate restricts the coordination number to four, limiting a higher coordination, as the observed five-fold Ce/Gd-carbonitrile motifs on Ag(111)[40,41], by intermolecular steric hindrance. As a result of the four-fold coordination sphere of each Gd atom and the rigid nature of the four-fold geometry of the porphyrin molecules, a porous 2D supramolecular assembly is observed extending over the entire surface. This structural design employing lanthanide elements on surfaces and based on four-fold vertexes has only analogues in lanthanide crystal synthetic chemistry, where crystal structures can display two-dimensional four-fold reticulated sheets in *ab* planes[213].

Thus, after Gd-carbonitrile coordination, the macrocycle is kept protonated offering a chemical pocket to be metalated by additional metallic species.

5.2.2 Co : TPCN metalation and coordination networks

Next we inspect the propensity of TPCN species towards metalation and coordination with Co adatoms, since free-base tetraphenyl porphyrin undergoes fast metalation upon

exposure to Co at 300 K[214,215]. Following Co deposition on a submonolayer of TPCN on Ag(111) held at room temperature, a metalation of the tetrapyrrolic macrocycle could be selectively achieved. As depicted by Figures 5.6(a-b), at negative bias up to 70% of tetrapyrroles show a bright two-fold rod-like inner protrusion, whereas the rest of the macrocycles remain unperturbed (cf. Figure 5.6(c) for comparative height profile), which is in agreement with previous studies of Co metalation of free-base tetrapyrrolic species[210,211].

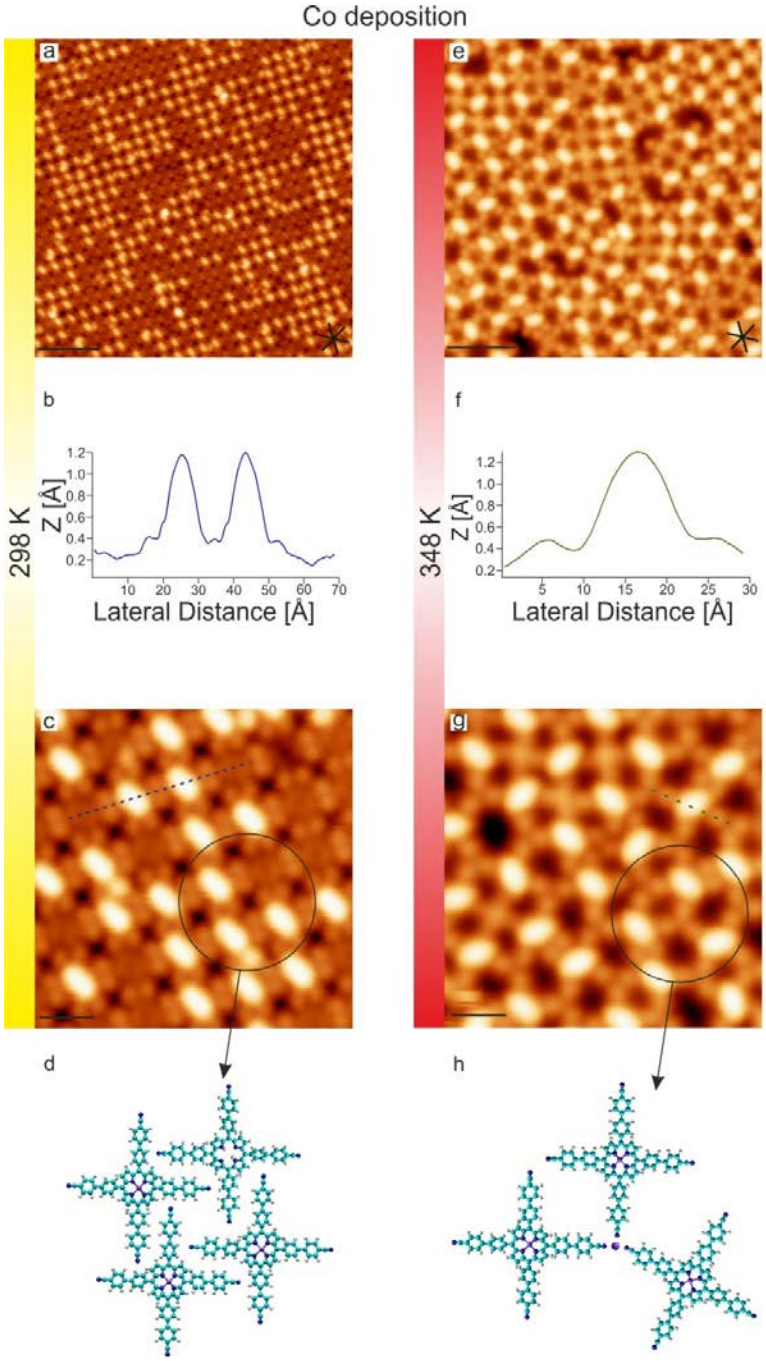

Figure 5 . 6 | T-dependent metalation and coordination of 2H-TPCN networks on Ag(111) by deposition of Co atoms

a, c, Room-temperature metalation of the porphyrins by Co deposition, which is identified by a rod-like appearance of the macrocycle. Tunneling parameters: **(a)** V_{bias} = -1 V and I = 200 pA; **(c)** V_{bias} = -1 V and I = 90 pA. **b,** Height profile along the purple dotted line in **c** showing different apparent heights for metalated and non-metalated tetrapyrroles. **d, f,** Large-scale resolution images and height profile exhibiting a disordered metalated and Co-carbonitrile coordinated network when the sample is annealed to 375 K. Tunneling parameters: **(d)** V_{bias} = -1 V and I = 300 pA, **(f)** V_{bias} = -1 V and I = 300 pA. For **(c)** and **(f)** superposition of atomistic models facilitates the identification of metalated and non-metalated macrocycles as well as the non-coordinated or coordinated terminal biphenylcarbonitrile groups. **e,** Height profile extracted along the green dotted line in **(f)** exhibiting a perfect match with the profile of the metalated species in **(b)**.

Only a very few cases of Co-NC coordination motifs are observed (less than 1%) at any Co coverage, revealing a selective preference for metalation to take place in the tetrapyrrolic cavity. This behavior is particularly remarkable as compared with the reported propensity of dicarbonitrile polyphenyl species to coordinate with Co at room temperature[14,79,80,216,217]. Furthermore, Co coordination resulted in the formation of very tiny patches at the border of the non-coordinated supramolecular assembly exhibiting three- and four-fold Co-carbonitrile coordination (see below). To investigate temperature-dependent structural changes the sample is annealed at temperatures form 298 to 348 K. At 348 K, a random metal-organic network is detected, in which three- and four-fold Co-carbonitrile motifs are coexisting at a 71% and 29% of occupancy respectively, as previously observed for dicarbonitrile polyphenyl species. The experimental projected Co-NC bond length is 2.0 ± 0.5 Å being 0.7 Å shorter than the average Gd-NC distance.

5.2.3 Orthogonal d-f heterobimetallic network

Taking advantage of the high affinity of the central free-base tetrapyrrolic core towards Co adatoms and the coordination with Gd at room temperature, heterobimetallic networks involving Gd-carbonitrile coordination and in-situ Co-metalated porphyrin species are fabricated. To this aim, Co atoms were evaporated onto a previously prepared Gd : 2H-TPCN sample held at room temperature.

Figure 5.7(a) shows high-resolution STM images of the heterobimetallic Gd-Co-TPCN assembly on Ag(111) acquired at positive bias (V_b = 1 V). As it clearly appears from the images, the four-fold coordination architecture is preserved and assigned to Gd-NC

coordination, while simultaneously the borders of the nanostructure exhibit a minority three-fold coordination attributed to Co-carbonitrile coordination (cf. below).

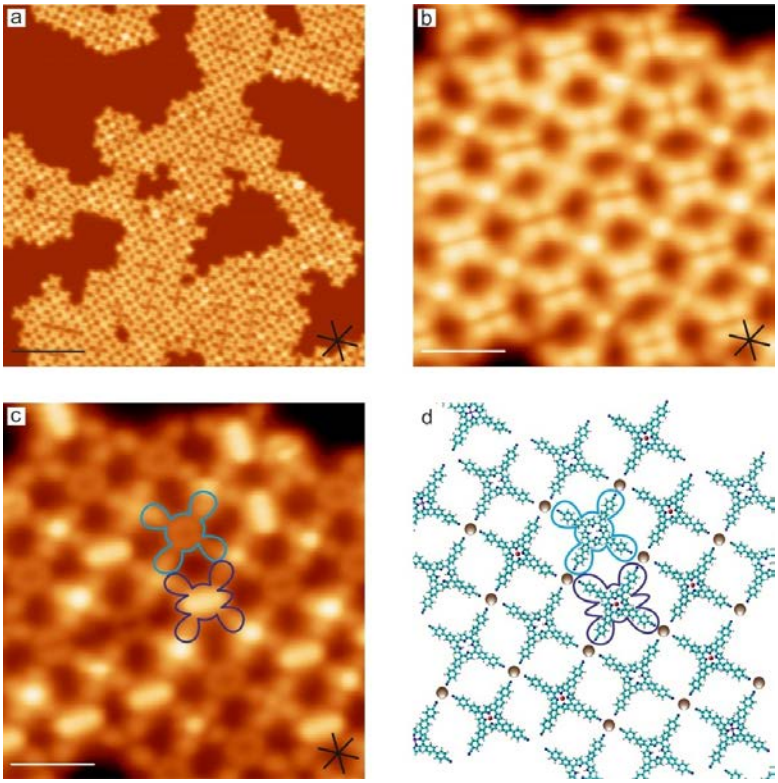

Figure 5 . 7 | Lanthanide-driven heterobimetallic porphyrin network

a, Overview STM image of the heterobimetallic network (V_b= 1 V and I = 100 pA). **b,** STM image recorded at V_b= 1 V (I = 75 pA) displays no different appearance between metalated and free-based porphyrins macrocycles, showing four bright lobes localized over the four mesa-bridge carbons. **c,** At low positive V_{bias} (V_b= 0.7 V and I = 75 pA) the four lobes for the non-metalated substituted porphyrins appear brighter than the metalated ones (the contours magenta and violet highlight the two mentioned porphyrin species).Gd atoms appear as circular bright protrusions independently the V_{bias} used. **d,** Ball-and-stick atomistic model of the assembly presented in **(c)**, herein C, N, H, Gd and Co atoms are depicted in green, blue, white, brown and purple respectively.

At V_b = 0.7 V imaging of the same area reveals the fingerprint of porphyrin metalation (cf. Figure 5.7(c)), which consists in the appearance of dimmer and brighter macrocycle shapes assigned to Co metalated and free-base porphyrin derivates, respectively. Importantly, these Co-metalated species are involved in the coordination, without any distortion of the grid-like assembly.

Regarding metal-organic coordination, Gd centers appear as bright protrusions regardless of the bias polarity. As previously reported for five-fold Gd-NC motifs, residual gas can be axially ligated to the Gd centers influencing its appearance. We discard that Co atoms are attached to the lanthanide vertexes for the following reasons: i) the aspect and size of the rare-earth centers is equivalent, within the heterogeneity, before and after Co deposition (cf. Figures 5.8(a,b)) and ii) no clustering is observed at the vertexes, thus maintaining the structure of the coordination network intact (cf. Figure 5.8(c)). The Gd-Gd distance is identical within the experimental precision for the metalated (35.1 ± 0.7 Å) and the non-metalated (34.5 ± 0.6 Å) species, and it is much different from the Co-Co distance (32.4 ± 1.0 Å), reflecting as expected the bigger size of the lanthanide atoms.

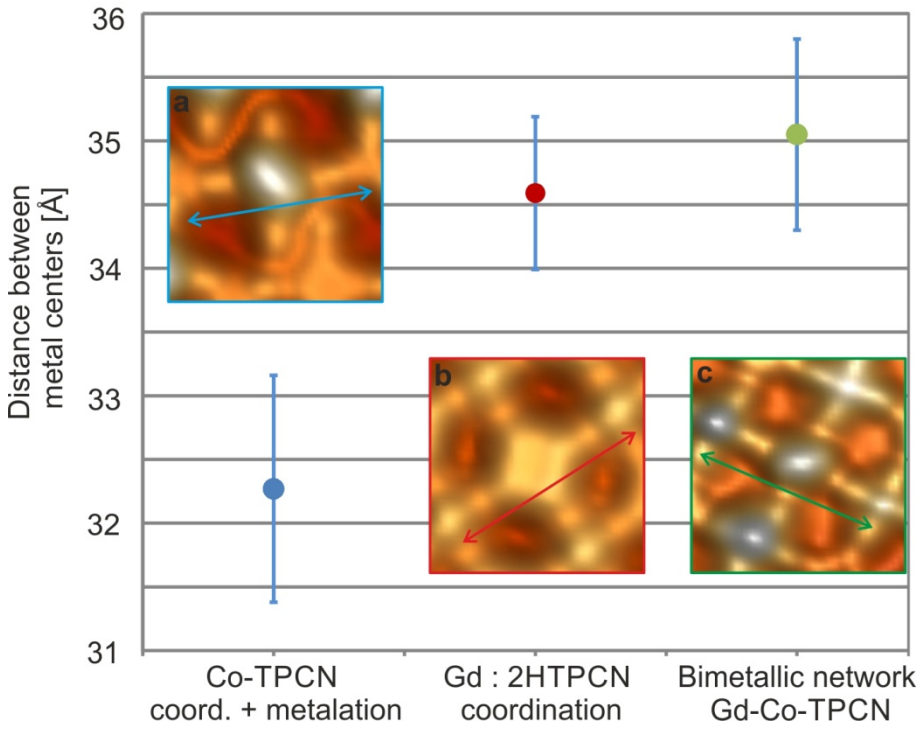

Figure 5 . 8 | Intermetallic distances of the distinct metallosupramolecular assemblies

The pure lanthanide metal-organic network (inset b) and the bimetallic one (inset c) exhibit a similar internodal distance, whereas the pure Co metal-organic structure presents a clearly shorter value (inset a). STM images **(a-c)** are presented in a 3D fashion. The blue line depicts the Co-molecule-Co distance, whereas the red and green show the Gd-molecule-Gd value for the pure lanthanide assembly and the bimetallic one, respectively. Internodal distances of **(b)** and **(c)** are in agreement with the Fast Fourier Transform of long range images.

5.3 Conclusion

In summary, by exploiting orthogonal coordination interactions, we have successfully designed a surface-confined d-f heterobimetallic supramolecular nanoarchitecture, consisting of a grid-like four-fold Gd-carbonitrile coordinated network of in-situ Co metalated porphyrin derivates on Ag(111). To this aim, a three-step self-assembly protocol is employed. First, the deposition on Ag(111) of a free-base porphyrin species (2H-TBPCNP), peripherally equipped with terminal carbonitrile functional groups to steer coordinative schemes, results in a tetragonal close-packed assembly stabilized by N···H interactions. A subsequent incorporation of Gd atoms gives rise to a grid-like nanoarchitecture based on four-fold Gd-carbonitrile coordination vertexes, without any sign of metalation. Finally, the deposition of Co atoms results in the efficient metalation of the central pyrrolic macrocycle, maintaining intact the porous Gd-coordinated network, thus forming a supramolecular d-f nanosystem.

This is the first in vacuo realization of a 2D lanthanide-transition metal heterostructure exploiting the advantages of selective metal-organic coordination of a molecular species towards coordination and metalation. This protocol can anticipated possible new avenues to molecular design on surfaces, propelling the development of d-f nanosystems, with potential impact for engineering magneto responsive or, light emitting devices for sensing and single-molecule catalytic applications.

In the next chapter we change the functional group of the molecular building block, i.e. carboxylates instead of the carbonitrile groups employed in chapters 3, 4 and 5 in order to explore the Gd-carboxylate interactions on the Ag(111) and Cu(111) surfaces.

6. Lanthanide (Gd)-carboxylate coordination on surfaces

MOCNs that comprise carboxylate functional groups and transition metal elements as metallic nodes have been intensely studied in the last few years combining advantages of both homogeneous and heterogeneous catalysis[218,219] and being proved to be suitable as robust and adaptable templates for the organization of guest species.

On the one hand, specific intermolecular interactions, i.e. van der Waals forces, hydrogen bonds or metal coordination have been employed to connect constituting building blocks. In recent times, ionic self-assembly (process that uses electrostatic interactions between oppositely charged molecules/atoms as the dominant interaction) has been developed as a potent tool for the fabrication of novel nanoarchitectures with exclusive chemical and structural properties[220-223]. In this sense, carboxylic moieties were chosen due to their easily donation of the carboxylic hydrogen giving rise to their anionic homologous.

On the other hand, Considerable efforts were devoted to explore novel coordination architectures with cyano endgroups incorporating lanthanides (chapters 3-5), typically providing high coordination numbers that give rise to unusual topologies as also encountered in bulk chemistry[224-231]. In this manner the interaction between carboxylate endgroups and lanthanide elements should be explored at surfaces in order to study similarities and differences among the lanthanide-organic coordination with distinct functional groups.

LT-STM and VT-STM experiments realized in this chapter were carried out at TUM and in collaboration with IMDEA Nanoscience (Madrid, Spain) under the supervision of Dr. David Ecija. DFT simulations were performed by Professor Fernando Martin´s group at UAM, Spain.

6.1 Deposition of TDA and TDA + Gd on Ag(111)

4,1′,4′,1′′-terphenyl-1,4′′-dicarboxylic acid (TDA, synthesized by a Pd-catalyzed Suzuki coupling[232]) is deposited at room temperature onto a smooth Ag(111) substrate giving

rise to a close-packed ordered arrangement (Figure 6.1), where molecular species are visualized as rods. An atomistic model reveals that the self-assembly is stabilized by O···H interactions, as previously described for molecular species functionalized with carboxylic endgroups[17,233].

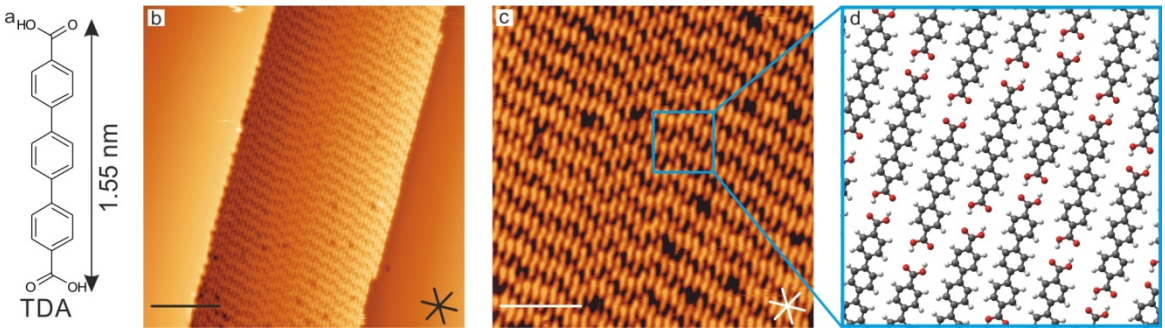

Figure 6 . 1 | Chemical structure and LT-STM topographs of TDA species deposited at room temperature on Ag(111)

a, Molecular structure of TDA. **b,** LT-STM image showing the tetragonal supramolecular network stabilized by H-bond interactions (V_b = 1 V and I = 80 pA). Scale bar: 10 nm. **c,** Low-temperature STM image that allows to discern the individual entities as bright rods (V_b = 1 V and I = 80 pA). Scale bar: 5 nm. **d,** Atomistic model of **(c)** revealing that the network is stabilized by directional H-bonding. C, O and H atoms are depicted in grey, red and white, respectively.

After annealing the sample to slightly higher temperatures (375 - 450 K) molecular species are desorbed from the Ag(111) surface and the observation of the anionic species (TDA^{2-}) is not achieved.

In order to check the affinity of the carboxylic groups to lanthanide elements, gadolinium atoms are deposited at room temperature onto a Ag(111) surface containing TDA species. A new scenario emerges, where big islands formed by intact TDA species coexist with irregular metallosupramolecular networks (cf. Figure 6.2). A closer look reveals that the new structures are based on a four-fold metal-organic interaction. We assign this coordination to the link between Gd centers and carboxylate derivates (TDA^{2-}), with a Gd : linker stoichiometry of 1 : 2 and a projected average Gd-O bond length of 2.5 ± 0.8 Å, coexisting at the temperature of sample growth with TDA molecules. Thus, the growth of ordered Gd-directed metallosupramolecular architectures based on TDA linkers on Ag(111) is cumbersome: i) on one hand at room temperature, after Gd deposition, there is a competition between carboxylate and carboxylic species

(majority), resulting only in minority disordered metal-organic networks; ii) on the other hand, annealing the sample at higher temperatures to promote carboxylate moieties results in the desorption of the TDA species.

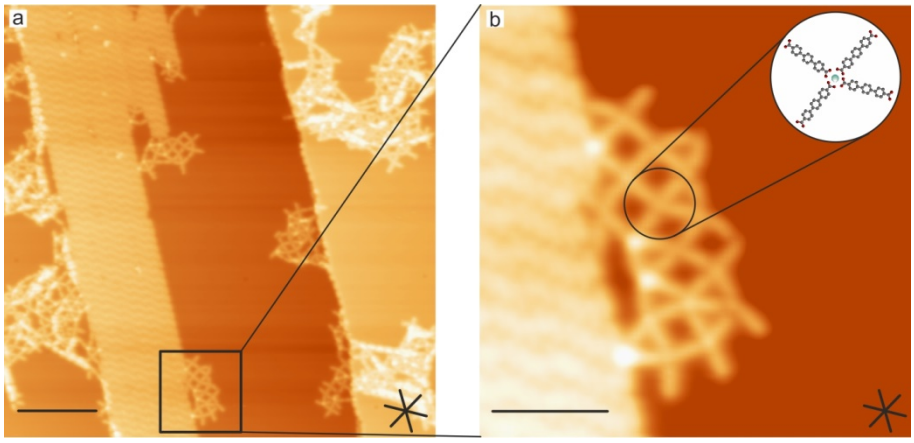

Figure 6 . 2 | LT-STM topographs of disordered Gd : carboxylate assemblies deposited at room temperature on Ag(111)

a, LT-STM image showing disorganized Gd : TDA assemblies coexisting with TDA molecular islands. (V_b = 1 V and I = 87 pA). Scale bar: 15 nm. **b,** Zoom-in STM image of **(a)** that allows to discern small patches of the Gd : carboxylate molecular assembly (V_b = 1 V and I = 87 pA). The inset shows an atomistic model of a the four-fold metal-organic interaction. C, O and Gd atoms are depicted in grey, red and light green, respectively. Scale bar: 5 nm.

6.2 Deposition of TDA on Cu(111)

The deposition of TDA on bare Cu(111) at room temperature gives rise to close-packed arrays, in which the molecular species are visualized as rods, featuring an oblique lattice, with unit cell vectors of 8.2 ± 0.7 Å and 18.7 ± 0.7 Å, spanning an angle of 55° (cf. Figure 6.3(b)). Importantly, at this temperature, the molecular species preserve its integrity, allowing high diffusion and the formation of networks stabilized by O···H intermolecular interactions. (cf. Figure 6.3(c)).

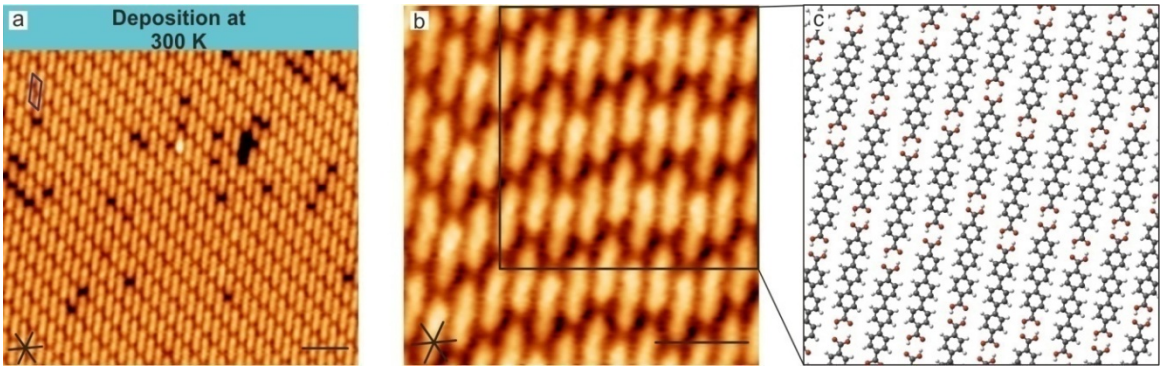

Figure 6 . 3 | Dense-packed assembly of TDA on Cu(111) after deposition at RT

a, LT-STM image showing the tetragonal supramolecular network stabilized by H-bond interactions (V_b = -1 V and I = 400 pA). The violet tetragon depicts the unit cell. Scale bar: 3 nm. **b,** Low-temperature STM image that allows to discern the individual entities as bright rods (V_b = 0.1 V and I = 200 pA). Scale bar: 2 nm. **c,** Atomistic model of **(b)** revealing that the network is stabilized by directional H-bonding. C, O and H atoms are depicted in grey, red and white, respectively.

At slightly higher substrate temperatures (308 K), variable-temperature STM reveals the appearance of mainly isolated rod-like species, associated with deprotonated compounds[234], coexisting with rarely appearing unaltered TDA islands. Above this substrate temperature, only carboxylate moieties (TDA^{2-}) appear for low-temperature visualization (cf. Figure 6.4). A detailed analysis of the STM data shown in Figure 6.4(b) reveals the appearance of individual TDA^{2-} molecules, imaged as extended rod-like shape, where the long molecular axes are aligned 45° with respect the three high-symmetry directions of the Cu(111). Remarkably two major depressions positioned at the long molecular axes peripheries are observed (inset Figure 6.4(b)). This phenomena, associated with the oxygen-terminated molecular extremity, is related to the strong reactivity of the carboxylic group upon adsorption on Cu surfaces[85,86,235-241].

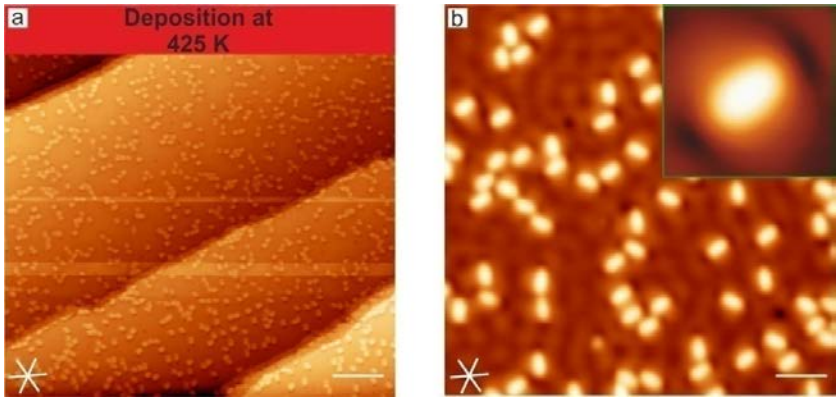

Figure 6 . 4 | Dense-packed assembly of TDA on Cu(111) after deposition at 425 K

a, Long range LT-STM image of individual TDA molecules after annealing the substrate (V_b= 0.1 V and I = 200 pA). Scale bar: 12 nm. **b,** High-resolution LT-STM image of **(a)**. The green marked inset shows an individual molecule with two major depressions at the long molecular axe sides. (V_b= 0.1 V and I = 200 pA). Scale bar: 3 nm.

6.3 TDA + Gd on Cu(111)

In order to assess the affinity of the carboxylate groups to lanthanide elements, gadolinium is deposited onto a Cu(111) surface containing TDA^{2-} molecules and held at ≈ 423 K.

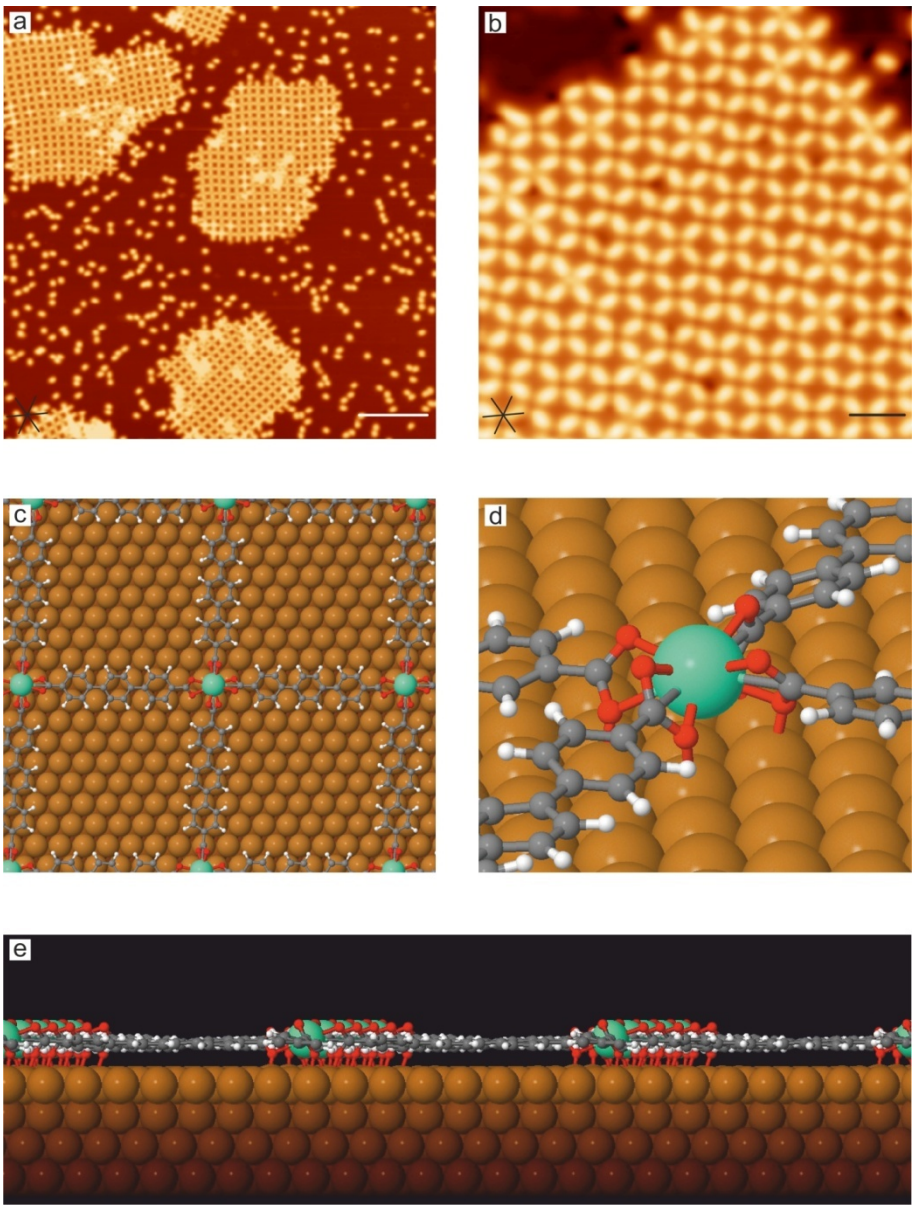

Figure 6 . 5 | Lanthanide-directed Gd : carboxylate supramolecular network on Cu(111)

a, Long-range topograph (V_b = 1 V and I = 80 pA). Scale bar: 15 nm. **b,** High-resolution image (V_b = -1 V and I = 300 pA). Scale bar: 3 nm. **c-e,** DFT optimized geometry of the assembly. **c,** Top-view. **d,** Zoom-in perspective view emphasizing the 8-fold Gd-O coordination motif. **e,** Side-view. Gd, C, O, H, and Cu atoms are depicted in light green, grey, red, white, and orange, respectively.

Following this protocol, Figure 6.5(a) depicts the formation of extended patches of 2D reticulated supramolecular structures, coexisting with isolated carboxylate molecular species. High-resolution imaging allows us to discern the network architecture, which features a square unit cell of 19.5 ± 0.7 Å, with a Gd : molecular linker stoichiometry of 1 : 2 (cf. Figure 6.5(b)). Hereby, molecular species are visualized as rods, and Gd centers as voids (cf. Figure 6.5(a,b)) or dim protrusions (cf. Figure 6.7) depending on the employed tunneling conditions and tip state. The mononuclear Gd vertexes are surrounded by four molecular linkers, reflecting a square-planar coordination motif with four chelating rare-earth-carboxylate bonds and a projected average Gd-O bond length of 2.6 ± 0.7 Å (cf. below). This coupling scheme resulting in a coordination number of 8 is unprecedented for interfacial metallosupramolecular architectures and hints towards a prevalent ionic character versus covalency in the lanthanide metal-organic bonds, also encountered in bulk chemistry[242].

To further rationalize the Gd-carboxylate supramolecular network, we got support from DFT simulations. Figures 6.5(c-e) illustrate an optimized geometry of the assembly, highlighting the eight-fold Gd-O lateral coordination and yielding a binding energy of 4.99 eV/molecule (for comparison in the absence of the substrate this binding energy is 3.27 eV/molecule). Molecules are adsorbed with their polyphenylene backbone almost planar. The average interphenylene dihedral angle is 10.9°, i.e. individual rings are oriented approximately ± 5° with respect to the surface plane. The planarization of the molecular linkers is then similar to that encountered for the surface-confined five-fold metal-organic assemblies based on Ce(Gd) and *p*-NC-$(Ph)_{3,4}$-CN-*p* species.[40-42]

Remarkably, Gd atoms present an adsorption height of 3.1 Å with respect to the surface (cf. Figure 6.5(e)). In order to balance Gd-O attractive interactions and intermolecular O···O steric hindrance, the carboxylate termini rotate 44.5° about their sigma bonds, thus allowing the high coordination number of 8, with a Gd-O bond length of 2.4-2.7 Å, in accordance with the experimental geometry and similar values reported for 3D lanthanide-oxygen donor complexes.[243] This 8-fold Gd-O lateral coordination motif

differs from the coordination nodes in the related nanoporous Fe and Co-terephthalate arrays fabricated on Cu(100) or Au(111), which incorporate four lateral carboxylate bonds to dimetal centers[244,245]. We attribute the distinct coordinative scheme to the larger atomic diameter of the Gd center and the propensity of rare-earth metals towards higher coordination numbers.

Additional information regarding the electronic structure of the coupling motif is provided by the evaluation of the DFT results. First, the Bader analysis shows a positive charge of +2.1e for Gd and a negative charge of -1.1e for each of the eight surrounding oxygens involved in the coordination, which results in a total charge of -0.89e for the metal-organic assembly. These results indicate cationic Gd centers in the metallosupramolecular layers[239]. Second, we analyze the electron density displacement field[246] of the Gd-$(TPA)_4$ adlayer (cf. Figure 6.6). The field reveals black depletion zones around the Gd center, indicating a strong ionic component in the Gd-$(TPA)_4$ coordinative scheme, similar to the Cs-$(TCNQ)_4$ system, where ionic interactions are deduced.[246]

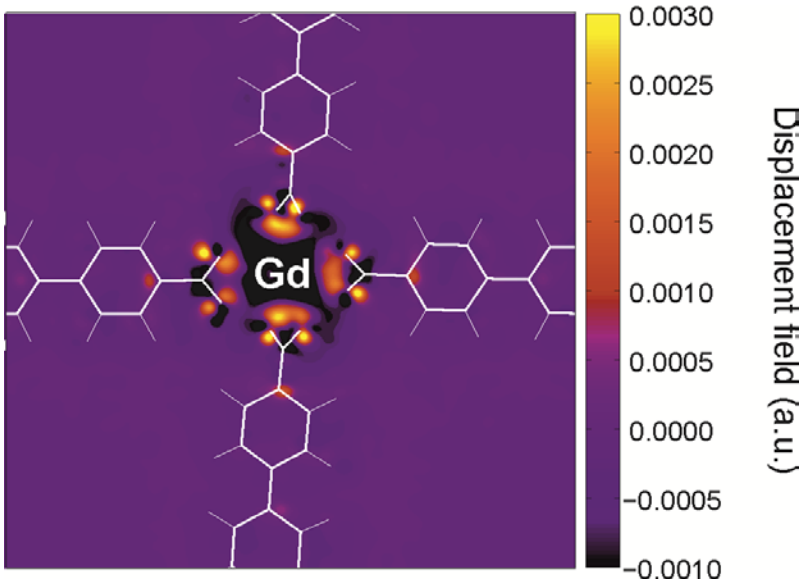

Figure 6 . 6 | Charge-density displacement field of the Gd-TPA_4 node on the Cu(111) surface

The plot illustrates the difference between electron charge density of the interacting system and those of its non-interacting components. Negative values (violet, black) represent charge depletion, accounting for an ionic character of the Gd center. Positive values (yellow, orange, red) indicate charge accumulation, highlighting the charge gained by the carboxylate moieties. The structure model is superimposed.

Importantly, there is only a single rare-earth center in the four-fold coordination node. More complex nodes such as the previously encountered dinuclear Co or Fe motifs in

carboxylate-based metal-organic networks, or the recently suggested di-iron-nodes in upright positions coordinated by pyridil moieties are excluded in the gadolinium-directed four-fold reticulated architecture, because the rare-earth atomic diameter is too large for the nodal space and Cu adatoms did not participate in coordination schemes in the explored range of temperatures. Nevertheless a few dinuclear centers comprising a six-fold node are found as shown in Figure 6.7.

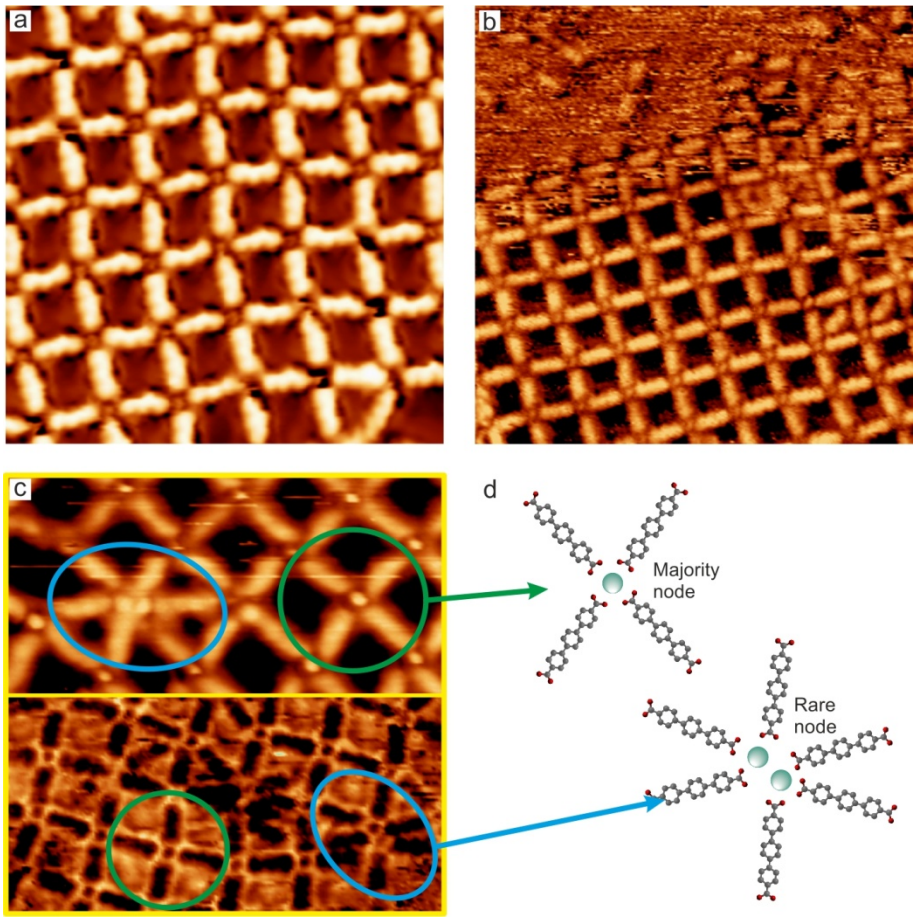

Figure 6 . 7 | Nature of the coordination nodes

a-b, High resolution STM images of the reticulated network showing one Gd atom per node. **a,** V_{bias} = -1 V, measured at 6 K. **b,** V_{bias} = 0.8 V, imaged at room temperature. **c,** High resolution STM images revealing the majority mononuclear Gd nodes and statistically very infrequent binding motifs comprising two Gd atoms and six molecular species. V_{bias} = 0.8 V, measured at room temperature. Bottom panel is shown with inverted contrast to emphasize the Gd nodes. **d,** Atomistic models of the two distinct binding motifs. Carbon, oxygen and gadolinium atoms are depicted as grey, red and green, respectively.

The Cu(111) surface is also expected to play an appreciable role in the formation of the lanthanide-carboxylate networks. TDA^{2-} species and Gd-carboxylate networks were exposed to a CO dosage (≈ 75 s at 1×10^{-7}mbar) to elucidate the molecular registry on the

surface, due to the well-known adsorption of CO molecular species on Cu(111), which are place in an upright configuration on top sites[111]. Up to this exposure, no significant changes in the molecular species or the Gd centers were detected; however CO molecules were visualized as round indentations absorbed on the surface (cf. Figure 6.8(a,b)). Based on this premise, the atomistic model presented in Figures 6.8(c,d) shows how the three phenyl rings of the TDA^{2-} species were placed on the bridge positions of the Cu(111) surface. For Gd-carboxylate networks, lanthanide atoms were also found to be positioned on the bridge positions while coordinated molecular species adapted their location with respect to the Cu(111) surface in order to form the Gd-carboxylate coordination network as shown in Figure 6.8 (d).

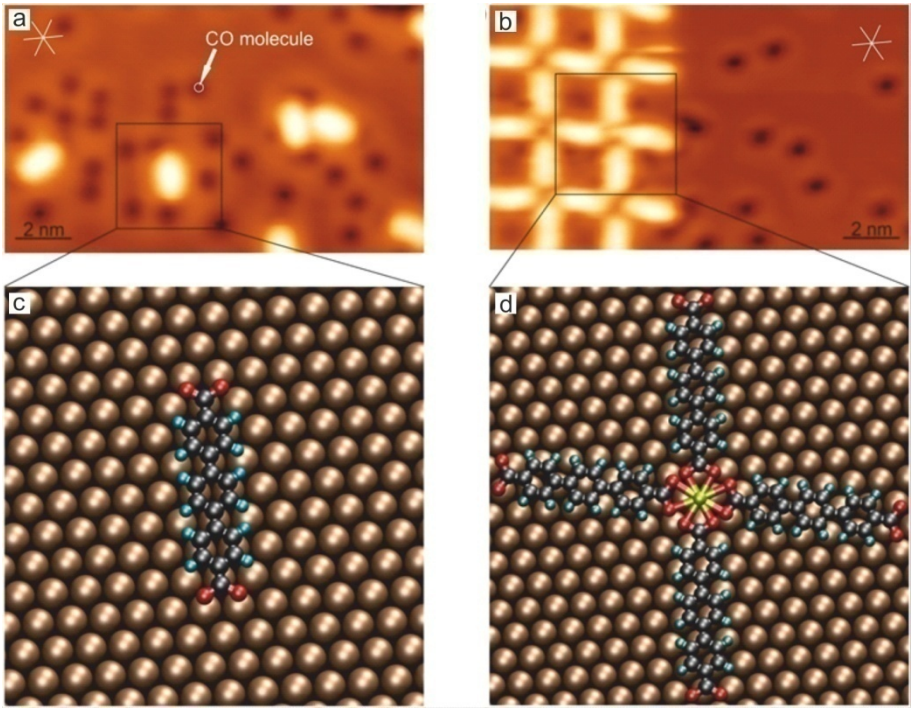

Figure 6 . 8 | LT-STM images and atomistic model of TDA^{2-} species and Gd-carboxylate network after exposure to CO gas at 6 K

a, High-resolution LT-STM image of individual TDA molecules after CO deposition (V_b= 0.5 V and I = 150 pA). Black nodes are assigned to single CO molecules placed in an upright configuration on top sites. **b,** High-resolution LT-STM image of the Lanthanide-directed Gd : carboxylate supramolecular network after CO deposition(V_b= 0.4 V and I = 160 pA). **c-d,** Zoom-in atomistic models of **(a-b)** showing how the atoms are placed on the Cu(111) surface. Copper, carbon, oxygen, hydrogen and gadolinium atoms are depicted in brown, black, red, light blue and yellow, respectively.

Next, we have explored the thermal stability of the Gd-carboxylate nanoarchitectures by holding the sample at distinct temperatures during STM-measurements. Continuous imaging at 77 K, RT and at 360 K exhibits stable island edges and identical assemblies to those achieved at 6 K (cf. Figure 6.9), highlighting an appreciable thermal robustness, also encountered in surface-confined metal-carboxylate networks involving alkali or d-block centers[87,247-249]. Importantly, the variable-temperature imaging shows certain degree of flexibility of the coordination nodes, which could be of relevance for hosting[87] functional guest species. Further inspection at 393 K (the technical limit for the variable-temperature STM) signals the initial steps of disintegration of edges of the assemblies.

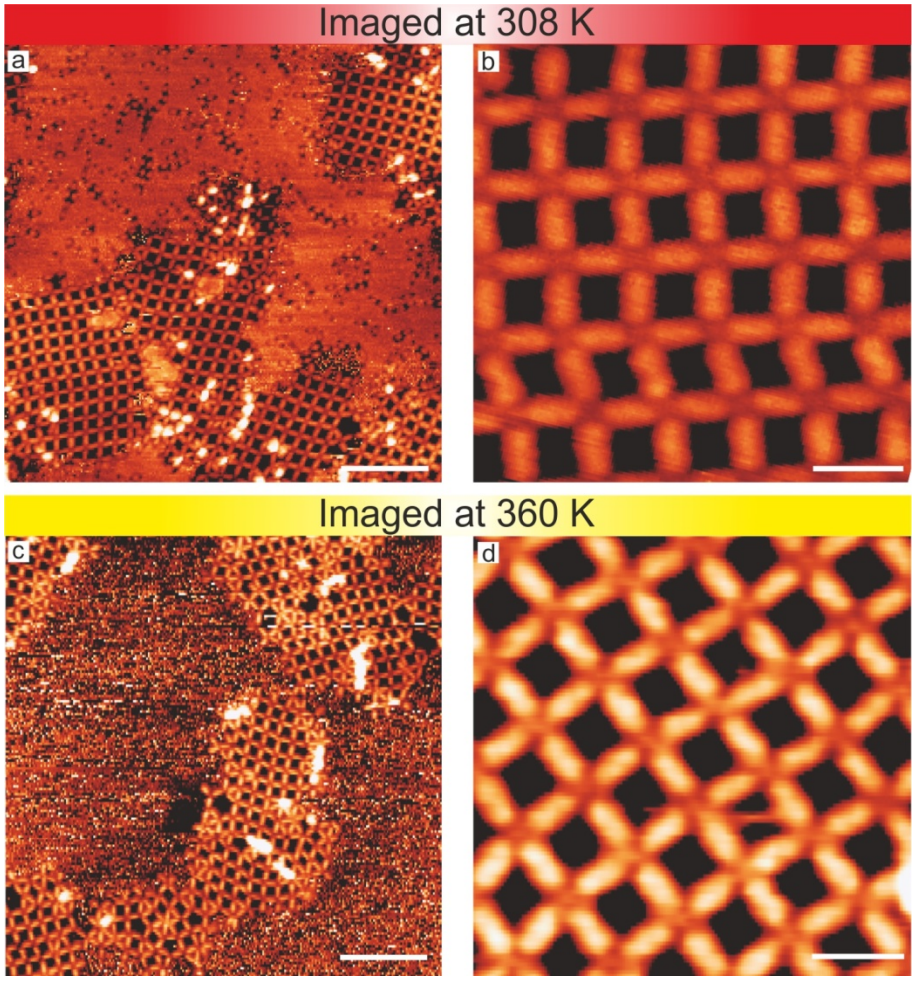

Figure 6 . 9 | Variable-temperature STM images of the Gd-TDA supramolecular assembly on Cu(111) recorded at 308 K and 360 K

a, Long-scale image (V_b = 1.3 V and I = 500 pA, scale bar = 10 nm). **b,** High-resolution STM image (V_b = 1.3 V and I = 480 pA, scale bar = 2 nm). **c,** Large-range STM image highlighting the stability of the islands at high-temperature (V_b = 1.1 V and I = 370 pA, scale bar = 10 nm). **d,** High-resolution STM image (V_b = 1.6 V and I = 400 pA, scale bar = 2nm).

6.4 Conclusion

In summary, we have presented a multi-technique study combining low-temperature STM, variable-temperature STM and DFT simulations introducing the gadolinium-directed assembly of 2D coordination networks on Cu(111) by exploiting metal-ligand interactions between TDA^{2-} species and gadolinium centers.

Our data and analysis give insights into the detailed geometry and electronic nature of the lanthanide-carboxylate bond on metallic surfaces, notably indicating chelating arrangements with ionic characteristics. Thanks to the unprecedented coordination number of 8 for the Gd vertexes and the bonding strength, the assemblies are thermally robust. Taking into account the feasibility of incorporating distinct lanthanide elements in similar coordination environments,[41] our study opens novel avenues towards manifold robust rare-earth-carboxylate nanoarchitectures featuring specific functionalities provided from the selected lanthanide and linkers.

7. General conclusions and perspectives

The work presented in this thesis introduces lanthanides as unique elements to design metallosupramolecular architectures on noble metal surfaces. For the first time, the use of organic molecules with specific functional groups, i.e. carbonitrile and carboxylate moieties as molecular building blocks and its coordination with lanthanide elements has been reported. Scanning tunneling microscopy represents a surface sensitive technique that provides the possibility of imaging and manipulate matter at the atomic level. Therefore, two-dimensional lanthanide metal-organic networks have been inspected taking advantage of this tecnique. Moreover, further investigations enclosing f-block elements as well as the use of complementary techniques are necessary to study their electronic and magnetic properties that can be of capital relevance in photonics, sensing, catalysis or spin-orbit materials.

In this work, the interaction between lanthanide elements as cerium (Ce), gadolinium (Gd) or europium (Eu) and carbonitrile (*p*-NC-Ph_3-CN-*p*, *p*-NC-Ph_4-CN-*p* and TPCN) or carboxylate (TDA^{2-}) functionalized molecular species absorbed on gold, silver and copper surfaces is investigated.

In particular, the co-deposition, under specific stoichiometric conditions of Ce/Gd atoms and *p*-NC-$Ph_{3,4}$-CN-*p* species absorbed on the Ag(111) surface gives rise to lanthanide-based metal-organic networks (α, β and γ phases) where five-fold planar coordination nodes prevail. This spontaneous expression of five-fold coordination is attributed to the particular electronic configuration of lanthanides. They possess larger ionic radius and smaller ligand-field effects than transition metals (d-block elements), and their coordination chemistry is governed by the geometrical arrangements and steric effect of the employed molecular linkers. Especially interesting is the presence of phase γ which represents the first observation, based on metal-organic interactions, of a snub square Archimedean tiling. Furthermore, taking advantage of the lateral manipulation procedure, the control and manipulation of Gd(*p*-NC-Ph_4-CN-*p*)$_5$ supramolecules is achieved highlighting the relatively strong lanthanide : molecular linker interaction.

In order to compare the chemical similarities and/or differences between Eu and Ce/Gd coordination networks, Eu and *p*-NC-Ph_4-CN-*p* species are co-deposited and studied at RT on the Ag(111) surface. Herein, four-fold and five-fold coordination networks are observed under precise stoichiometric conditions, in contrast to previous experiments with Ce/Gd, where five-fold coordination nodes prevail independently of the lanthanide : molecular linker stoichiometric ratio. Thus, the europium coordination sphere can be adapted to several coordination numbers according to preparation conditions. Co-deposition of Eu and *p*-NC-Ph_4-CN-*p* species at RT onto the Au(111) surface presents a different scenario, demonstrating the influence of the adlayer/substrate interactions. As a result, an increased adaptivity of the coordination motifs is detected due to the weaker surface interactions for Au(111) in comparison with the Ag(111) surface. Importantly, for a specific 2 : 5.1 (Eu : *p*-NC-Ph_4-CN-*p*) stoichiometry, a novel metal-organic network based on four-, five- and six-fold coordination nodes and featuring random-tiling dodecagonal quasicrystalline network characteristics is observed. Its appearance is tentatively associated to the flexible Eu coordination and the balance between enthalpy and entropy as a key parameter for random-tiling quasiperiodicity.

The distinct reactivity of a porphyrin derivate (2H-TPCN) towards Gd and Co atoms on a bare Ag(111) surface is also inspected. After Gd deposition onto a 2H-TPCN molecular close-packed tetragonal assembly a four-fold coordination network emerges. This network is stabilized by the interaction between Gd and the terminal carbonitrile groups of the porphyrin derivate, following a 1 : 1 (Gd : 2H-TPCN) stoichiometric ratio and importantly, no metalation of the porphyrin chemical pocket is observed. On the one hand, the absence of five-fold coordination nodes (like in the Ce/Gd : *p*-NC-$Ph_{3,4}$-CN-*p* systems) is attributed to steric impediments in the porphyrin backbone. On the other hand, the lack of metalation is tentatively assigned to a high activation barrier of the metalation together with a more difficult access of the Gd atoms to the tetrapyrrole macrocycle. Consequently, taking advantage of the lack of metalation by Gd atoms of the porphyrin derivate, Co atoms are deposited onto the Gd : 2H-TPCN network. Accordingly, a d(Co)-f(Gd) heterobimetallic network comprising Gd-carbonitrile coordination and in-situ Co-metalated porphyrin species is achieved.

Finally, carboxylate ligands are among the most frequently employed ligands in 4f coordination chemistry due to the highly oxophilic nature of lanthanide ions. Thus, TDA^{2-} species, equipped with dicarboxylate functional groups are employed as molecular building blocks in its coordination with Gd atoms on the Cu(111) surface. Herein, a squared supramolecular network with a Gd : molecular linker stoichiometry of 1 : 2 is recognized. Notably, eight oxygen atoms are coordinated to the Gd node which is only possible due to the rotation of the carboxylate moiety at the surface. This fact reveals the ability of the carboxylate ligand to adopt different coordination modes, in comparison with previous studies of transition metal atoms and TDA molecules. In addition, the ionic character and the thermal stability of the network have been also investigated, highlighting the robustness of the Gd : carboxylate interaction.

These results demonstrated the rich variety of lanthanides and organic molecules interactions observed on noble metal surfaces. The lanthanide : molecular linker interactions give rise to different metal-organic architectures whose structural properties have been studied through the scanning tunneling microscopy technique. Nevertheless, complementary techniques, i.e. XPS or XMCD, should be used to get a higher insight in the intricate electronic and magnetic properties of such systems.

Future experiments could aim to the exploration of:

- The interaction of the same lanthanide elements with other organic functional groups on noble metal surfaces. Herein, the goal would be to investigate the different metal-organic nanoarchitectures systematically characterized by the STM.
- The interaction of different lanthanide elements with the same organic functional groups on the same noble metal surfaces. In this regard, the target would be to explore the chemical properties of the lanthanide series. Particularly interesting would be the presence or absence of quasicrystalline structures as other lanthanides, different from Eu, are employed in the lanthanide metal-organic network formation.
- Ligation of gaseous molecules, as CO or O_2, to lanthanide metal-organic architectures could be studied on different substrates in order to examine

the influence of the chemical environment of the lanthanide nodes on the binding affinity.

- Growth of lanthanide metal-organic architectures on atomically thin sheets of sp^2-hybridized boron nitride (BN) or graphene featuring structural, electronic and magnetic properties unachievable on metallic surfaces.

8. Appendix

8.1 Spectroscopic characterization of lanthanide-carbonitrile ligand networks by low-temperature STM

The interface established between metal atoms and organic molecules in terms of geometry and electronic configuration[250] plays an important role for optical, electrical and magnetic properties applicable in many fields such as organic solar cells[251,252], organic light-emitting diodes or field effect transistors[253,254]. This interface defines the metal-organic coupling strength and can modify the alignment of the organic molecular orbitals (MOs) due to the molecular interaction with single atoms or atom clusters[117,134,250,255-257]. In the last years, several spectroscopic studies regarding predefined metal-organic structures using transition metals as metal nodes were carried out onto metallic surfaces[256-259] as well as on insulating films[260] which has allowed detailed information on the molecular orbitals of different metal-organic complexes giving direct information about their physic-chemical properties at a fundamental level.

In the following, a brief approach to the spectroscopic characterization of lanthanide-directed (Ce/Gd) metal-organic networks using carbonitrile functional groups on a bare Ag(111) surface is shown. For comparison, a system where a transition metal (Co) is used as the metal node in the metal-carbonitrile network is also inspected.

- **Ce + *p*-NC-Ph$_n$-NC-*p* (n = 3,4)**

Figure 8.1 (a-b) shows representative STM images of pentameric units (phase α, Ce (*p*-NC-Ph$_{3,4}$-CN-*p*)$_5$, chapter 3) formed by employing Ce and *p*-NC-Ph$_3$-CN-*p* or *p*-NC-Ph$_4$-CN-*p* organic molecules, respectively. Scanning tunneling spectroscopy (STS) measured on non-coordinated *p*-NC-Ph$_{3,4}$-NC-*p* molecules (red curves) only show a delocalized resonance peak, which is tentatively assigned to the lowest unoccupied molecular orbital (LUMO), located at 1.28 V for *p*-NC-Ph$_3$-NC-*p* molecules and 1.37 V for *p*-NC-Ph$_4$-NC-*p* molecules. Figure 9.1 (c-d) shows the electronic characterization of Ce(*p*-NC-Ph$_{3,4}$-

NC-*p*)$_5$ units which present a strong localization of the molecular orbitals due to the influence of the Ce coordination:

i) The electronic structure of *p*-NC-Ph$_3$-CN-*p* linkers is modified upon coordination with cerium (Figure 8.1 (c)). Spectra acquired at the non-coordinated border of one linker to the Ce center in equidistant steps reveals two peaks in the molecular backbone (at 0.72 V and at 1.07 V), whose relative intensity depends on the proximity of the point of spectra acquisition to the Ce atom. Importantly, STS of the Cerium node only reveals a peak at 0.72 V. Thus, we rationalized the longitudinal evolution of the electronic structure as a downshift from 1.28 V to 1.07 V in the LUMO of the molecular linker upon coordination and the emergence of a new peak due to the presence of the cerium atom.

ii) A similar behavior is observed in *p*-NC-Ph$_4$-CN-*p* linkers upon coordination with cerium (Figure 8.1 (d)). The non-coordinated extremity of a coordinated *p*-NC-Ph$_4$-CN-*p* molecule shows two peaks at 0.78 V and 1.11 V, whose relative intensity is again modulated depending on the proximity of the point of spectra acquisition to the Ce atom. The Ce node presents a peak at 0.78 V. Thus, the downshift from 1.37 V to 1.11 V in the LUMO of the molecular linker upon coordination and the presence of a new peak at 1.11 V are again attributed to the coordination with the cerium atom.

No information regarding the highest occupied molecular orbital (HOMO) is observed in our STS data.

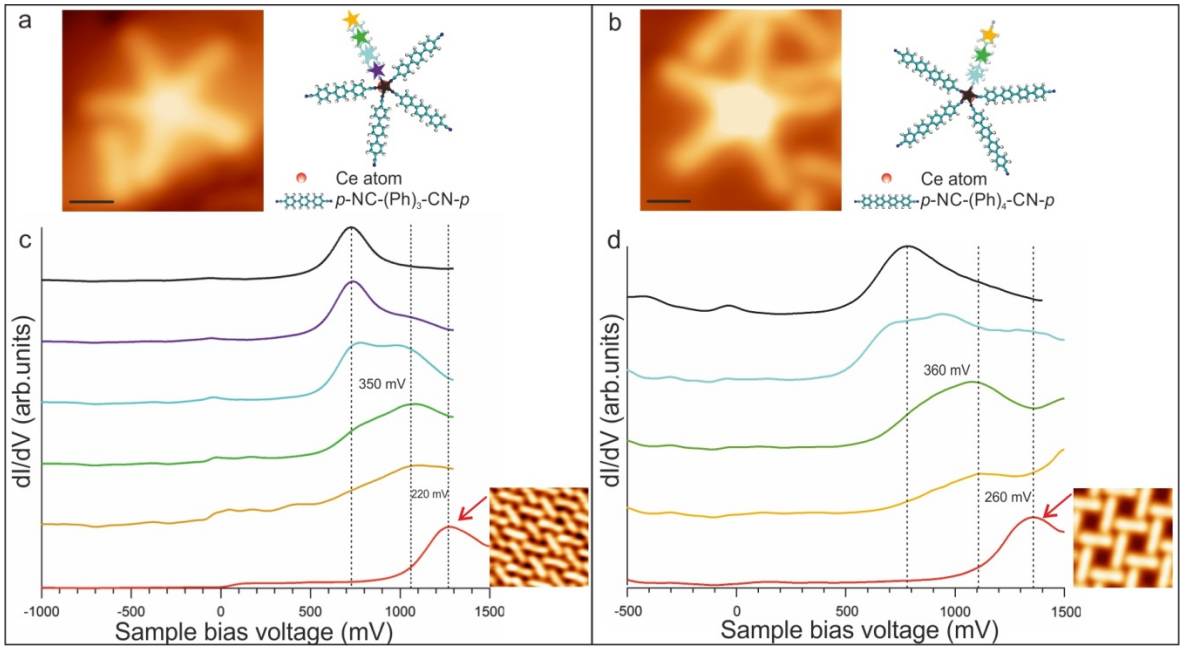

Figure 8 . 1 | Spectroscopic characterization of Ce(*p*-NC-Ph$_{3,4}$-CN-*p*)$_5$ supramolecules

a-b, High-resolution STM images and atomistic models of a Ce(*p*-NC-Ph$_3$-CN-*p*)$_5$ and a Ce(*p*-NC-Ph$_4$-CN-*p*)$_5$ supramolecule, respectively. The colored stars indicate the points where the STS data have been measured. Scanning parameters: V_b = 0.2 V, I = 100 pA. Scale bar: 1 nm. **c-d,** Spatially resolved spectroscopic data reveal the downshift phenomena in the molecular frontier orbital energy. The different colors of the STS curves are in agreement with the different stars colored in **(a-b)**. Red curves in **(c)** and **(d)** depict the LUMO of non-coordinated molecular species.

In order to study the influence of the chemical environment in the frontier orbital energy shifts of the metal-organic coordination, several spectra are acquired for the different phases (α, β and γ) studied in chapter 3. Figure 8.2 shows how the molecular resonances for the different phases vary depending on its coordination with one or two Ce atoms. Phases α, β and borders of γ show single Ce-coordinated molecules (Figure 8.1 (c,d) and 8.2 (b)) with a spectroscopic behavior previously described. Phase γ shows double Ce-coordinated molecules (Figure 8.2 (a,c)) and the spectroscopic data exhibit similar resonances in the molecular backbone as the spectra is taken at equal distances from the closer Ce atom.

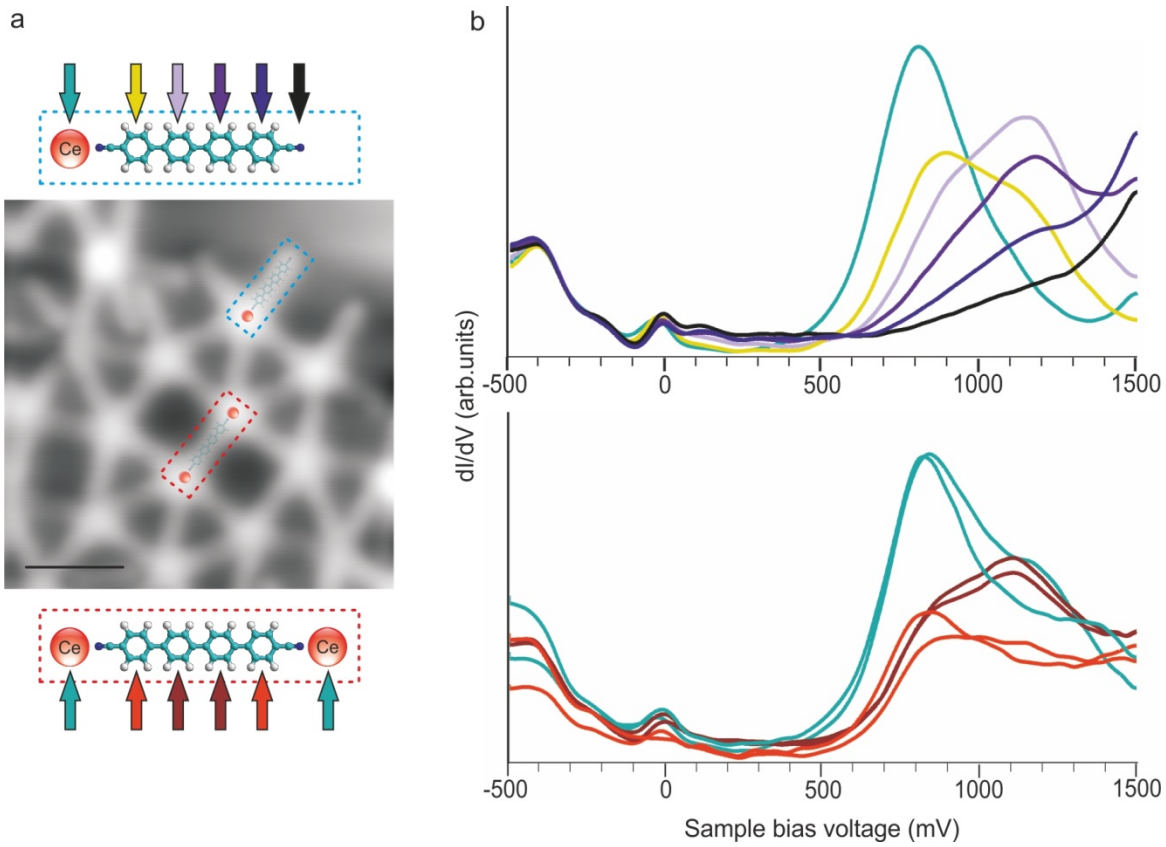

Figure 8 . 2 | STS curves on Ce metal-organic systems in different bonding enviroments

a, High-resolution STM image of a five-fold Ce : *p*-NC-Ph_4-CN-*p* system. Blue and red doted rectangles depict atomistic models of Ce : *p*-NC-Ph_4-CN-*p* and Ce : *p*-NC-Ph_4-CN-*p* : Ce systems, respectively. The colored arrows in the doted rectangles indicate the points where the STS data have been measured. Scanning parameters: V_b = 0.2 V, I = 80 pA. Scale bar: 3 nm. **b,** Upper STS curves present spatially resolved spectroscopic data revealing the downshift phenomena in the molecular frontier orbital energy. Lower STS curves present spatially resolved spectroscopic data revealing the influence of the chemical environment in the shifting of molecular orbitals. The different colors of the STS curves are in agreement with the different arrows colored in **(a)**.

- **Gd + *p*-NC-Ph_4-NC-*p***

To investigate the influence of the lanthanide atoms on the electronic structure of the complex, similar STS studies were carried out with Gd atoms as metallic nodes Gd : (*p*-NC-Ph_4-CN-*p*)$_5$. Figure 8.3 reveals a similar localization behavior of the resonance peaks of a molecule while is coordinated with a Gd atom. The appearance of two resonance peaks at 1.37 V and 2.02 V delocalized along non-coordinated molecules (red star and curve in Figure 8.3 (c)) is observed. The non-coordinated extremity of a coordinated *p*-NC-Ph_4-CN-*p* molecule presents two peaks at 1.13 V and 1.75 V, whose relative intensity

is modulated depending on the proximity of the point of spectra acquisition to the Gd atom (green, light blue and purple stars and curves in Figure 8.3 (c)). The Gd node presents a peak at 0.75 V. Hence, the downshift of LUMO and LUMO +1 around 0.25 V is attributed to the coordination with the Gd atom, showing a strong localization of the molecular orbitals due to the influence of the Gd coordination.

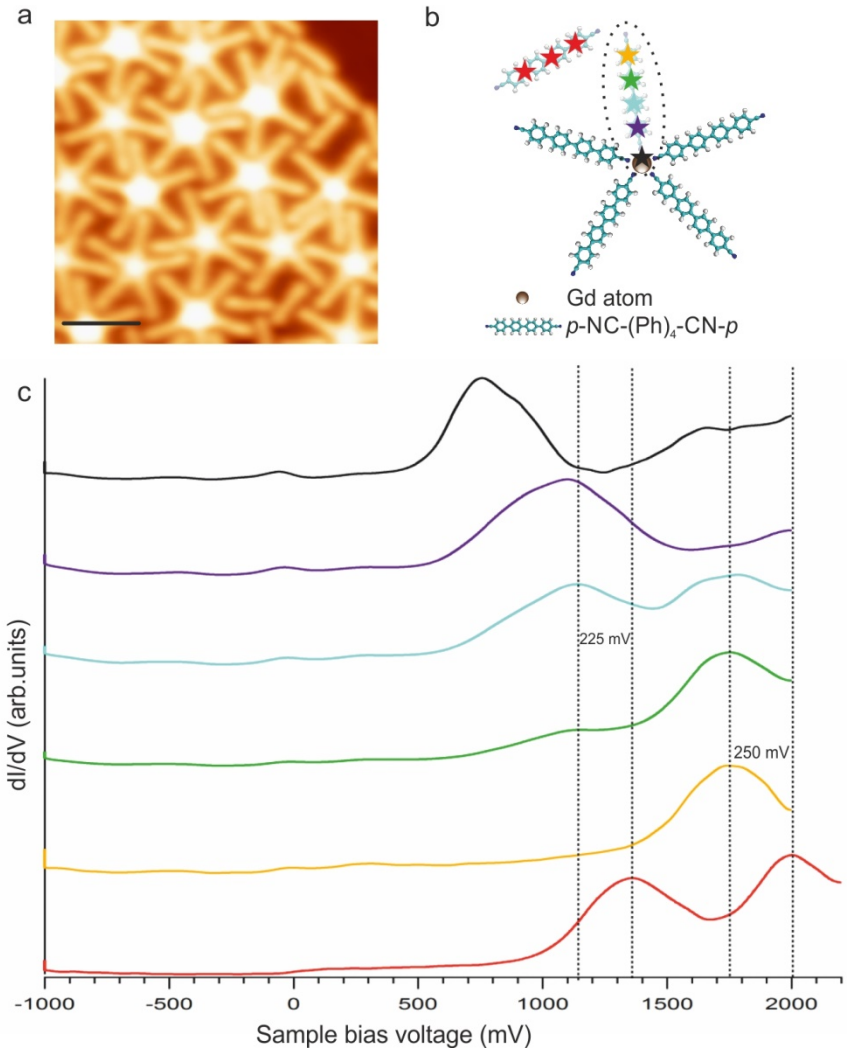

Figure 8 . 3 | Spectroscopic characterization of Gd(*p*-NC-Ph$_4$-CN-*p*)$_5$ supramolecules

a, High-resolution STM image of Gd(*p*-NC-Ph$_4$-CN-*p*)$_5$ supramolecules coexisting with some non-coordinated molecular linkers. Scanning parameters: V_b = 0.3 V, I = 60 pA. Scale bar: 3 nm. **b,** Atomistic model of one of the pentameric units and a non-coordinated molecules shown in **(a)**. The colored stars indicate the points where the STS data have been measured. **c,** Spatially resolved spectroscopic data reveal the downshift phenomena in the frontier orbital energy. The different colors of the STS curves are in agreement with the different stars colored in **(b)**.

- **Co + *p*-NC-Ph$_4$-NC-*p***

For comparison, a system with a transition metal (Co) as the metal node in the metal-carbonitrile network is also inspected. Herein, the LUMO (1.36 V) and LUMO +1 (2.02 V) of a non-coordinated organic molecule are again shown in the red curve of Figure 8.4 (c). Spectra acquired at the center of a double Co-coordinated molecule (light blue star and curve in Figure 8.4 (b,c)) shows two peaks at 1.16 V and at 1.73 V revealing a downshift of around 0.2 V with respect to non-coordinated molecules. STS of the cobalt node only reveals a peak at 1.16 V (olive star and curve in Figure 8.4 (b,c)). Thus, a similar electronic behavior as in the Gd : *p*-NC-Ph$_4$-CN-*p* system is found using a transition metal (Co) as the metal node.

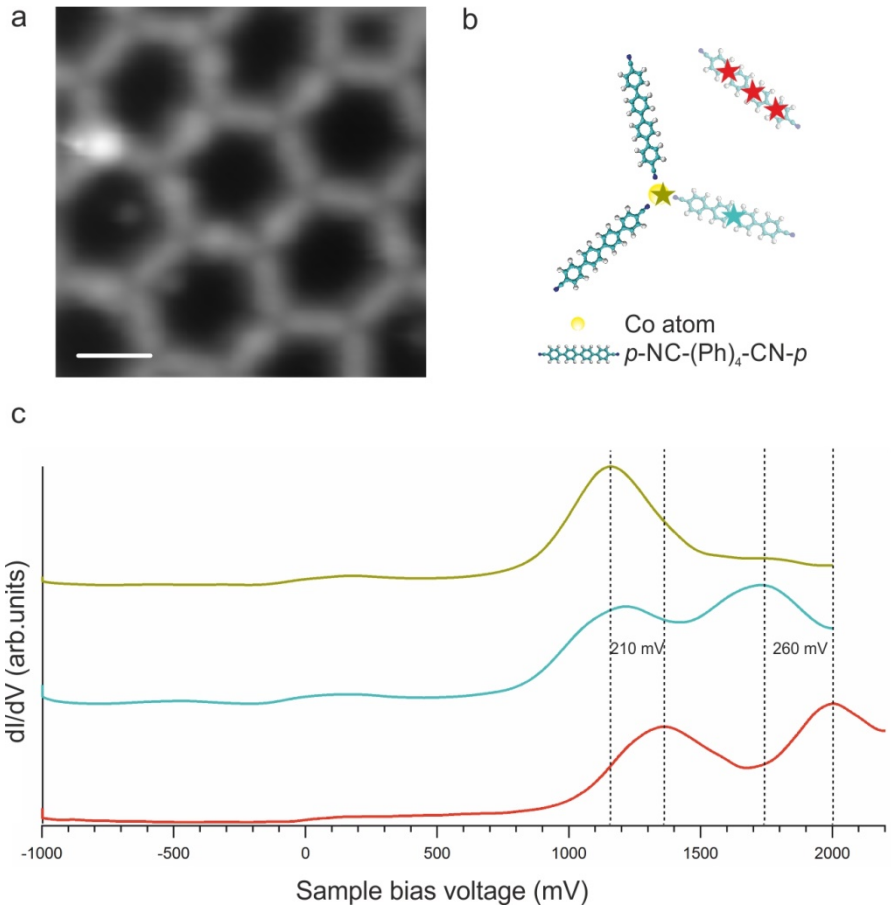

Figure 8 . 4 | Spectroscopic characterization of Co(*p*-NC-Ph$_4$-CN-*p*)$_3$ supramolecules

a, High-resolution STM image of a three-fold Co : *p*-NC-Ph$_4$-CN-*p* network. Scanning parameters: V_b = 0.5 V, I = 75 pA. Scale bar: 2 nm. **b,** Atomistic model of a Co(*p*-NC-Ph$_4$-CN-*p*)$_3$ unit shown in **(a)**. The colored stars indicate the points where the STS data have been measured. **c,** Spatially resolved spectroscopic data

reveal the downshift phenomena in the frontier orbital energy. The different colors of the STS curves are in agreement with the different stars colored in **(b)**. Red curve depicts the LUMO and LUMO +1 orbitals of the non-coordinated *p*-NC-Ph_4-CN-*p* molecule.

- **Gd + TPCN**

In the last STS analysis a different organic molecule with a carbonitrile functional endgroup, i.e. extended porphyrin (TPCN, chapter 5) is studied in its coordination with Gd atoms. Once again the typical downshift in the molecular resonance is observed ranging from 1.90 V for the spectra acquired at the extremities of the porphyrin derivate (red star and curve in Figure 8.5 (b,c)) to 1.25 V assigned to the spectra acquired at the Gd node of around 0.7 V (black star and curve in Figure 8.5 (b,c)). Resonance features related to the porphyrin chemical pocket and its metalation with Co atoms are summarized elsewhere[215].

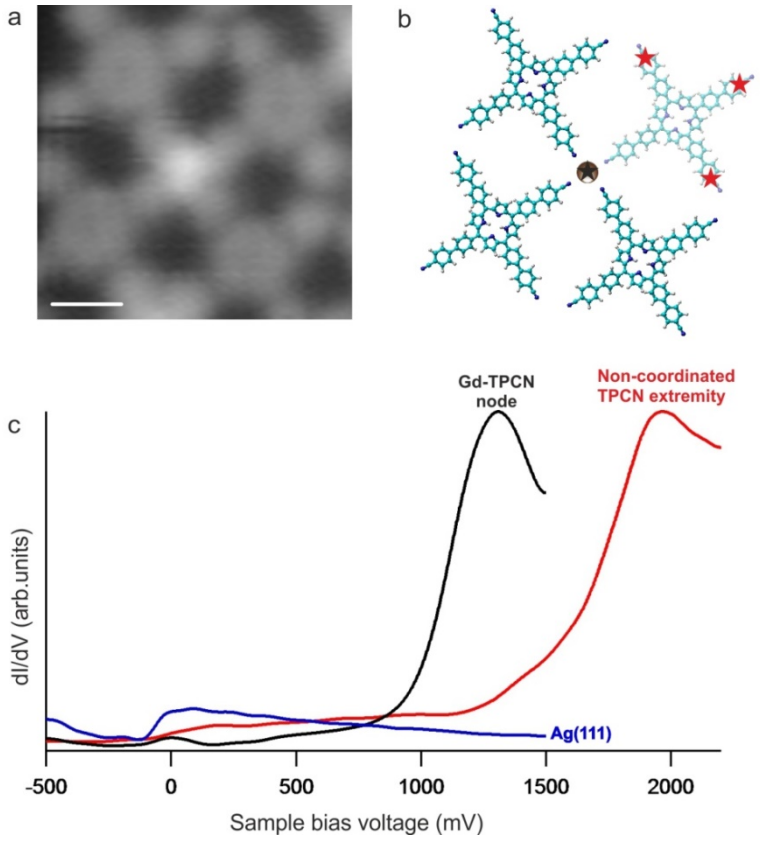

Figure 8 . 5 | Spectroscopic characterization of Gd : TPCN networks

a, High-resolution STM image of a Gd : TPCN network. Scanning parameters: V_b = 0.5 V, I = 100 pA. Scale bar: 2 nm. **b,** Atomistic model of $Gd(TPCN)_4$ shown in **(a)**. The colored stars indicate the points where the STS data have been measured. **c,** Spatially resolved spectroscopic data reveal the downshift phenomena in

the frontier orbital energy. The different colors of the STS curves are in agreement with the different stars colored in **(b)**. Blue curve depicts the surface state of the Ag(111) surface.

In summary we have shown in this section how the use of scanning tunneling spectroscopy (STS) allows detailed spectroscopic characterization of the molecular orbitals of several lanthanide-carbonitrile systems. These data indicate that the characteristic frontier orbital of the different systems is preserved but downshifted in energy independently of the lanthanide (Ce or Gd) and the molecule (with carbonitrile endgroups) employed. Spectroscopic studies of more lanthanide metal-organic systems would be spread out in further experiments giving an insight into the charge redistribution at metal-organic interfaces crucial for the understanding of the energy level alignment.

9. Experimental method´s summary

In this section a detailed description of the experimental methods used in chapters 3-6 is described:

- ***Five-fold lanthanide (Ce/Gd)-carbonitrile coordination on surfaces* (chapter 3):**

The experiments were performed using two independent custom designed ultra-high vacuum systems that hosted an Aarhus 150 STM (VT-STM, see www.specs.com) and a low-temperature STM (LT-STM, see www.lt-stm.com), respectively. The base pressure was below 2×10^{-10} mbar in the LT-STM system and below 1×10^{-9} mbar in the variable temperature-STM system. V_{bias} is applied to the sample.

The Ag(111) substrate was prepared by standard cycles of Ar^+ sputtering (800 eV) and subsequent annealing to 723 K for 10 minutes. All STM images were taken in constant-current mode with electrochemically etched tungsten tips.

The supramolecular networks based on the Ce/Gd-ligand coordination motifs described in the manuscript were fabricated in a two-step process:

1. The molecular linkers *p*-NC-Ph_3-CN-*p* (*p*-NC-Ph_4-CN-*p*) were deposited by organic molecular beam epitaxy (OMBE) from a quartz crucible held at T = 478 K (503 K) onto a clean Ag(111) crystal held at ≈ 300 K.

2a. For the Ce networks: Ce atoms were evaporated from a homemade water-cooled cell by resistively heating a W filament enclosing a Ce ball of high purity (99.99%, MaTecK GmbH, 52428 Jülich, Germany) onto the sample held at ≈ 300 K.

2b. For the Gd networks: Gd atoms were deposited by means of electron beam evaporation onto the sample held at ≈ 300 K from an outgassed Gd rod (99.9%, MaTecK GmbH, 52428 Jülich, Germany).

After the growth protocol, the scanning tunneling microscopy inspection reveals whether the deposition of lanthanide on the surface was adequate or, on the contrary, lower or higher than expected.

The DFT calculations were performed using the QuickStep module[261] within the CP2K program suite (http://www.CP2K.org/). The adsorbed structures were modeled with the slab approach, where four layers of substrate were used, of which the two uppermost were relaxed. Hexagonal cells with lateral dimensions of 46.27 and 43.03 Å were used in α and β phases, respectively, and a monoclinic cell of 30.61 Å × 32.20 Å with an angle 91.945° with eight molecules in the purely molecular phase.[103] In the β structure the DFT-optimized value of the lattice constant of Ag was used because laterally the structure is covalently bound and we indeed observed strain when the experimental lattice constant was employed. Vertically the cell dimension was chosen as 35 Å except in the β phase where a value of 25.25 Å was applied. Only Γ point was used to sample the surface Brillouin zone, and Fermi-Dirac broadening at 300 K was used to broaden the occupation numbers around the Fermi energy.

As the exchange-correlation functional we employed the revPBE[262] generalized-gradient approximation, with long-range dispersion included using the DFT-D3 empirical correction.[263] The Kohn-Sham equations were solved within the Gaussian plane wave (GPW) scheme.[264] The details are similar to our recent investigations of *h*-BN adsorbed on transition metal surface:[265] The ionic cores were described using Goedecker-Teter-Hutter pseudo potentials,[266] the density expanded in a plane wave basis set up to the cut-off energy of 900 Ry (in molecular phase 500 Ry) and the wave functions in the DZVP Gaussian basis set of the MOLOPT type;[267] for Ce we included 30 electrons in the valence and a [4432] basis set. The binding energies were calculated without relaxing the system upon the removal of the molecule in question, i.e. just removing the atomic coordinates of the molecule.

- ***Manifold lanthanide (Eu)-carbonitrile coordination on surfaces: A route to quasicrystallinity (Chapter 4):***

The experiments were performed using a custom-designed ultra-high vacuum systems that hosted an Omicron scanning tunneling microscope (STM). The base pressure was below 4 × 10^{-10} mbar in the variable temperature-STM system. V_{bias} in tunneling conditions is applied to the sample.

The Au(111) substrate was prepared using standard cycles of Ar^+ sputtering (800 eV) and subsequent annealing to 723 K for 10 minutes. All STM images were taken in constant-current mode with an electrochemically etched tungsten tip.

The supramolecular networks based on Eu-ligand coordination motifs described in the manuscript were fabricated in a three-step process:

1.- The molecular linkers *p*-NC-Ph_4-CN-*p* were deposited by organic molecular beam epitaxy (OMBE) from a quartz crucible held at T = 493 K onto a clean Au(111) crystal at ≈ 298 K.

2.- Next, Eu atoms were deposited by means of electron beam evaporation onto the sample held at ≈ 298 K from an outgassed Eu rod (99.5%, MaTecK GmbH, 52428 Jülich, Germany). Thereafter, sample was annealed to ≈ 373 K for 10 minutes with a subsequent cooling rate of ≈ 2 °C/min to room temperature and inspected with STM.

3.- The europium to linker stoichiometric ratio was carefully controlled to design specific supramolecular networks. On one hand, the formation of random string networks based on threefold coordination nodes, reticular fourfold asemblies, and ddQC networks, respectively, was achieved in a step-by-step process starting with the random string networks and depositing more *p*-NC-Ph_4-CN-*p* linkers to the sample to grow the desired phase. On the other hand, the hexagonal lattice stabilized by six-fold nodes was formed on a pristine Au(111) sample, just following steps 1 and 2 of the growth protocol.

The molecular force field MMFF implementation in the program CHARMM was employed to model the quasicrystalline pattern. The Eu-N distance between the minimized linkers and the Europium nodes was set to 2.51 Å, the Europium nodes positively charged and fixed, and the whole structure subsequently relaxed to a RMS gradient of 1 cal mol^{-1}. An Eu-N distance of 2.51 Å was obtained from MP2 quantum mechanical calculations of the Eu(I)[benzonitrile]$^+_4$ complex with the Gaussian 09 program, where the Adamo implementation of the Perdew, Burke and Ernzerhof was used as the functional with a 6-311G basis set and the MWB52 Stuttgart/Dresden electron core potential for europium. _ENREF_210

- ***Orthogonal insertion of lanthanide (Gd) and transition metal (Co) atoms in metal-organic networks on surfaces (Chapter 5):***

The experiments were perform in a custom designed ultra-high vacuum system that hosts a low-temperature STM (LT-STM, see www.lt-stm.com), where the base pressure was below 5×10^{-10} mbar. All STM images were taken in constant-current mode with electrochemically etched tungsten tips, applying a bias (V_{bias}) to the sample and at a temperature of ≈ 6 K. The Ag(111) substrate was prepared by standard cycles of Ar^+ sputtering (800 eV) and subsequent annealing to 723 K for 10 minutes. Deposition of metallic or molecular species was done holding the sample at room temperature, if not stated otherwise. 2H-TPCN molecules were deposited by organic molecular-beam epitaxy (OMBE) from a quartz crucible held at 718 K onto a clean Ag(111) crystal. Gd atoms were sublimated by means of electron beam evaporation from an outgassed Gd rod (99.9%, MaTecK GmbH, 52428 Jülich, Germany). Co atoms were evaporated from a homemade water-cooled cell by resistively heating a W filament enclosing a Co rod of high purity.

- ***Lanthanide (Gd)-carboxylate coordination on surfaces (Chapter 6):***

The experiments were carried out in two distinct custom designed ultra-high vacuum systems, where the base pressure was below 5×10^{-10} mbar. Measurements at cryogenic conditions (≈ 6 K) were performed in an ultra-high vacuum system that hosts a Createc LT-STM. Variable-temperature STM (77 - 393 K) using an Aarhus-150 STM investigations were carried out in a unique ultrahigh-vacuum system to allow precise control of surface composition. All STM images were taken in constant-current mode with electrochemically etched tungsten tips, applying a bias (V_{bias}) to the sample. The Cu(111) substrate was prepared by standard cycles of Ar^+ sputtering (800 eV) and subsequent annealing to 723 K for 10 minutes. The metal-organic architectures were fabricated following a two-step protocol. First, a submonolayer TDA coverage was prepared by organic molecular-beam epitaxy (OMBE) from a quartz crucible held at 543 K onto a clean Cu(111) crystal at room temperature if not stated otherwise. Subsequently, sample was annealed to 423 K and gadolinium (Gd) atoms were sublimated by means of

electron beam evaporation from an outgassed Gd rod (99.9%, MaTecK GmbH, 52428 Jülich, Germany).

Simulations: First-principles calculations have been performed using the VASP package.[268-270] The generalized gradient approximation (GGA) for the exchange-correlation functional of Perdew, Burke, and Ernzerhof (PBE)[271] is employed, with dispersion correction using Grimme's DFT-D2 scheme.[272] The effective potentials of core electrons are described using the projector-augmented wave (PAW) pseudopotentials,[273,274] as implemented in the VASP code. For Gd, the valency of the pseudopotential is 9 and the spatially localized 4f electrons are kept frozen in the core. A cutoff energy of 450 eV for the plane wave expansion and a Methfessel-Paxton smearing[275] of 0.2 eV for the occupation of electronic states are chosen. Geometries are optimized with Γ-point for Brillouin-zone sampling until all forces are smaller than 0.02 eV $Å^{-1}$. Single-point energies are calculated with a 3 × 3 × 1 *k*-point mesh according to the Monkhorst-Pack grid.[276] Atomic charges are computed by Bader's topological analysis of the electron density (including the core charge)[277] using the Bader analysis program[278] for VASP. The Cu(111) surface is modeled by a four-layer slab separated by ≈ 11 Å of vacuum in the surface normal direction, and the topmost two layers are allowed to relax during geometry optimizations. The binding energies are calculated by directly removing the molecule in question from the network whose geometry remains unchanged. In order to visualize the charge transfer in the Gd-TDA adlayer in a two-dimensional presentation, the distribution of the so-called electron density displacement field, DF*(x,y)*, is plotted. The electron density difference ($\Delta\rho$) between the combined system ($\rho_{Gd\text{-}TDA/Cu}$) and the sum of its separated constituents (calculated as freestanding neutral species in the frozen geometry) is defined as $\Delta\rho = \rho_{Gd\text{-}TDA/Cu} - (\rho_{Gd} + \rho_{TDA} + \rho_{Cu})$. DF*(x,y)* is calculated by integrating $\Delta\rho$ from the plane dividing the substrate and adlayer (z_{sub}) up to vacuum[246]:

$$\mathrm{DF}(x,y) = \int_{Zsub}^{vacuum} \Delta\rho(x,y,z)\mathrm{d}z$$

10. List of publications

- Ecija, D.; **Urgel, José I.**; Auwärter, W.*;* Papageorgiou, A. C.; Seitsonen, A. P.; Vijayaraghavan, S.; Joshi, S.; Fischer, S.; Reichert, J. and Barth, J. V. **Five-Vertex Archimedean Surface Tessellation by Lanthanide-Directed Molecular Self-Assembly.** *Proc. Natl. Acad. Sci. USA.* **110**, 6678-6681 (2013).

- Joshi, S.; Bischoff, F.; Koitz, R.; Ecija, D.; Seufert, K.; Seitsonen, A. P.; Hutter, J.; Diller, K.; **Urgel, José I.**; Sachdev, H.; Barth, J. V. and Auwarter, W. **Control of Molecular Organization and Energy Level Alignment by an Electronically Nanopatterned Boron Nitride Template.** *Acs Nano*. 8 (1), 430-442 (2013).

- **Urgel, José I.**; Ecija, D.; Auwärter, W. and Barth, J. V. **Controlled Manipulation of Gadolinium-Coordinated Supramolecules by Low Temperature Scanning Tunneling Microscopy.** *Nano Letters*. 14, 1369-1373 (2014).

- **Urgel, José I.**; Ecija, D.; Auwärter, W.; Papageorgiou, A. C.; Seitsonen, A. P.; Vijayaraghavan, S.; Joshi, S.; Fischer, S.; Reichert, J. and Barth, J. V**. Five-Vertex Lanthanide Coordination on Surfaces: A Route to Sophisticated Nanoarchitectures and Tessellations.** *J. Phys. Chem. C.* 118, 12908-12915 (2014).

- Chen, Z; Klyatskaya, S; **Urgel, José I.**; Ecija, D.; Fuhr, O.; Auwärter, W.; Barth, J. V. and Ruben, M. **Synthesis, Characterisation, Monolayer Assembly and Lanthanide-Organic Coordination Networks Using a Linear Terphenyl-Di(propiolonitrile) Linker on Ag(111).** *Beilstein J. Nanotechnol.* 6, 327-335 (2014).

- **Urgel, José I**; Schwarz, Martin; Garnica, M.; Stassen, D.; Bonifazi, D.; Ecija, D.; Barth, J.V. and Auwärter, W. **Controlling Coordination Reactions and Assembly on an Insulating Boron Nitride Monolayer.** *J. Am. Chem. Soc.* 137 (7), 2420-2423 (2015).

- **Urgel, José I.**; Ecija, D.; Auwärter, W.; Stassen, D.; Bonifazi, D. and Barth, J.V. **Orthogonal Insertion of Lanthanide and Transition Metal Atoms in Metal-Organic Networks on Surfaces.** *Angew. Chem. Int. Ed.* 54 (21), 6163-6167 (2015).

- **Urgel, José I.**; Vijayaraghavan, S.; Ecija, D.; Auwärter, W. and Barth, J. V. **Tetracene Confinement in L-Methionine Gratings on the Ag (111) Surface.** *Surf. Sci*. (2015).

- **Urgel, José I.**; Cirera, B.; Wang, Y.; Auwärter, W.; Otero, R.; Gallego, J.M.; Alcamí, M.; Martin, F.; Miranda, R.; Ecija, D. and Barth, J.V. **Surface-Supported Robust Two-Dimensional Lanthanide-Carboxylate Coordination Networks.** *Small*. (2015).

- Lyu, G.; Zhang, Q.; **Urgel, José I.**; Kuang, G.; Auwärter, W.; Ecija, D.; Barth, J. V. and Lin, N. **Tunable Surface-Confined Lanthanide-Directed Networks by Exploiting Coordinative Flexibility through Ligand Stoichiometry.** *Chem. Commun*. (2015). Accepted.

- **Urgel, José I.**; Ecija, D.; Lyu, G.; Zhang, R.; Palma, C. A.; Auwärter, W.; Lin, N. and Barth, J. V. **Quasicrystallinity Expressed in 2D Coordination Lattices.** *Nat. Chem.* (2015). In peer review process.

11. Bibliography

1 Feynman, R. P. There's Plenty of Room at the Bottom. *Engineering and science* **23**, 22-36 (1960).

2 Balzani, V. Nanoscience and Nanotechnology: The Bottom-up Construction of Molecular Devices and Machines. *Pure Appl. Chem.* **80**, 1631-1650 (2008).

3 Hamlett, C. A. *Utilization of Nanostructured Surfaces for Sensing Applications and the Use of Nanoentities for the Fabrication of New Materials*. PhD thesis, University of Birmingham (UBir), (2008).

4 Bhattacharyya, D.; Singh, S.; Satnalika, N.; Khandelwal, A. & Jeon, S.-H. Nanotechnology, Big Things from a Tiny World: A Review. *Nanotechnology* **2** (2009).

5 Allhoff, F. *Nanoethics: The Ethical and Social Implications of Nanotechnology*. (John Wiley & Sons, 2007).

6 Binnig, G.; Rohrer, H.; Gerber, C. & Weibel, E. Surface Studies by Scanning Tunneling Microscopy. *Phys. Rev. Lett.* **49**, 57 (1982).

7 Barth, J. V.; Brune, H.; Ertl, G. & Behm, R. J. Scanning Tunneling Microscopy Observations on the Reconstructed Au (111) Surface: Atomic Structure, Long-Range Superstructure, Rotational Domains, and Surface Defects. *Phys. Rev. B* **42**, 9307 (1990).

8 Jung, T.; Schlittler, R. & Gimzewski, J. Conformational Identification of Individual Adsorbed Molecules with the Stm. *Nature* **386**, 696-698 (1997).

9 Nadj-Perge, S. *et al.* Observation of Majorana Fermions in Ferromagnetic Atomic Chains on a Superconductor. *Science* **346**, 602-607 (2014).

10 Eigler, D. M. & Schweizer, E. K. Positioning Single Atoms with a Scanning Tunnelling Microscope. *Nature* **344**, 524-526 (1990).

11 Green, M. F. *et al.* Patterning a Hydrogen-Bonded Molecular Monolayer with a Hand-Controlled Scanning Probe Microscope. *Beilstein J. Nanotechnol.* **5**, 1926-1932 (2014).

12 Crommie, M. F.; Lutz, C. P. & Eigler, D. M. Confinement of Electrons to Quantum Corrals on a Metal Surface. *Science* **262**, 218-220 (1993).

13 Wang, B.; Bocquet, M.-L.; Marchini, S.; Günther, S. & Wintterlin, J. Chemical Origin of a Graphene Moiré Overlayer on Ru (0001). *Phys. Chem. Chem. Phys.* **10**, 3530-3534 (2008).

14 Schlickum, U. *et al.* Metal-Organic Honeycomb Nanomeshes with Tunable Cavity Size. *Nano Lett.* **7**, 3813-3817 (2007).

15 Auwärter, W.; Ecija, D.; Klappenberger, F. & Barth, J. V. Porphyrins at Interfaces. *Nat. Chem.* **7**, 105-120 (2015).

16 http://www.research.ibm.com/articles/madewithatoms.shtml. *IBM.*

17 De Feyter, S. & De Schryver, F. C. Two-Dimensional Supramolecular Self-Assembly Probed by Scanning Tunneling Microscopy. *Chem. Soc. Rev.* **32**, 139-150 (2003).

18 Barth, J. V. Molecular Architectonic on Metal Surfaces. *Annu. Rev. Phys. Chem.* **58**, 375-407 (2007).

19 Atwood, D. A. *The Rare Earth Elements: Fundamentals and Applications*. (John Wiley & Sons, 2013).

20 Werts, M. H. Making Sense of Lanthanide Luminescence. *Sci. Prog.* **88**, 101-131 (2005).

21 Bünzli, J.-C. G. Lanthanide Luminescence for Biomedical Analyses and Imaging. *Chem. Rev.* **110**, 2729-2755 (2010).

22 Liu, Y. *et al.* Amine-Functionalized Lanthanide-Doped Zirconia Nanoparticles: Optical Spectroscopy, Time-Resolved Fluorescence Resonance Energy Transfer Biodetection, and Targeted Imaging. *J. Am. Chem. Soc.* **134**, 15083-15090 (2012).

23 Aime, S. *et al.* Paramagnetic Lanthanide (III) Complexes as Ph-Sensitive Chemical Exchange Saturation Transfer (Cest) Contrast Agents for Mri Applications. *Magn. Reson. Med.* **47**, 639-648 (2002).

24 Soini, E.; Lövgren, T. & Reimer, C. B. Time-Resolved Fluorescence of Lanthanide Probes and Applications in Biotechnology. *Crit. Rev. Anal. Chem.* **18**, 105-154 (1987).

25 Sudhakaran Pillai, S. *Luminescent Materials Based on Lanthanide Ions*. PhD thesis, Kingston University London (KUL), (2010).

26 Bethencourt, M.; Botana, F.; Calvino, J.; Marcos, M. & Rodriguez-Chacon, M. Lanthanide Compounds as Environmentally-Friendly Corrosion Inhibitors of Aluminium Alloys: A Review. *Corros. Sci.* **40**, 1803-1819 (1998).

27 Fricker, S. P. The Therapeutic Application of Lanthanides. *Chem. Soc. Rev.* **35**, 524-533 (2006).

28 Thompson, K. H. & Orvig, C. Editorial: Lanthanide Compounds for Therapeutic and Diagnostic Applications. *Chem. Soc. Rev.* **35**, 499-499 (2006).

29 Wang, G.; Peng, Q. & Li, Y. Lanthanide-Doped Nanocrystals: Synthesis, Optical-Magnetic Properties, and Applications. *Acc. Chem. Res.* **44**, 322-332 (2011).

30 Kilbourn, B. T. New Industrial Applications of the Lanthanides. *Inorg. Chim. Acta* **94**, 37 (1984).

31 Ferbinteanu, M.; Cimpoesu, F. & Tanase, S. in *Lanthanide Metal-Organic Frameworks* 185-229 (Springer, 2014).

32 Ma, S.; Yuan, D.; Wang, X.-S. & Zhou, H.-C. Microporous Lanthanide Metal-Organic Frameworks Containing Coordinatively Linked Interpenetration: Syntheses, Gas Adsorption Studies, Thermal Stability Analysis, and Photoluminescence Investigation. *Inorg. Chem.* **48**, 2072-2077 (2009).

33 Ren, Y. w. *et al.* 1, 4-Phenylenediacetate-Based Ln Mofs–Synthesis, Structures, Luminescence, and Catalytic Activity. *Eur. J. Inorg. Chem.* **2011**, 4369-4376 (2011).

34 Shibasaki, M.; Yamada, K. I. & Yoshikawa, N. in *Lanthanide Lewis Acids Catalysis* Ch. 20, 911-944 (1999).

35 Cui, Y.; Chen, B. & Qian, G. Lanthanide Metal-Organic Frameworks for Luminescent Sensing and Light-Emitting Applications. *Coord. Chem. Rev.* **273**, 76-86 (2014).

36 Woodruff, D. N.; Winpenny, R. E. P. & Layfield, R. A. Lanthanide Single-Molecule Magnets. *Chem. Rev.* **113**, 5110-5148 (2013).

37 Shiga, T.; Okawa, H.; Kitagawa, S. & Ohba, M. Stepwise Synthesis and Magnetic Control of Trimetallic Magnets $[Co_2ln(L)_2(H2O)_4][Cr(Cn)_6]\cdot nH_2O$ (Ln= La, Gd; H_2l= 2, 6-Di (Acetoacetyl) Pyridine) with 3-D Pillared-Layer Structure. *J. Am. Chem. Soc.* **128**, 16426-16427 (2006).

38 Tanase, S. & Reedijk, J. Chemistry and Magnetism of Cyanido-Bridged d–f Assemblies. *Coord. Chem. Rev.* **250**, 2501-2510 (2006).

39 Culp, J. T. *et al.* Magnetism of Metal Cyanide Networks Assembled at Interfaces. *Coord. Chem. Rev.* **249**, 2642-2648 (2005).

40 Ecija, D. *et al.* Five-Vertex Archimedean Surface Tessellation by Lanthanide-Directed Molecular Self-Assembly. *Proc. Natl. Acad. Sci. USA.* **110**, 6678-6681 (2013).

41 Urgel, J. I. *et al.* Five-Vertex Lanthanide Coordination on Surfaces: A Route to Sophisticated Nanoarchitectures and Tessellations. *J. Phys. Chem. C* **118**, 12908-12915 (2014).

42 Urgel, J. I.; Ecija, D.; Auwarter, W. & Barth, J. V. Controlled Manipulation of Gadolinium-Coordinated Supramolecules by Low-Temperature Scanning Tunneling Microscopy. *Nano Lett.* **14**, 1369-1373 (2014).

43 Urgel, J. I. *et al.* Orthogonal Insertion of Lanthanide and Transition-Metal Atoms in Metal–Organic Networks on Surfaces. *Angew. Chem. Int. Ed.* **54**, 6163-6167 (2015).

44 Urgel, J. I. *et al.* Surface-Supported Robust 2D Lanthanide-Carboxylate Coordination Networks. *Small*, doi:10.1002/smll.201502761 (2015).

45 Schatz, G. C. & Ratner, M. A. *Quantum Mechanics in Chemistry*. (Courier Corporation, 2012).

46 Feynman, R. P. L., R. *"Física Volumen 3: Mecánica Cuántica"*. ((Alhambra Mexicana, 2000)).

47 http://www.ieap.uni-kiel.de/surface/ag-kipp/stm/stm.htm. *From S. Woedtke, Ph.D. Thesis, Inst. F. Exp. U. Ang. Phys. Der Cau Kiel.*

48 Stroscio, J. A. & Kaiser, W. J. *Scanning Tunneling Microscopy*. Vol. 27 (Academic Press, 1993).

49 Bai, C. *Scanning Tunneling Microscopy and Its Application*. Vol. 32 (Springer Science & Business Media, 2000).

50 Chen, C. J. *Introduction to Scanning Tunneling Microscopy*. (Oxford University Press, 2008).

51 http://www.vmechanm.blogspot.de/2007_04_01_archive.html. *Tunnel Effect.*

52 Tersoff, J. & Hamann, D. Theory and Application for the Scanning Tunneling Microscope. *Phys. Rev. Lett.* **50**, 1998 (1983).

53 Bardeen, J. Tunnelling from a Many-Particle Point of View. *Phys. Rev. Lett.* **6**, 57 (1961).

54 Hamers, R. Atomic-Resolution Surface Spectroscopy with the Scanning Tunneling Microscope. *Annu. Rev. Phys. Chem.* **40**, 531-559 (1989).

55 Tersoff, J. & Hamann, D. Theory of the Scanning Tunneling Microscope. *Phys. Rev. B* **31** (1985).

56 Vijayaraghavan, S. *Molecular Nanoscience and Chemical Physics of Interfaces*. PhD thesis, TUM (Technische Universität München), (2013).

57 Müller, T. Scanning Tunneling Microscopy: A Tool for Studying Self-Assembly and Model Systems for Molecular Devices. *Veeco Instruments Inc.(Santa Barbara, CA)(AN 85, Rev AO, 1/05)* (2005).

58 Hipps, K. Handbook of Applied Solid State Spectroscopy. *Scanning Tunneling Spectroscopy*, 1-33 (2006).

59 Hla, S. H. Scanning Tunneling Microscopy Single Atom/Molecule Manipulation and Its Application to Nanoscience and Technology. *J. Vac. Sci. Technol. B* **23**, 1351 (2005).

60 Bonnell, D. *Scanning Probe Microscopy and Spectroscopy: Theory, Techniques, and Applications*. (Wiley-vch, 2001).

61 Seufert, K. Surface Anchored Porphyrins - Investigations of Assembly, Reactivity, Manipulation and in-Situ Synthesis. Phd Thesis. (Technische Universität München 2011).

62 www.oerlikon.com. *Molecular Pumps by Oerlikon Leybold Vacuum Gmbh T.*

63 www.pfeiffer-vacuum.com. *Pump by Pfeiffer Vacuum Inc. D.*

64 www.varianinc.com. *Pump by Varian Inc. I.*

65 Weber, A. *Supramolecular Organization, Conformation and Electronic Properties of Porphyrin Molecules on Metal Substrates*. PhD thesis, University of British Columbia, Vancouver, (2007).

66 Weber, A. *Design and Investigation of Molecular Nanostructures on Surfaces with a Low-Temperature Scanning Tunneling Microscope* PhD thesis, University of British Columbia (UBC), (2005).

67 http://www.sps-createc.com. *Sps-Createc Gmbh, Magnusstr. 11, 12489 Berlin, Germany.*

68 http://www.focus-gmbh.com/uhv-instruments/EFM/EFM.html. *Focus Gmbh, Neukirchner Str. 2, 65510 Huenstetten, Germany.*

69 Lloyd, J. A. *Biologically Active Molecules Confined in 2D: Self-Assembly, Thermal Behavior & Chemical Transformations*. Master thesis, Technische Universität München (TUM), (2013).

70 Ecija, D. *Crecimiento, Autoorganización Y Caracterización Mediante Stm De Nanoestructuras Inorgánicas Y Orgánicas*. PhD thesis, Universidad Autónoma de Madrid (UAM), (2007).

71 http://www.scientaomicron.com/en/home. *Scientaomicron Gmbh, Limburger Str. 75, 65232 Taunusstein, Germany.*

72 www.phys.ust.hk/phnlin/.

73 Ernst, S. *Optimisation of the Preparation Process for Tips Used in Scanning Tunneling Microscopy*. PhD thesis, Technische Universität Dresden (TUD), (2006).

74 Barth, J. V.; Costantini, G. & Kern, K. Engineering Atomic and Molecular Nanostructures at Surfaces. *Nature* **437**, 671-679 (2005).

75 Bartels, L. Tailoring Molecular Layers at Metal Surfaces. *Nat. Chem.* **2**, 87-95 (2010).

76 Resel, R. Crystallographic Studies on Hexaphenyl Thin Films—a Review. *Thin Solid Films* **433**, 1-11 (2003).

77 Niko, A.; Meghdadi, F.; AmbroschDraxl, C.; Vogl, P. & Leising, G. Optical Absorbance of Oriented Thin Films. *Synth. Met.* **76**, 177-179 (1996).

78 Era, M.; Tsutsui, T. & Saito, S. Polarized Electroluminescence from Oriented P-Sexiphenyl Vacuum-Deposited Film. *Appl. Phys. Lett.* **67**, 2436-2438 (1995).

79 Marschall, M. *et al.* Random Two-Dimensional String Networks Based on Divergent Coordination Assembly *Nat. Chem.* **2**, 131-137 (2010).

80 Schlickum, U. *et al.* Surface-Confined Metal-Organic Nanostructures from Co-Directed Assembly of Linear Terphenyl-Dicarbonitrile Linkers on Ag(111). *J. Phys. Chem. C* **114**, 15602-15606 (2010).

81 Heim, D. *et al.* Surface-Assisted Assembly of Discrete Porphyrin-Based Cyclic Supramolecules. *Nano Lett.* **10**, 122-128 (2009).

82 Heim, D. *et al.* Self-Assembly of Flexible One-Dimensional Coordination Polymers on Metal Surfaces. *J. Am. Chem. Soc.* **132**, 6783-6790 (2010).

83 Ecija, D. *et al.* Two-Dimensional Short-Range Disordered Crystalline Networks from Flexible Molecular Modules. *ACS Nano* **6**, 4258-4265 (2012).

84 Liu, J. *et al.* Structural Transformation of Two-Dimensional Metal-Organic Coordination Networks Driven by Intrinsic in-Plane Compression. *J. Am. Chem. Soc.* **133**, 18760-18766 (2011).

85 Lin, N.; Dmitriev, A.; Weckesser, J.; Barth, J. V. & Kern, K. Real-Time Single-Molecule Imaging of the Formation and Dynamics of Coordination Compounds. *Angew. Chem. Int. Ed.* **41**, 4779-4783 (2002).

86 Dmitriev, A.; Spillmann, H.; Lin, N.; Barth, J. V. & Kern, K. Modular Assembly of Two-Dimensional Metal-Organic Coordination Networks at a Metal Surface. *Angew. Chem. Int. Ed.* **41**, 2670 - 2673 (2003).

87 Stepanow, S. *et al.* Steering Molecular Organization and Host-Guest Interactions Using Tailor-Made Two-Dimensional Nanoporous Coordination Systems. *Nat. Mater.* **3**, 229-233 (2004).

88 Bünzli, J.-C. G. Benefiting from the Unique Properties of Lanthanide Ions. *Acc. Chem. Res.* **39**, 53-61 (2006).

89 Hargittai, I. *Fivefold Symmetry*. (World Scientific Publishing Co. Pte. Ltd., 1992).

90 Dunlap, R. A. *The Golden Ratio and Fibonacci Numbers*. (World Scientific Publishing Co. Pte. Ltd, 1997).

91 https://en.wikipedia.org/wiki/Dodecahedrane.

92 https://myfolia.com/plantings/234114-tabernaemontana-corymbosa-sweet-love-tabernaemontana-corymbosa.

93 https://en.wikipedia.org/wiki/Red-knobbed_starfish.

94 https://asiakas.kotisivukone.com/files/productspace.ota.fi/Valokuvia/. *Vitruvius Pollio.*

95 http://www.davoscongress.ch/.

96 Kepler, J. *Harmonices Mundi*. (1619).

97 https://en.wikipedia.org/wiki/Johannes_Kepler. *Portrait of Johannes Kepler.*

98 Parviainen, R. *Connectivity Properties of Archimedean and Laves Lattices*. PhD thesis, Uppsala University (UU), (2004).

99 Harrison, A. First Catch Your Hare: The Design and Synthesis of Frustrated Magnets. *J. Phys.: Condens. Matter.* **16**, S553-S572 (2004).

100 Ueda, K.; Dotera, T. & Gemma, T. Photonic Band Structure Calculations of Two-Dimensional Archimedean Tiling Patterns. *Phys. Rev. B* **75**, 195122 (2007).

101 Mikhael, J.; Roth, J.; Helden, L. & Bechinger, C. Archimedean-Like Tiling on Decagonal Quasicrystalline Surfaces. *Nature* **454**, 501-504 (2008).

102 Tahara, K. *et al.* 2D Networks of Rhombic-Shaped Fused Dehydrobenzo[12]Annulenes: Structural Variations under Concentration Control. *J. Am. Chem. Soc.* **131**, 17583-17590 (2009).

103 Schlickum, U. *et al.* Chiral Kagome Lattice from Simple Ditopic Molecular Bricks. *J. Am. Chem. Soc.* **130**, 11778-11782 (2008).

104 Shi, Z. & Lin, N. Porphyrin-Based Two-Dimensional Coordination Kagome Lattice Self-Assembled on a Au(111) Surface. *J. Am. Chem. Soc.* **131**, 5376-5377 (2009).

105 Klappenberger, F. *et al.* Uniform Π-System Alignment in Thin Films of Template-Grown Dicarbonitrile-Oligophenyls. *Adv. Mater.* **21**, 1631-1642 (2011).

106 Arras, E.; Seitsonen, A. P.; Klappenberger, F. & Barth, J. V. Nature of the Attractive Interaction between Proton Acceptor and Organic Ring Systems. *Phys. Chem. Chem. Phys.* **14**, 15995-16001 (2012).

107 Kepler, J. *Harmonices Mundi Libri V*. (1969).

108 Stroscio, J. A. & Eigler, D. M. Atomic and Molecular Manipulation with the Scanning Tunneling Microscope. *Science* **254**, 1319-1326 (1991).

109 Jung, T. A.; Schlittler, R. R.; Gimzewski, J. K.; Tang, H. & Joachim, C. Controlled Room-Temperature Positioning of Individual Molecules: Molecular Flexure and Motion. *Science* **271**, 181-184 (1996).

110 Stipe, B. C.; Rezaei, M. A. & Ho, W. Inducing and Viewing the Rotational Motion of a Single Molecule. *Science* **279**, 1907-1909 (1998).

111 Bartels, L.; Meyer, G. & Rieder, K. H. Basic Steps of Lateral Manipulation of Single Atoms and Diatomic Clusters with a Scanning Tunneling Microscope Tip. *Phys. Rev. Lett.* **79**, 697-700 (1997).

112 Böhringer, M.; Morgenstern, K.; Schneider, W. D. & Berndt, R. Separation of a Racemic Mixture of Two Dimensional Molecular Clusters by Scanning Tunneling Microscopy. *Angew. Chem. Int. Ed.* **38**, 821-823 (1999).

113 Keeling, D. L. *et al.* Bond Breaking Coupled with Translation in Rolling of Covalently Bound Molecules. *Phys. Rev. Lett.* **94**, 146104 (2005).

114 Lastapis, M. *et al.* Picometer-Scale Electronic Control of Molecular Dynamics inside a Single Molecule. *Science* **308**, 1000-1003 (2005).

115 Swart, I.; Sonnleitner, T.; Niedenführ, J. & Repp, J. Controlled Lateral Manipulation of Molecules on Insulating Films by Stm. *Nano Lett.* **12**, 1070-1074 (2012).

116 Custance, O.; Perez, R. & Morita, S. Atomic Force Microscopy as a Tool for Atom Manipulation. *Nat. Nanotechnol.* **4**, 803-810 (2009).

117 Repp, J.; Meyer, G.; Paavilainen, S.; Olsson, F. E. & Persson, M. Imaging Bond Formation between a Gold Atom and Pentacene on an Insulating Surface. *Science* **312**, 1196-1199 (2006).

118 Moresco, F. Manipulation of Large Molecules by Low-Temperature Stm: Model Systems for Molecular Electronics. *Phys. Rep.* **399**, 175-225 (2004).

119 Lorente, N.; Rurali, R. & Tang, H. Single-Molecule Manipulation and Chemistry with the Stm. *J. Phys.: Condens. Matter.* **17**, S1049-S1074 (2005).

120 Otero, R.; Rosei, F. & Besenbacher, F. Scanning Tunneling Microscopy Manipulation of Complex Organic Molecules on Solid Surfaces. *Annu. Rev. Phys. Chem.* **57**, 497-525 (2006).

121 Moresco, F. *et al.* Conformational Changes of Single Molecules Induced by Scanning Tunneling Microscopy Manipulation: A Route to Molecular Switching. *Phys. Rev. Lett.* **86**, 672-675 (2001).

122 Qiu, X. H.; Nazin, G. V. & Ho, W. Mechanisms of Reversible Conformational Transitions in a Single Molecule. *Phys. Rev. Lett.* **93**, 196806 (2004).

123 Alemani, M. *et al.* Electric Field-Induced Isomerization of Azobenzene by Stm. *J. Am. Chem. Soc.* **128**, 14446-14447 (2006).

124 Kudernac, T. *et al.* Electrically Driven Directional Motion of a Four-Wheeled Molecule on a Metal Surface. *Nature* **479**, 208-211 (2011).

125 Liljeroth, P.; Repp, J. & Meyer, G. Current-Induced Hydrogen Tautomerization and Conductance Switching of Naphthalocyanine Molecules. *Science* **317**, 1203-1206 (2007).

126 Pan, S. *et al.* Design and Control of Electron Transport Properties of Single Molecules. *Proc. Nat. Acad. Sci.* **106**, 15259-15263 (2009).

127 Bischoff, F. *et al.* How Surface Bonding and Repulsive Interactions Cause Phase Transformations: Ordering of a Prototype Macrocyclic Compound on Ag(111). *ACS Nano* **7**, 3139-3149 (2013).

128 Pivetta, M.; Ternes, M.; Patthey, F. & Schneider, W.-D. Diatomic Molecular Switches to Enable the Observation of Very-Low-Energy Vibrations. *Phys. Rev. Lett.* **99**, 126104 (2007).

129 Mohn, F. *et al.* Reversible Bond Formation in a Gold-Atom–Organic-Molecule Complex as a Molecular Switch. *Phys. Rev. Lett.* **105**, 266102 (2010).

130 Dujardin, G.; Walkup, R. E. & Avouris, P. H. Dissociation of Individual Molecules with Electrons from the Tip of a Scanning Tunneling Microscope. *Science* **255**, 1232-1235 (1992).

131 Martel, R.; Avouris, P. & Lyo, I. W. Molecularly Adsorbed Oxygen Species on Si(111)-(7×7): Stm-Induced Dissociative Attachment Studies. *Science* **272**, 385-388 (1996).

132 Stipe, B. C. *et al.* Single-Molecule Dissociation by Tunneling Electrons. *Phys. Rev. Lett.* **78**, 4410-4413 (1997).

133 Lee, H. J. & Ho, W. Single-Bond Formation and Characterization with a Scanning Tunneling Microscope. *Science* **286**, 1719-1722 (1999).

134 Liljeroth, P.; Swart, I.; Paavilainen, S.; Repp, J. & Meyer, G. Single-Molecule Synthesis and Characterization of Metal–Ligand Complexes by Low-Temperature Stm. *Nano Lett.* **10**, 2475-2479 (2010).

135 Auwärter, W. *et al.* A Surface-Anchored Molecular Four-Level Conductance Switch Based on Single Proton Transfer. *Nat. Nanotechnol.* **7**, 41-46 (2012).

136 Sloan, P. A.; Sakulsermsuk, S. & Palmer, R. E. Nonlocal Desorption of Chlorobenzene Molecules from the Si(111)-(7×7) Surface by Charge Injection from the Tip of a Scanning Tunneling Microscope: Remote Control of Atomic Manipulation. *Phys. Rev. Lett.* **105**, 048301 (2010).

137 http://researcher.watson.ibm.com/researcher/view_group.php?id=4245.

138 Batten, S. R.; Neville, S. M. & Turner, D. R. *Coordination Polymers. Design, Analysis and Application*. (The Royal Society of Chemistry, 2009).

139 Shechtman, D.; Blech, I.; Gratias, D. & Cahn, J. W. Metallic Phase with Long-Range Orientational Order and No Translational Symmetry. *Phys. Rev. Lett.* **53**, 1951-1953 (1984).

140 Steurer, W. Twenty Years of Structure Research on Quasicrystals. *Z. Kristallogr.* **219**, 391-446 (2004).

141 Steurer, W. Fascinating Quasicrystals. *Chem. Soc. Rev.* **41**, 6717-6718 (2012).

142 Steurer, W. Why Are Quasicrystals Quasiperiodic? *Chem. Soc. Rev.* **41**, 6719-6729 (2012).

143 Ishimasa, T.; Nissen, H. U. & Fukano, Y. New Ordered State between Crystalline and Amorphous in Ni-Cr Particles. *Phys. Rev. Lett.* **55**, 511-513 (1985).

144 Poon, S. J. Electronic Properties of Quasicrystals an Experimental Review. *Adv. Phys.* **41**, 303-363 (1992).

145 Dubois, J.-M. Properties and Applications of Quasicrystals and Complex Metallic Alloys. *Chem. Soc. Rev.* **41**, 6760-6777 (2012).

146 Vardeny, Z. V.; Nahata, A. & Agrawal, A. Optics of Photonic Quasicrystals. *Nature Photon.* **7**, 177-187 (2013).

147 Zeng, X. *et al.* Supramolecular Dendritic Liquid Quasicrystals. *Nature* **428**, 157-160 (2004).

148 Hayashida, K.; Dotera, T.; Takano, A. & Matsushita, Y. Polymeric Quasicrystal: Mesoscopic Quasicrystalline Tiling in Abc Star Polymers. *Phys. Rev. Lett.* **98**, 195502 (2007).

149 Xiao, C.; Fujita, N.; Miyasaka, K.; Sakamoto, Y. & Terasaki, O. Dodecagonal Tiling in Mesoporous Silica. *Nature* **487**, 349-353 (2012).

150 Bindi, L.; Steinhardt, P. J.; Yao, N. & Lu, P. J. Natural Quasicrystals. *Science* **324**, 1306-1309 (2009).

151 Bindi, L. *et al.* Evidence for the Extraterrestrial Origin of a Natural Quasicrystal. *Proc. Natl. Acad. Sci. USA.* **109**, 1396-1401 (2012).

152 Bindi, L. *et al.* Natural Quasicrystal with Decagonal Symmetry. *Sci. Rep.* **5**, 9111 (2015).

153 Talapin, D. V. *et al.* Quasicrystalline Order in Self-Assembled Binary Nanoparticle Superlattices. *Nature* **461**, 964-967 (2009).

154 Wasio, N. A. *et al.* Self-Assembly of Hydrogen-Bonded Two-Dimensional Quasicrystals. *Nature* **507**, 86-89 (2014).

155 Fischer, S. *et al.* Colloidal Quasicrystals with 12-Fold and 18-Fold Diffraction Symmetry. *Proc. Natl. Acad. Sci. USA.* **108**, 1810-1814 (2011).

156 Forster, S.; Meinel, K.; Hammer, R.; Trautmann, M. & Widdra, W. Quasicrystalline Structure Formation in a Classical Crystalline Thin-Film System. *Nature* **502**, 215-+ (2013).

157 Chen, H.; Li, D. X. & Kuo, K. H. New Type of Two-Dimensional Quasicrystal with Twelvefold Rotational Symmetry. *Phys. Rev. Lett.* **60**, 1645-1648 (1988).

158 Ishimasa, T. *Dodecagonal Quasicrystals* (2011).

159 Conrad, M.; Krumeich, F. & Harbrecht, B. A Dodecagonal Quasicrystalline Chalcogenide. *Angew. Chem. Int. Ed.* **37**, 1383-1386 (1998).

160 Lifshitz, R. & Diamant, H. Soft Quasicrystals–Why Are They Stable? *Philos. Mag.* **87**, 3021-3030 (2007).

161 Dotera, T. Toward the Discovery of New Soft Quasicrystals: From a Numerical Study Viewpoint. *J. Polym. Sci., Part B: Polym. Phys.* **50**, 155-167 (2012).

162 Yang, Z.; Wei, J.; Bonville, P. & Pileni, M.-P. Beyond Entropy: Magnetic Forces Induce Formation of Quasicrystalline Structure in Binary Nanocrystal Superlattices. *J. Am. Chem. Soc.* **137**, 4487-4493 (2015).

163 Keys, A. S. & Glotzer, S. C. How Do Quasicrystals Grow? *Phys. Rev. Lett.* **99**, 235503 (2007).

164 Iacovella, C. R.; Keys, A. S. & Glotzer, S. C. Self-Assembly of Soft-Matter Quasicrystals and Their Approximants. *Proc. Natl. Acad. Sci. USA.* **108**, 20935-20940 (2011).

165 Ungar, G. & Zeng, X. Frank–Kasper, Quasicrystalline and Related Phases in Liquid Crystals. *Soft Matter* **1**, 95-106 (2005).

166 Lee, S.; Bluemle, M. J. & Bates, F. S. Discovery of a Frank-Kasper Σ Phase in Sphere-Forming Block Copolymer Melts. *Science* **330**, 349-353 (2010).

167 Goldman, A. & Kelton, R. Quasicrystals and Crystalline Approximants. *Rev. Mod. Phys.* **65**, 213 (1993).

168 Gähler, F. *Quasicrystal Structures from the Crystallographic Viewpoint*. PhD thesis, Swiss Federal Institute Of Technology (ETH), (1988).

169 Janssen, T.; Chapuis, G. & Boissieu, M. d. *Aperiodic Crystals. From Modulated Phases to Quasicrystals*. (Oxford University Press, 2007).

170 Steurer, W. & Deloudi, S. *Crystallography of Quasicrystals*. (Springer, 2009).

171 Baake, M. & Grimm, U. *Encyclopedia of Mathematics and Its Mpplications: Aperiodic Order*. (Cambridge University Press, 2013).

172 Gähler, F.; Janot, C. & Dubois, J. in *Proceeding of the ILL/CODEST Workshop.* 272-284 (World Scientific, Singapore).

173 Stämpfli, P. A Dodecagonal Quasi-Periodic Lattice in Two Dimensions. *Helv. Phys. Acta* **59**, 1260-1263 (1986).

174 Niizeki, N. & Mitani, H. Two-Dimensional Dodecagonal Quasilattices. *J. Phys. A: Math. Gen.* **20**, L405-L410 (1987).

175 Baake, M.; Klitzing, R. & Schlottmann, M. Fractally Shaped Acceptance Domains of Quasiperiodic Square-Triangle Tilings with Dedecagonal Symmetry. *Phys. A.* **191**, 554-558 (1992).

176 Kawamura, H. Statistics of Two-Dimensional Amorphous Lattice. *Progr. Theor. Exp. Phys.* **70**, 352-365 (1983).

177 Leung, P. W.; Henley, C. L. & Chester, G. V. Dodecagonal Order in a Two-Dimensional Lennard-Jones System. *Phys. Rev. B* **39**, 446-458 (1989).

178 Oxborrow, M. & Henley, C. L. Random Square-Triangle Tilings. *Phys. Rev. B* **48**, 6996-6998 (1993).

179 Widom, M. Bethe Ansatz Solution of the Square-Triangle Random-tiling Model. *Phys. Rev. Lett.* **70**, 2094-2097 (1993).

180 Grimm, U. & Joseph, D. 199-218 (Springer, 2002).

181 Dzugutov, M. Formation of a Dodecagonal Quasicrystalline Phase in a Simple Monatomic Liquid. *Phys. Rev. Lett.* **70**, 2924 (1993).

182 Barkan, K.; Diamant, H. & Lifshitz, R. Stability of Quasicrystals Composed of Soft Isotropic Particles. *Phys. Rev. B* **83**, 172201 (2011).

183 Barkan, K.; Engel, M. & Lifshitz, R. Controlled Self-Assembly of Periodic and Aperiodic Cluster Crystals. *Phys. Rev. Lett.* **113** (2014).

184 Dotera, T.; Oshiro, T. & Ziherl, P. Mosaic Two-Lengthscale Quasicrystals. *Nature* **506**, 208-211 (2014).

185 Glotzer, S. C. Assembly Engineering: Materials Design for the 21st Century (2013 Pv Danckwerts Lecture). *Chem. Eng. Sci.* **121**, 3-9 (2015).

186 Garcia, J. & Allen, M. J. Developments in the Coordination Chemistry of Europium(II). *Eur. J. Inorg. Chem.* **2012**, 4550-4563 (2012).

187 Palma, C.-A. *et al.* Topological Dynamics in Supramolecular Rotors. *Nano Lett.* **14**, 4461-4468 (2014).

188 Lensen, D. & Elemans, J. A. Artificial Molecular Rotors and Motors on Surfaces: Stm Reveals and Triggers. *Soft Matter* **8**, 9053-9063 (2012).

189 Haji-Akbari, A. *et al.* Disordered, Quasicrystalline and Crystalline Phases of Densely Packed Tetrahedra. *Nature* **462**, 773-777 (2009).

190 Joseph, D. & Elser, V. A Model of Quasicrystal Growth. *Phys. Rev. Lett.* **79**, 1066-1069 (1997).

191 Müllegger, S.; Hänel, K.; Strunskus, T.; Wöll, C. & Winkler, A. Organic Molecular Beam Deposition of Oligophenyls on Au (111): A Study by X-Ray Absorption Spectroscopy. *ChemPhysChem* **7**, 2552-2558 (2006).

192 Marschall, M. *et al.* Supramolecular Organization and Chiral Resolution of P-Terphenyl-M-Dicarbonitrile on the Ag (111) Surface. *ChemPhysChem* **11**, 1446-1451 (2010).

193 Henze, S.; Bauer, O.; Lee, T.-L.; Sokolowski, M. & Tautz, F. Vertical Bonding Distances of Ptcda on Au (111) and Ag (111): Relation to the Bonding Type. *Surf. Sci.* **601**, 1566-1573 (2007).

194 Küster, W. Beiträge Zur Kenntnis Des Bilirubins Und Kamins. *Hoppe-Seyler´s Z. Physiol. Chem.* **82**, 463 (1912).

195 Arnold, J. *The Porphyrin Handbook*. Vol. 7 (1999).

196 Burrell, A. K.; Officer, D. L.; Plieger, P. G. & Reid, D. C. Synthetic Routes to Multiporphyrin Arrays. *Chem. Rev.* **101**, 2751-2796 (2001).

197 Anderson, H. L. Building Molecular Wires from the Colours of Life: Conjugated Porphyrin Oligomers. *Chem. Commun.*, 2323-2330 (1999).

198 Li, Y. *et al.* Coordination and Metalation Bifunctionality of Cu with 5,10,15,20-Tetra(4-Pyridyl)Porphyrin: Toward a Mixed-Valence Two-Dimensional Coordination Network. *J. Am. Chem. Soc.* **134**, 6401-6408 (2012).

199 Mohnani, S. & Bonifazi, D. Supramolecular Architectures of Porphyrins on Surfaces: The Structural Evolution from 1D to 2D to 3D to Devices. *Coord. Chem. Rev.* **254**, 2342-2362 (2010).

200 Hieringer, W. *et al.* The Surface Trans Effect: Influence of Axial Ligands on the Surface Chemical Bonds of Adsorbed Metalloporphyrins. *J. Am. Chem. Soc.* **133**, 6206-6222 (2011).

201 Seufert, K.; Auwärter, W. & Barth, J. V. Discriminative Response of Surface-Confined Metalloporphyrin Molecules to Carbon and Nitrogen Monoxide. *J. Am. Chem. Soc.* **132**, 18141-18146 (2010).

202 Wäckerlin, C. *et al.* Ammonia Coordination Introducing a Magnetic Moment in an on-Surface Low-Spin Porphyrin. *Angew. Chem. Int. Ed.* **52**, 4568-4571 (2013).

203 Hulsken, B. *et al.* Real-Time Single-Molecule Imaging of Oxidation Catalysis at a Liquid–Solid Interface. *Nature nanotechnology* **2**, 285-289 (2007).

204 Sedona, F. *et al.* Tuning the Catalytic Activity of Ag(110)-Supported Fe Phthalocyanine in the Oxygen Reduction Reaction. *Nat. Mater.* **11**, 970-977 (2012).

205 Yilmaz, M. D. & Huskens, J. Orthogonal Supramolecular Interaction Motifs for Functional Monolayer Architectures. *Soft Matter* **8**, 11768-11780 (2012).

206 Plečnik, C. E.; Liu, S. & Shore, S. G. Lanthanide−Transition-Metal Complexes: From Ion Pairs to Extended Arrays. *Acc. Chem. Res.* **36**, 499-508 (2003).

207 Chen, F.; Chen, Z.; Bian, Z. & Huang, C. Sensitized Luminescence from Lanthanides in D–F Bimetallic Complexes. *Coord. Chem. Rev.* **254**, 991-1010 (2010).

208 Huang, Y.; Jiang, F. & Hong, M. Magnetic Lanthanide–Transition-Metal Organic–Inorganic Hybrid Materials: From Discrete Clusters to Extended Frameworks. *Coord. Chem. Rev.* **253**, 2814-2834 (2009).

209 Sanders, J. K. M. *et al. The Porphyrin Handbook*. Vol. 7 (1999).

210 Auwärter, W. *et al.* Controlled Metalation of Self-Assembled Porphyrin Nanoarrays in Two Dimensions. *ChemPhysChem* **8**, 250-254 (2007).

211 Gottfried, J. M.; Flechtner, K.; Kretschmann, A.; Lukasczyk, T. & Steinrück, H.-P. Direct Synthesis of a Metalloporphyrin Complex on a Surface. *J. Am. Chem. Soc.* **128**, 5644-5645 (2006).

212 Wong, C.-H. & Zimmerman, S. C. Orthogonality in Organic, Polymer, and Supramolecular Chemistry: From Merrifield to Click Chemistry. *Chem. Commun.* **49**, 1679-1695 (2013).

213 Shi, J. *et al.* Polynitrile-Bridged Two-Dimensional Crystal: Eu(Iii) Complex with Strong Fluorescence Emission and Nlo Property. *Chem. Commun.*, 756-757 (2002).

214 Shubina, T. E. *et al.* Principle and Mechanism of Direct Porphyrin Metalation: A Joint Experimental and Theoretical Investigation. *J. Am. Chem. Soc.* **129**, 9476-9483 (2007).

215 Auwärter, W. *et al.* Site-Specific Electronic and Geometric Interface Structure of Co-Tetraphenyl-Porphyrin Layers on Ag(111). *Phys. Rev. B* **81**, 245403 (2010).

216 Kühne, D. *et al.* High-Quality 2d Metal−Organic Coordination Network Providing Giant Cavities within Mesoscale Domains. *J. Am. Chem. Soc.* **131**, 3881-3883 (2009).

217 Reichert, J. *et al.* Competing Interactions in Surface Reticulation with a Prochiral Dicarbonitrile Linker. *J. Phys. Chem. C* **117**, 12858-12863 (2013).

218 Nozaki, C.; Lugmair, C. G.; Bell, A. T. & Tilley, T. D. Synthesis, Characterization, and Catalytic Performance of Single-Site Iron (Iii) Centers on the Surface of Sba-15 Silica. *J. Am. Chem. Soc.* **124**, 13194-13203 (2002).

219 Copéret, C.; Chabanas, M.; Petroff Saint-Arroman, R. & Basset, J. M. Homogeneous and Heterogeneous Catalysis: Bridging the Gap through Surface Organometallic Chemistry. *Angew. Chem. Int. Ed.* **42**, 156-181 (2003).

220 Faul, C. F. & Antonietti, M. Ionic Self-Assembly: Facile Synthesis of Supramolecular Materials. *Adv. Mater.* **15**, 673-683 (2003).

221 Zhang, T.; Spitz, C.; Antonietti, M. & Faul, C. F. Highly Photoluminescent Polyoxometaloeuropate-Surfactant Complexes by Ionic Self-Assembly. *Chemistry-A European Journal* **11**, 1001-1009 (2005).

222 Zakrevskyy, Y.; Smarsly, B.; Stumpe, J. & Faul, C. Highly Ordered Monodomain Ionic Self-Assembled Liquid-Crystalline Materials. *Phys. Rev. E* **71**, 021701 (2005).

223 Wang, Z.; Medforth, C. J. & Shelnutt, J. A. Porphyrin Nanotubes by Ionic Self-Assembly. *J. Am. Chem. Soc.* **126**, 15954-15955 (2004).

224 Bünzli, J.-C. G. Review: Lanthanide Coordination Chemistry: From Old Concepts to Coordination Polymers. *J. Coord. Chem.* **67**, 3706-3733 (2014).

225 Reineke, T. M.; Eddaoudi, M.; Fehr, M.; Kelley, D. & Yaghi, O. M. From Condensed Lanthanide Coordination Solids to Microporous Frameworks Having Accessible Metal Sites. *J. Am. Chem. Soc.* **121**, 1651-1657 (1999).

226 Pan, L. *et al.* Porous Lanthanide-Organic Frameworks: Synthesis, Characterization, and Unprecedented Gas Adsorption Properties. *J. Am. Chem. Soc.* **125**, 3062-3067 (2003).

227 Qin, C.; Wang, X.-L.; Wang, E.-B. & Su, Z.-M. A Series of Three-Dimensional Lanthanide Coordination Polymers with Rutile and Unprecedented Rutile-Related Topologies. *Inorg. Chem.* **44**, 7122-7129 (2005).

228 Long, D.-L.; Blake, A. J.; Champness, N. R.; Wilson, C. & Schröder, M. Lanthanum Coordination Networks Based on Unusual Five-Connected Topologies. *J. Am. Chem. Soc.* **123**, 3401-3402 (2001).

229 Long, D.-L. *et al.* Non-Natural Eight-Connected Solid-State Materials: A New Coordination Chemistry. *Angew. Chem. Int. Ed.* **43**, 1851-1854 (2004).

230 Wong, K. L.; Law, G. L.; Yang, Y. Y. & Wong, W. T. A Highly Porous Luminescent Terbium–Organic Framework for Reversible Anion Sensing. *Adv. Mater.* **18**, 1051-1054 (2006).

231 Long, D.-L.; Blake, A. J.; Champness, N. R.; Wilson, C. & Schröder, M. Unprecedented Seven- and Eight-Connected Lanthanide Coordination Networks. *Angew. Chem. Int. Ed.* **40**, 2443-2447 (2001).

232 Chaumeil, H.; Le Drian, C. & Defoin, A. Efficient Synthesis of Substituted Terphenyls by Suzuki Coupling Reaction. *Synthesis*, 757-760 (2002).

233 Barth, J. V.; Weckesser, J.; Lin, N.; Dmitriev, A. & Kern, K. Supramolecular Architectures and Nanostructures at Metal Surfaces. *Appl. Phys. A* **76**, 645-652 (2003).

234 Stepanow, S.; Lin, N.; Barth, J. V. & Kern, K. Surface-Template Assembly of Two-Dimensional Metal−Organic Coordination Networks. *J. Phys. Chem. B* **110**, 23472-23477 (2006).

235 Vitali, L. *et al.* Portrait of the Potential Barrier at Metal-Organic Nanocontacts. *Nat. Mater.* **9**, 320-323 (2010).

236 Messina, P. *et al.* Direct Observation of Chiral Metal-Organic Complexes Assembled on a Cu(100) Surface. *J. Am. Chem. Soc.* **124**, 14000-14001 (2002).

237 Stepanow, S. *et al.* Programming Supramolecular Assembly and Chirality in Two-Dimensional Dicarboxylate Networks on a Cu(100) Surface. *Nano Lett.* **5**, 901-904 (2005).

238 Tait, S. L. *et al.* Metal−Organic Coordination Interactions in Fe−Terephthalic Acid Networks on Cu(100). *J. Am. Chem. Soc.* **130**, 2108-2113 (2008).

239 Stepanow, S. *et al.* Rational Design of Two-Dimensional Nanoscale Networks by Electrostatic Interactions at Surfaces. *ACS Nano* **4**, 1813-1820 (2010).

240 Kley, C. S. *et al.* Highly Adaptable Two-Dimensional Metal–Organic Coordination Networks on Metal Surfaces. *J. Am. Chem. Soc.* **134**, 6072-6075 (2012).

241 Grumelli, D.; Wurster, B.; Stepanow, S. & Kern, K. Bio-Inspired Nanocatalysts for the Oxygen Reduction Reaction. *Nat. Commun.* **4** (2013).

242 Cotton, S. *Lanthanide and Actinide Chemistry*. (John Wiley & Sons, 2006).

243 Han, Y. *et al.* Structures and Properties of Porous Coordination Polymers Based on Lanthanide Carboxylate Building Units. *Inorg. Chem.* **49**, 10781-10787 (2010).

244 Seitsonen, A. P. *et al.* Density Functional Theory Analysis of Carboxylate-Bridged Diiron Units in Two-Dimensional Metal-Organic Grids. *J. Am. Chem. Soc.* **126**, 5634-5635 (2006).

245 Clair, S. *et al.* Monitoring Two-Dimensional Coordination Reactions: Directed Assembly of Co-Terephthalate Nanosystems on Au (111). *J. Phys. Chem. B* **110**, 5627-5632 (2006).

246 Abdurakhmanova, N. *et al.* Stereoselectivity and Electrostatics in Charge-Transfer Mn- and Cs-Tcnq4 Networks on Ag(100). *Nat. Commun.* **3**, 940 (2012).

247 Spillmann, H. *et al.* Hierarchical Assembly of Two-Dimensional Homochiral Nanocavity Arrays. *J. Am. Chem. Soc.* **125**, 10725-10728 (2003).

248 Skomski, D.; Abb, S. & Tait, S. L. Robust Surface Nano-Architecture by Alkali–Carboxylate Ionic Bonding. *J. Am. Chem. Soc.* **134**, 14165-14171 (2012).

249 Skomski, D.; Tempas, C. D.; Smith, K. A. & Tait, S. L. Redox-Active on-Surface Assembly of Metal–Organic Chains with Single-Site Pt(II). *J. Am. Chem. Soc.* **136**, 9862-9865 (2014).

250 Nazin, G.; Qiu, X. & Ho, W. Visualization and Spectroscopy of a Metal-Molecule-Metal Bridge. *Science* **302**, 77-81 (2003).

251 Blom, P. W.; Mihailetchi, V. D.; Koster, L. J. A. & Markov, D. E. Device Physics of Polymer: Fullerene Bulk Heterojunction Solar Cells. *Adv. Mater.* **19**, 1551-1566 (2007).

252 Günes, S.; Neugebauer, H. & Sariciftci, N. S. Conjugated Polymer-Based Organic Solar Cells. *Chem. Rev.* **107**, 1324-1338 (2007).

253 Moons, E. Conjugated Polymer Blends: Linking Film Morphology to Performance of Light Emitting Diodes and Photodiodes. *J. Phys.: Condens. Matter* **14**, 12235 (2002).

254 Cicoira, F. & Santato, C. Organic Light Emitting Field Effect Transistors: Advances and Perspectives. *Adv. Funct. Mater.* **17**, 3421-3434 (2007).

255 Yamachika, R.; Grobis, M.; Wachowiak, A. & Crommie, M. Controlled Atomic Doping of a Single C60 Molecule. *Science* **304**, 281-284 (2004).

256 Wegner, D. *et al.* Tuning Molecule-Mediated Spin Coupling in Bottom-up-Fabricated Vanadium-Tetracyanoethylene Nanostructures. *Phys. Rev. Lett.* **103**, 087205 (2009).

257 Wang, W. *et al.* Manipulating Localized Molecular Orbitals by Single-Atom Contacts. *Phys. Rev. Lett.* **105**, 126801 (2010).

258 Yang, H.-H. *et al.* Digitized Charge Transfer Magnitude Determined by Metal–Organic Coordination Number. *ACS Nano* **7**, 2814-2819 (2013).

259 Yang, Z. *et al.* Orbital Redistribution in Molecular Nanostructures Mediated by Metal–Organic Bonds. *ACS Nano* **8**, 10715-10722 (2014).

260 Liljeroth, P.; Swart, I.; Paavilainen, S.; Repp, J. & Meyer, G. Single-Molecule Synthesis and Characterization of Metal− Ligand Complexes by Low-Temperature Stm. *Nano Lett.* **10**, 2475-2479 (2010).

261 VandeVondele, J. *et al.* Fast and Accurate Density Functional Calculations Using a Mixed Gaussian and Plane Waves Approach. *Comput. Phys. Commun.* **167**, 103-128 (2005).

262 Zhang, Y. & Yang, W. Comment on "Generalized Gradient Approximation Made Simple". *Phys. Rev. Lett.* **80**, 890-891 (1998).

263 Grimme, S. & Antony, J. A Consistent and Accurate *Ab Initio* Parametrisation of Density Functional Dispersion Correction (DFT-D) for the 94 Elements H-Pu. *J. Chem. Phys.* **132**, 154104 (2010).

264 Lippert, G.; Hutter, J. & Parrinello, M. A Hybrid Gaussian and Plane Wave Density Functional Scheme. *Mol. Phys.* **92**, 477-487 (1997).

265 Gómez-Díaz, J. *et al.* Hexagonal Boron Nitride on Transition Metal Surfaces. *Theor. Chem. Acc.* **132**, 1350 (2013).

266 Goedecker, S.; Teter, M. & Hutter, J. Separable Dual-Space Gaussian Pseudopotentials. *Phys. Rev. B* **54**, 1703-1710 (1996).

267 VandeVondele, J. & Hutter, J. Gaussian Basis Sets for Accurate Calculations on Molecular Systems in Gas and Condensed Phases. *J. Chem. Phys.* **127**, 114105 (2007).

268 Kresse, G. & Hafner, J. *Phys. Rev. B* **49**, 14251 (1994).

269 Kresse, G. & Furthmüller, J. *Phys. Rev. B* **54**, 11169 (1996).

270 Kresse, G. & Furthmüller, J. *Comput. Mater. Sci.* **6**, 15 (1996).

271 Perdew, J. P.; Burke, W. & Ernzerhof, M. *Phys. Rev. Lett.* **77**, 3965 (1996).

272 Grimme, S. *J. Comp. Chem.* **27**, 1787 (2006).

273 Blöchl, P. E. Projector Augmented Wave Method. *Phys. Rev. B* **59**, 17953-17979 (1994).

274 Kresse, G. & Joubert, D. *Phys. Rev. B* **59**, 1758 (1999).

275 Methfessel, M. & Paxton, A. *Phys. Rev. B* **40**, 3616 (1989).

276 Monkhorst, H. J. & Pack, J. D. *Phys. Rev. B* **13**, 5188 (1976).

277 Bader, R. F. W. *Atoms in Molecules - a Quantum Theory*. (1990).

278 Arnaldsson, A.; Tang, W. & Henkelman, G. *Bader Analysis Program,* *Http://Theory.Cm.Utexas.Edu/Vtsttools/Bader/*.